NUMERICAL MODELING OF THE EFFECT OF SULFUR POISONING ON THE PERFORMANCE OF THE POROUS ANODE SOLID OXIDE FUEL CELL

by

Negar Manafi Rasi

A thesis submitted to the Department of Chemical Engineering

In conformity with the requirements for

the degree of Master of Applied Science

Queen's University

Kingston, Ontario, Canada

(November 2014)

Abstract

A numerical model to capture the effect of H_2S impurities on the Solid Oxide Fuel Cell (SOFC) performance with Ni-based porous anode is developed. H_2S impurities can adversely affect the fuel cell performance, due to the sulfur poisoning of the Ni catalyst of the SOFC anode. The novelty of this work is the derivation of a Butler-Volmer type kinetic formulation that captures the effect of sulfur poisoning on the H_2 electro-oxidation reaction in the Ni-YSZ anode of SOFC. The novel kinetic model is then incorporated into a 2-dimensional porous anode model with gas-phase species transport, charged species transport and anode electrochemistry. The result is a performance model that can predict the effect of H_2S impurity on the polarization curves of the SOFC by taking into account the transport phenomena in addition to the electrochemistry formulations. Two types of kinetic models named as "coverage dependent kinetic model" and "coverage independent kinetic model", differing in the coverage dependency of energy of H_2 and H_2S adsorption reactions are developed and incorporated in the 2D porous anode model. Loss in performance is predicted by both kinetic models and 2D performance models. Both kinetic models predictions show an increase in the current density loss with an increase in H_2S concentration. 2D performance models predictions with both coverage dependent and coverage independent models show an increasing trend in both the loss in the cell voltage and increase in the cell resistance upon the increase of the inlet H_2S content of the fuel. The 2D performance model with coverage-dependent kinetics predicts lower loss in the cell performance than the 2D performance model with coverage-independent kinetics. By comparing the performance model predictions with the experimental results, similar trends of increase in the sulfur poisoning effect by increase in H_2S content and smaller increase in the relative cell resistance at higher current densities can be recognized in both experimental results and the 2D model predictions. Coverage-dependent 2D performance model predictions are closer to the experimental results than the coverage-independent 2D performance model predictions.

Acknowledgements

I would like to thank Dr. Kunal Karan for his encouragement, guidance and support thorough out this study. I am grateful for his scientific advices, insightful discussions and constructive suggestions, without which this work would have not been accomplished. I would also like to thank Dr. Dayadeep Monder and Eric Hardjo for their valuable technical support. The work reported in this dissertation was supported by funding from the National Science and Engineering Research Council (NSERC) through the Solid Oxide Fuel Cell Canada Strategic Research Network.

I would also like to extend my thanks to my colleagues at the Queen's-RMC Fuel cell Research Centre, Dr. Brant A. Peppley, Ela Halliop, Mayur Mundhwa and Parisa Karimi, who helped me with remotely accessing computers in FCRC to run simulations during my stay in Calgary.

Appreciation is due to Aida Khosravi, Parnian Haghighat, Nikoo Sabzvar, Seyedshahab Esmaeilnejad and Barath Ram Jayasankar, for their friendship and emotional support. Acknowledgements are also due to my teachers who have motivated me with their dedication over the years.

Finally, I would like to express my gratitude and love to my family. I am most thankful to my mother, Haydeh, who kept my hopes alive along this path with her unconditional love and support; my father, Jalil, from whom I received my optimistic perception of life and for his faith on me and my abilities; and my beloved sister, Setareh, who was my inspiration to stay motivated and energetic in pursue of my goals. I would also like to extend my appreciation to my aunt and her beloved family for their love and support as well as my grandparents who have always encouraged me to achieve my dreams.

Table of Contents

List of Figures

List of Tables

Nomenclature

A_{des}	Pre-exponential factor for the hydrogen desorption reaction from Nickel
ASR	Average area specific resistance
D_{ij}	Binary diffusion coefficient
$\widetilde{D}_{ij}$	Multicomponent Fick diffusivity of species i in j
D_{ij}^{eff}	Effective binary diffusion coefficient in a porous medium
d_j	Diffusional driving force
d_p	Mean particle diameter
E_a	Difference between the potential of electronic phase and potential of ionic phase in anode
E_a^{eq}	Equilibrium potential difference between the electronic phase and the ionic phase in anode
E_c	Difference between the potential of electronic phase and potential of ionic phase in anode
$E_c{}^{eq}$	Equilibrium potential difference between the electronic phase and the ionic phase in anode
E_{cell}	Cell voltage
E_{ocv}	Open circuit voltage
$\Delta E_{cell,R}$	Relative loss in the cell voltage at constant current density
$E_{cell\|H2}$	Cell voltage for fuel mixture without H_2S impurities
$E_{cell\|H2S}$	Cell voltage or fuel mixture with H_2S impurities
E_{ion}	Activation energy of O^{2-} conduction
E_{des}	Activation energy for the hydrogen desorption reaction from Nickel
$E_{el,i}$	Electronic energy of species i
$E_{ZPV,i}$	Zero point vibrational energy of species i
$E_{th,i}$	Thermal energy of species i

$E_H(0)$	Hydrogen adsorption energy at zero coverage
$E_S(0)$	Sulfur adsorption energy at zero coverage
F	Faraday's constant (96, 487 C/mol)
G_i^0	Standard state Gibbs free energy of species i
$\Delta G_{H2,ads}^0$	Standard state Gibbs free energy of H_2 adsorption reaction
$\Delta G_{H_2S,ads}^0$	Standard state Gibbs free energy of H_2S adsorption reaction
H_i^0	Standard state Molar enthalpy of species i
h	Planck constant
H_{ed}	Height of the electrode
H_{ch}	Height of the fuel channel
i_0	Exchange current density for hydrogen oxidation reaction
i_{H2}^*	Exchange current density factor for hydrogen oxidation reaction
$i_{ref\_H2}^*$	Exchange current density factor for hydrogen oxidation reaction at reference temperature
i_V	Volumetric current density
i_{tar}	Target current density
$\mathbf{i_i}$	Ionic flux vector
$\mathbf{i_e}$	Electronic flux vector
I	Identity Matrix
$\mathbf{j_i}$	Diffusive flux of species i
$\mathbf{J_i}$	Total flux of species i
K_i	Equilibrium constants of reaction i
K_{H2}	Equilibrium constant of H_2 adsorption
K_{H2S}	Equilibrium constant of H_2S adsorption
k_B	Boltzmann constant

l_{TPB}	TPB length per unit volume
l_{ed_el}	TPB length per contact between electrode and electrolyte
M_i	Molar weights of species i
$\dot{n}_{Fuel}$	Molar flow rate of the inlet fuel
n_{tot}	Number of the particles of the composite anode per unit volume
P_i	Partial pressure of the gas species i
P	Pressure of the gas mixture
P_{ed}	Probability of the electronic phase particle being present into a percolated cluster of its own phase
P_{el}	Probability of the ionic phase particle fall into a percolated cluster of its own phase
R_a	Rate of mass production in anode
r_i	Rate of production of species i
R	Ideal gas constant
R_{Ni}	Radius of the Ni particles
R_{YSZ}	Radius of the YSZ particles
r_{ed}	Radius of the electronic phase particle
r_{el}	Radius of the ionic phase particle
S_i^0	Molar entropy of species i
T	Operating temperature
T_{ref}	Reference temperature
U_f	Fuel utilization factor
v_i	Molar diffusion volumes of species i
$V_{fuel,inlet}$	Mean inlet fuel velocity
v	Velocity vector

w_i	Mass fraction of species i
w_{ed}	Width of the electrode
$x_{H2,in}$	Inlet H_2 molar fraction
$x_{H2O,in}$	Inlet H_2O molar fraction
$x_{H2S,in}$	Inlet H_2S molar fraction
x_j	Mole fraction of species j
Z_{ed}	Coordination number of the electronic phase composite electrode
Z_{el}	Coordination number of the ionic conducting phase composite electrode
Z_{tot}	Overall average coordination number
$Z_{\alpha\beta}$	Average number of the β particles in contact with the α particles

Greek letters

α_a	Anodic charge transfer coefficients
α_c	Cathodic charge transfer coefficients
α_H	Self-interaction parameters for hydrogen
α_S	Self-interaction parameters for sulfur
β_a	Anodic symmetric factors
β_c	Cathodic symmetric factors
β_{HS}	Binary interaction parameter between sulfur and hydrogen
γ_0	Sticking coefficient
Γ	Surface site density
ϵ	Porosity
ζ_{ed}	Number fractions of electrode
ζ_{el}	Number fractions of electrolyte particles
η_a	Local activation overpotental

$\eta_{a\|H2S}$	Effective anode overpotential for fuel mixture with H_2S impurities
$\eta_{a\|H2}$	Effective anode overpotential for fuel mixture without H_2S impurities
$\Delta\eta_{a,R}$	The relative increase in the effective anode overpotential
θ_H	Hydrogen coverage
θ_S	Sulfur coverage
$\theta_H(0)$	Hydrogen threshold coverage
$\theta_S(0)$	Sulfur threshold coverage
θ_H^*	Effective coverage of hydrogen
θ_S^*	Effective coverage of sulfur
κ	Permeability of the gas
μ_{mix}	Average viscosity for the mixture
μ	Viscosity of the gas mixture
μ_j	Chemical potential of species j
μ_j^0	Standard state chemical potential of species j
$\nu_{i,k}$	k^{th} vibrational frequency for species i
ρ_i	Density of species i
ρ	Density of gas mixture
σ_{el}^0	Conductivity of pure electronic conducting phase
σ_{ion}	Ionic conductivity of electrolyte
σ_{el}^{eff}	Effective electronic conductivity of anode
$\sigma_{ion\_an}^{eff}$	Effective ionic conductivity of anode
σ_{ion}^0	Conductivity of pure ionic conducting phase
σ_{0_ion}	Pre factor of O^{2-} conduction
σ_i	Collision diameter (in nm)

τ	Tortuosity
$\emptyset_{\mathrm{el}}$	Electronic phase potential in anode
$\emptyset_{\mathrm{ion}}$	Ionic phase potentials
$\emptyset_{ion(c)}$	Ionic phase potential in cathode
$\emptyset_{\mathrm{el(c)}}$	Electronic phase potential in cathode
ψ_{YSZ}	YSZ volume fraction
ψ_{Ni}	Ni volume fraction
$\Omega_i^{2,2}$	Collision integral

Chapter 1

Introduction

Energy is the key driver for the industrial development of nations. Energy had always been provided from the natural resources, mainly the fossil fuels (Landes 2003). Increase in global energy consumption driven by increasing world population and improving standard of living, limited reserves of fossil fuels, and environmental considerations are the key drivers for a change in the existing pattern of global energy consumption (Fedrigo and Hontelez, 2009). Both the efficient use of energy and the transition to renewable sources of energy are required to achieve this goal. Improving the energy efficiency both at the source and end-user level would help. Since higher efficiency for conversion results in lesser amount of fuel utilized for the same amount of useful work done, Solid Oxide Fuel Cell (SOFC) with high efficiency of energy conversion is considered as one of the sustainable energy technology systems.

1.1 Fuel Cells

Fuel cells are devices that convert the chemical energy of a fuel directly to electricity with heat as a biproduct. Fuel cells have higher efficiencies than the conventional combustion-based energy conversion systems. In addition to their higher efficiencies, they have the advantages of lower emission levels, modularity, reliability and zero noise pollution. The primary components of a fuel cell are an electrolyte for ion conduction, an anode where the oxidation reaction occurs and a cathode where the reduction reaction takes place (Haile, 2003). Fuel cells are generally categorized based on the type of the electrolyte used. Solid oxide Fuel Cell (SOFC) is a type of fuel cell with a solid-oxide (ceramic) electrolyte (S. C. Singhal and Kendall 2003).

1.1.1 Solid oxide fuel cell

Solid Oxide fuel cells work at high temperatures ranging 500ºC - 800ºC. Due to their high operating temperatures, they can be thermally integrated into gas turbines to cogenerate heat and power at combined efficiencies of around 85 % (S. C. Singhal and Kendall 2003). Figure 1-1 shows a schematic diagram of an SOFC. It is composed of cathode, electrolyte and anode. Air is supplied to the cathode while the fuel to the anode. The fuel for SOFCs can be hydrogen or hydrogen-rich reformate, a mixture of CO, CO_2, H_2, and H_2O. The oxygen in the air is reduced to oxygen ions that are conducted through the solid electrolyte towards the anode. Hydrogen electro-oxidation reaction with oxygen ions produces water, electrons and heat.

At the cathode, the overall oxygen reduction reaction can be written as follows:

$$\frac{1}{2}\,\boldsymbol{O_2(g) + 2e^- \Leftrightarrow O^{2-}} \tag{1.1}$$

For hydrogen-fuelled anode, oxidation reaction at the anode can be written as follows:

$$H_2(g) + O^{2-} \Leftrightarrow H_2O(g) + 2e^- \tag{1.2}$$

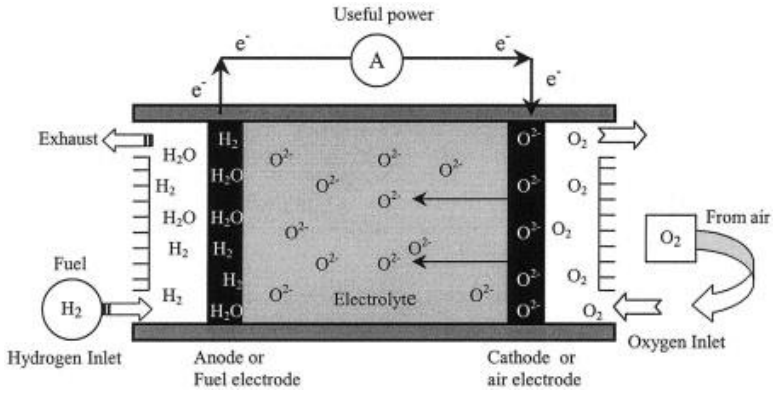

Figure 1-1: Schematic diagram of SOFC (Stambouli and Traversa, 2002)

Thus, if the fuel is pure hydrogen, water is the only chemical product of the anode reaction.

Each of the components of a fuel cell must meet certain functional requirements. Electrolyte of

the solid oxide fuel cells (SOFCs) must have high ionic conductivity and low electronic conductivity at the cell operating temperatures as well as must be dense to separate the fuel and oxidant streams from each other. To date, the most common electrolyte has been the Yittria-stabilized zirconia or YSZ. Cathode of SOFCs must have high electrical conductivity and good catalytic performance for oxygen reduction reaction. Composite of strontium-doped lanthanum manganite (LSM) and YSZ has been widely used as cathode for SOFCs. Anode of SOFCs should have high electronic conductivity and high catalytic activity for hydrogen oxidation reaction. Composites of Ni and YSZ are the most commonly used anodes in SOFCs (S. C. Singhal and Kendall, 2003). SOFC anode is a porous structure with ion-conducting phase, electron-conducting phase and pores (void phase). The overall electrochemical reactions in SOFC electrodes comprise of several steps such as gas adsorption, surface diffusion of the adsorbed species, the transport of the charged species, and the charge-transfer reaction (Janardhanan and Deutschmann, 2007). The involved species in the overall electrochemical reaction are electrons, ions and gaseous reactants (e.g. hydrogen and oxygen). Thus, the electrochemical reaction occurs at those sites where these three species can co-exist. These sites are called triple phase boundary (TPB) where the ionic conducting phase of YSZ, the electronic conduction of Ni and void phase transport the oxygen ions, electrons and gas species of H_2O and H_2. Only those TPBs that belong to a connected or percolated network can be counted as active sites for electrochemical reaction. The percolated network refers to a connected globally continuous path for ionic or electronic conduction. Increase in the TPB length is desirable for better SOFC performance. However maximizing the TPB might decrease the performance by decreasing the percolated phases (Kenney *et al*., 2009). Thus, TPB length is an important parameter in optimizing the cell electrochemical performance and it can be tuned by microstructural properties of the porous anode. (Farhad and Hamdullahpur, 2012).

Figure 1-2 shows the schematic diagram of SOFC porous anode with a close-up of triple phase

boundary (TPB).

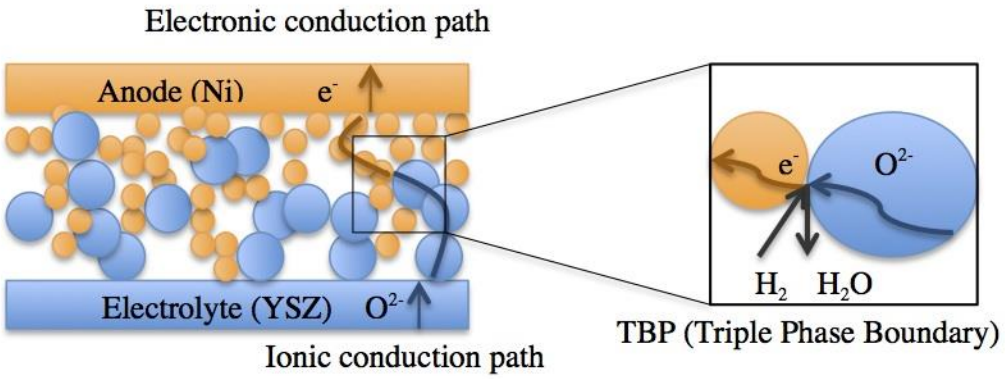

Figure 1-2: Schematic diagram of SOFC porous anode with a close-up of TPB

1.1.2 Fuels and solid oxide fuel cells

Due to high operational temperatures of solid oxide fuel cells and their ability for internal reforming, they can use a variety of hydrocarbon fuels with a simple pre-reforming system or even without reforming. This improves the fuel efficiency and reduces the capital cost of the fuel cell system. However, fuel impurities in hydrocarbon fuels can cause degradation of cell performance (Haga *et al*., 2008). Natural gas being the most convenient hydrocarbon fuel for the SOFC can contain H_2S impurities ranging from 1 to 30 ppm. Coal syngas, the product of coal gasification can also contain high levels of H_2S ranging from 0.2 to 1.3 mole percent (Larminie and Dicks, 2003). The major impurity of the SOFC fuels is H_2S. Even at ppm levels, H_2S in fuel can adversely affect the performance of SOFC by poisoning the Ni catalyst in anode. Understanding the sulfur poisoning and its effect on the SOFC performance are crucial for the SOFC technology improvements and commercialization. (Sasaki *et al*., 2006)

Ni is one of the widely used catalysts in many important catalytic processes that can be poisoned by H_2S, a common sulfur-poisoning component in these processes. Therefore, sulfur poisoning of

the Ni catalyst by H_2S had been vastly studied. In addition to that, the effect of sulfur poisoning of Ni anode on the SOFC performance had also been studied.

1.1.3 Ni catalyst and Sulfur poisoning

In general, poisoning is the chemisorption of impurities on the active sites available for catalysis. In addition to the physically blocking of adsorption sites, adsorbed poisons may modify the electronic structure or the chemical nature of the surface and consequently affect the catalyst performance (Forzatti and Lietti,1999). The relevant work on sulfur poisoning of Ni includes experimental studies, empirical models and density functional theory (DFT) based theoretical studies.

Experimental studies on Ni sulfur poisoning

The nature of chemisorption of sulfur on Ni had been studied by a variety of experimental techniques such as spectroscopy, volumetric, gravimetric, and magnetic measurements (Bartholomew *et al.*, 1982). Different mechanisms suggesting different numbers of bonds of H_2S on Ni surface upon adsorption were proposed by these studies. Four site mechanism with one sulfur bonding to two Ni atoms and two hydrogen, each bonding to one Ni atom at temperature range of 273ºK - 393ºK were proposed by Den Besten and Selwood (1962) and three site mechanism with one sulfur bonding to one Ni atom and two hydrogen each bonding to one Ni atom at temperature range of 193 ºK -373 ºK were proposed by Saleh *et al.* (1961). Based on the aforementioned suggestions, the S/Ni ratio will be 0.25 and 0.33 for the four site and three site mechanisms, respectively. The discrepancy in the S/Ni ratio arises from different temperature and pressure ranges that the experiments were performed at and as a result, different sulfur coverage values were proposed. As the adsorption of H_2S on Ni is an exothermic reaction, it is dependent on the temperature. Higher operating temperature would result in lower sulfur coverage and S/Ni stoichiometry. Sulfur coverage is also dependent on the partial pressures of H_2S, H_2 and therefore

P_{H2S}/P_{H2} ratio. Sulfur coverage would increases with the increase in P_{H2S}/P_{H2} ratio. Therefore, higher equilibrium sulfur coverage and S/Ni stoichiometry are reported at higher P_{H2S}/P_{H2} (Calvin H. Bartholomew, 2001).

Models for sulfur poisoning of Nickel by H_2S:

Models such as Langmuir isotherm have been used to describe the H_2S adsorption on Ni surface. It relates the surface coverage (fraction of the surface covered by adsorbate species) to the partial pressure of gas species exposed to the surface. In such a model, it is assumed that the adsorption proceeds to a monolayer with an increase in concentration, all sites are equivalent and the adsorption is independent of the occupation of the neighbouring sites, meaning that adsorption is independent of the coverage. Langmuir isotherm is not applicable for the cases of having more than one species or having chemical reactions (Kee *et al*., 2003). The first deficiency of the Langmuir isotherm is that it does not consider the dependency of the H_2S adsorption on the coverage. It was shown by some experimental studies that the H_2S heat of adsorption is dependent on coverage, (McCarty and Wise, 1980; Alstrup *et al.*, 1981)) confirming the dependency of H_2S adsorption on coverage. Here, heat of adsorption refers to the heat of adsorption per mole of H_2S adsorbed. Another deficiency of the Langmuir isotherm is that it does not consider the competitive adsorption of hydrogen on the Ni surface. In the experimental studies of the H_2S chemisorption on the Ni surface that were performed with a mixture of H_2 and H_2S feed, it was shown that the competitive adsorption of hydrogen on the Ni surface plays an important role on the sulfur coverage and S/Ni stoichiometry (Bartholomew *et al.*, 1982).

In another study, a Temkin-like isotherm was proposed by fitting the isotherm to the adsorption and desorption data. In this expression the equilibrium H_2S: H2 ratios are correlated to entropy that is independent of coverage and enthalpy that is linearly dependent on coverage. This isotherm does consider the dependency of the adsorption on the coverage but it does not consider

the competitive adsorption of the hydrogen on the Ni surface (Alstrup *et al.*, 1981).

Density functional theory (DFT) studies on sulfur poisoning of Ni by H_2S:

There had also been numbers of theoretical studies that have employed density functional theory (DFT) for examination of the chemisorption of H_2S on Ni surface. In a number of these studies, the adsorption energy was calculated as a function of coverage. However, these models have some deficiencies. In a DFT-based model of Wang and Liu (2007), the competitive adsorption of H_2 on Ni surface is ignored. In addition, the activity of adsorbed species, thermal corrections to the free energy and entropy of all surface species are not considered. In another DFT-based model from Galea *et al.* (2007), thermal corrections of the reaction enthalpy is ignored by assuming that the translational and rotational entropy of the gas species is lost on adsorption. In the DFT based model by Monder and Karan (2010) the competitive adsorption of H_2 on Ni surface was considered along with the activities and complete thermal corrections for adsorbate species calculated form vibrational analysis. The coverage dependent energetic (entropy and enthalpy) with thermal corrections are obtained from this model. One of the common limitations of these studies is that the computations are typically carried for a given crystal facet, e.g. Ni(111) and does not necessarily account for the distributions of various facets in a nanoparticle or the activity at the defect sites and at the edge.

1.1.4 SOFC Performance and H_2S Poisoning

In a SOFC operation, sulfur from H_2S in the fuel can be adsorbed on the Nickel surface in anode and cause sulfur poisoning. This would adversely affect the Ni performance as the electro-catalyst of SOFC and will eventually decrease the performance of SOFC. Studies on the effect of sulfur poisoning of Ni anode on the SOFC performance include the experimental, empirical and modeling studies.

Experimental studies on the SOFC performance and H_2S poisoning:

There have been many experimental works on the effect of the sulfur poisoning on the performance of the SOFC. All these experimental studies show that the loss in the SOFC performance increases by the increase in the H_2S concentration in the anode feed being a mixture of H_2 and H_2S. These experiments had been performed at different temperatures, feed mixtures with different components. Some feeds contained H_2O or N_2 in addition to H_2. The experiments were also performed on different samples such as bottom cells or stacks of solid oxide fuel cells.

In some experimental studies the effect of temperature have also been examined. The experiments had been performed on different feed mixtures with different components such as H_2O or N_2 in addition to H_2. The experiments were also performed on different samples such as button cells or stacks. The results show that the performance of the SOFC degrades when H_2S is added to the H_2 containing fuel due to the sulfur poisoning effect. Table 1-1 shows the different experimental studies on the SOFC at different test conditions, geometries and anode composition with the corresponding loss in performance due to the sulfur poisoning.

Table 1-1:List of some sulfur poisoning experimental studies on SOFC with Ni/YSZ anode

Group	Sample/Cell type	Anode Composition	Measuring conditions	Temperature (ºC)	Fuel	H_2S concentration (ppm)	Loss
Feduska and Isenberg (1983)	7-cell stack	-	Constant current of 150 (mA/cm2)	1000 ºC	10%CO, 5%H_2, 85%CO_2	50 ppm	5% loss in cell voltage
Haga *et al*. (2008)	Button cell-electrolyte support	Ni–ScSZ cermet anode	Constant current density of 0.2 (A/cm2)	800, 900, 1000	97% H_2, 3% H_2O	5 ppm	Voltage drop of 80, 35, and 15 (mV) from the initial voltage of 1000 mV
Matsuzaki and Yasuda (2000)	Button cell-Ni–YSZ cermet electrode and a YSZ electrolyte	Porosity: 40 % YSZ: 10 % (wt)	Constant current density of 0.3 (A/cm2)	750, 900, 1000	79% H_2, 21% H_2O	1-15	Increase of the overvoltage for 2 (mV) at C(H_2S) of 2 ppm, and 74 (mV) at C(H_2S) of 15 ppm
Zha, Cheng, and Liu (2007)	Button cell-electrolyte supported	-	Constant voltage of 0.3 (V), 0.6(V), 0.7(V), 0.8 (V)	800, 700, 900	50% H_2, 1.5% H_2O, 48.5 N_2	2-50	15.5%, 18.5 % and 32.2 % drop in current density at 0.3(V), 0.6 (V) and 0.8 (V), at C (H_2S) of 50 ppm.15.5 % drop in current density at 0.7 (V), at C (H_2S) of 2 ppm.

Group	Sample/Cell type	Anode Composition	Measuring conditions	Temperature (ºC)	Fuel	H_2S concentration (ppm)	Loss
(Cheng, Zha, and Liu 2007)	Button cell	-	Constant current density of 241 (mA/cm^2) and 409 (mA/cm^2) and constant voltage of 0.535(V) and 0.7 (V)	800	50% H2, 1.5% H2O, 48.5 N2	0-10	14% and 8% drop in cell power at 0.409 mA/cm^2) and 241 (mA/cm^2) at C (H_2S) of 10 ppm. 15% and 13% drop in cell power at 0.535(V) and 0.7 (V) at C (H_2S) of 10 ppm.
Rasmussen and Hagen (2009)	1-cell stack	Ni/YSZ anode support-active Ni/YSZ anode	Constant current density of 1000 (mA/cm^2) and	850	4% H_2O, 96 H_2	2-100	Initial cell voltage drop of 13.5 % and 14.5 % at C(H_2S)=10 ppm and C(H_2S)=100 ppm
(Sasaki *et al*. (2006)	Button cells_ electrolyte based Ni-YSZ anode. Electrode thickness: 30 Micro meter		Constant current density of 200 (mA/cm^2)	1000, 900, 850	Various H_2/ H_2O, N_2	1,2,3, 5,10, 20	0.18 (V) and 0.5 (V) Voltage drops at 200 (mA/cm^2), at C(H_2S)=5 at 1000 ºC and 850 ºC.

Group	Sample/Cell type	Anode Composition	Measuring conditions	Temperature (ºC)	Fuel	H_2S concentration (ppm)	Loss
Li and Wang (2011)	Anode supported planar	Anode, Anode support layer and electrolyte thicknesses: 10,400,10 μm	250 (mA/cm^2) and 500 (mA/cm^2)	800		2000	0.18 (V) and 0.287 (V) Voltage drops at 250 (mA/cm^2) and 500 (mA/cm^2)

Empirical models for SOFC performance and H_2S poisoning:

Some empirical models had been proposed to predict the loss in the SOFC performance as a result of sulfur poisoning of Nickel anode catalyst. In an empirical model proposed by Hansen (2008), the loss in cell performance is correlated to the sulfur coverage. In this model, the Temkin-like isotherm proposed by Alstrup *et al*, (1981) and the experimental data of the loss in SOFC performance by Zha *et al.* (2007) were used to derive this correlation. The main deficiency of this model is that it is based on the Temkin like isotherm that does not consider the competitive adsorption of the H_2 on Ni surface. Another problem with this model is that it calculates the loss in the performance based on experimental results at a constant cell voltage of 0.7 (V), which makes their derived correlation valid only for this voltage. At different cell voltages, the concentration profiles of the H_2 and H_2S in SOFC anode will be different. Therefore, sulfur coverage profile will be different. The validity of this correlation was not verified at different cell voltages. Another empirical model is the damage model for degradation of the SOFC anode. This degradation model investigates the effects of sulfur poisoning on the performance loss. It is developed based on applying a damage factor to the TPB length in anode as the TPB length is considered as the most appropriate parameter presenting the degradation due to the sulfur poisoning (Ryan *et al.,* 2012). The experimental data of Zha *et al.* (2007) were used to develop a damage factor as a function of H_2S concentration and Temperature.

1.1.5 Anode models with H_2S poisoning effect on the SOFC performance

A number of models for porous anode have been reported including those by Yakabe et al. (2000), Zhu and Kee (2008) and Hussain *et al.* (2007). These models have examined the effects of anode structure and microstructure as well as the operating conditions. However, none of the models have considered the effect of sulfur poisoning kinetics while coupling the transport effects. One model that has considered localized transport effects is the "near triple-phase boundary region model for H_2S poisoning of SOFC anodes" (Monder and Karan, 2011). It is a one-dimensional anode model for patterned Ni-YSZ anode that considers the H_2S dissociative adsorption reaction on the surface, in addition to the all gas-surface and

electrochemical reactions. This model only considers the surface transport of the adsorbed species and ignores the gas species transport effects by assuming that the fuel composition is uniform over the model domain. The DFT-based thermodynamic results of the competitive adsorption of H_2S on Ni surface (Monder and Karan, 2010) is adopted for the kinetic formulation of this model. The effect of the sulfur poising on the SOFC performance is presented by polarization curve at different H_2S concentrations and relative performance loss at different PH_2S/PH_2 values. There are no distributed porous anode models in the literature to evaluate the effect of sulfur poisoning on the SOFC performance. Once the modified kinetics of the anode electrochemical reaction in the presence of H_2S is established, it can be implemented in a porous anode model to evaluate the effect of sulfur poisoning on the SOFC performance.

1.1.6 Motivation and Objective

The goal of this thesis is to model the effect of sulfur poisoning on the electrochemical performance of the SOFC with Ni-YSZ porous anode. To achieve this goal, the objective of this thesis is to develop a numerical, two-dimensional kinetic-transport with distributed charge transport model of a SOFC cell with Ni-YSZ porous anode that can predict the electrochemical performance of the cell exposed to a H_2 rich fuel with H_2S impurities. This objective is fulfilled in 2 steps:

- In the first step, a kinetic formulation that takes into account the reaction of H_2S with Ni catalyst (sulfur poisoning) in addition to the H_2 electro-oxidation reaction is derived. This new formulation captures the effect of sulfur poisoning on the SOFC performance by incorporating the PH_2S (partial pressure of the H_2S) in a Butler-Volmer type formulation.
- In the second step, the new Butler-Volmer type equation is incorporated in a two-dimensional transport half-cell model with porous Ni-YSZ anode. This two-dimensional model considers the gas species gradients as well as the electric potential, ionic potential, pressure and velocity gradients. With the help of this model, the effect of transport phenomena on the kinetics of electrochemical reaction of the SOFC can be investigated.

1.2 Layout of the thesis

In chapter 2, the development of the novel kinetic formulation of H_2 electro oxidation reaction in the presence of H_2S is presented. The new Butler-Volmer type formulation is further extended to take into account the coverage dependency of the energetics of the reactions.

Chapter 3 presents the development of the multiphysics electrochemical performance model including the description of model equations for all the transport phenomena and detailed electrochemistry. The novel kinetic formulation developed in Chapter 2 is implemented in the multiphysics model and the results are compared with some experimental studies.

Chapter 4 gives a summary of the results and some recommendation for future works.

Chapter 2

Kinetic model for hydrogen electro-oxidation of Ni/YSZ-anodes accounting for sulfur poisoning

Chapter two presents the derivation of the *kinetic formulation* for the H_2 electro-oxidation in the Ni-based anodes of SOFC in the presence of H_2S. The kinetic model is derived considering *elementary kinetic modeling* that considers several elementary reaction steps. A modified Butler-Volmer type expression is obtained that captures the effect of the sulfur poisoning on the H_2 electro-oxidation. Two types of kinetic models, differing in the coverage dependency of energy of adsorption, are reported. The first model is based on a Langmuir-type adsorption isotherm for both H_2S and H_2 adsorption reactions. Thus, in this model the energetics of the adsorption reactions is *independent of the coverage of adsorbed species* and it is named as "coverage independent Butler-Volmer type kinetic model with sulfur poisoning". The second model considers the dependency of the adsorption energetics on the surface coverage of the adsorbed species. This kinetic model is called "coverage-dependent Butler-Volmer type kinetic model with sulfur poisoning". For each kinetic model a thermodynamic section to derive the corresponding equilibrium constants of H_2S and H_2 adsorption reactions are also considered. In the last section, coverage dependent and coverage independent kinetic models are compared in terms of predicted reduction in current density. Figure 2-1 summarizes the kinetic models that are presented in this chapter:

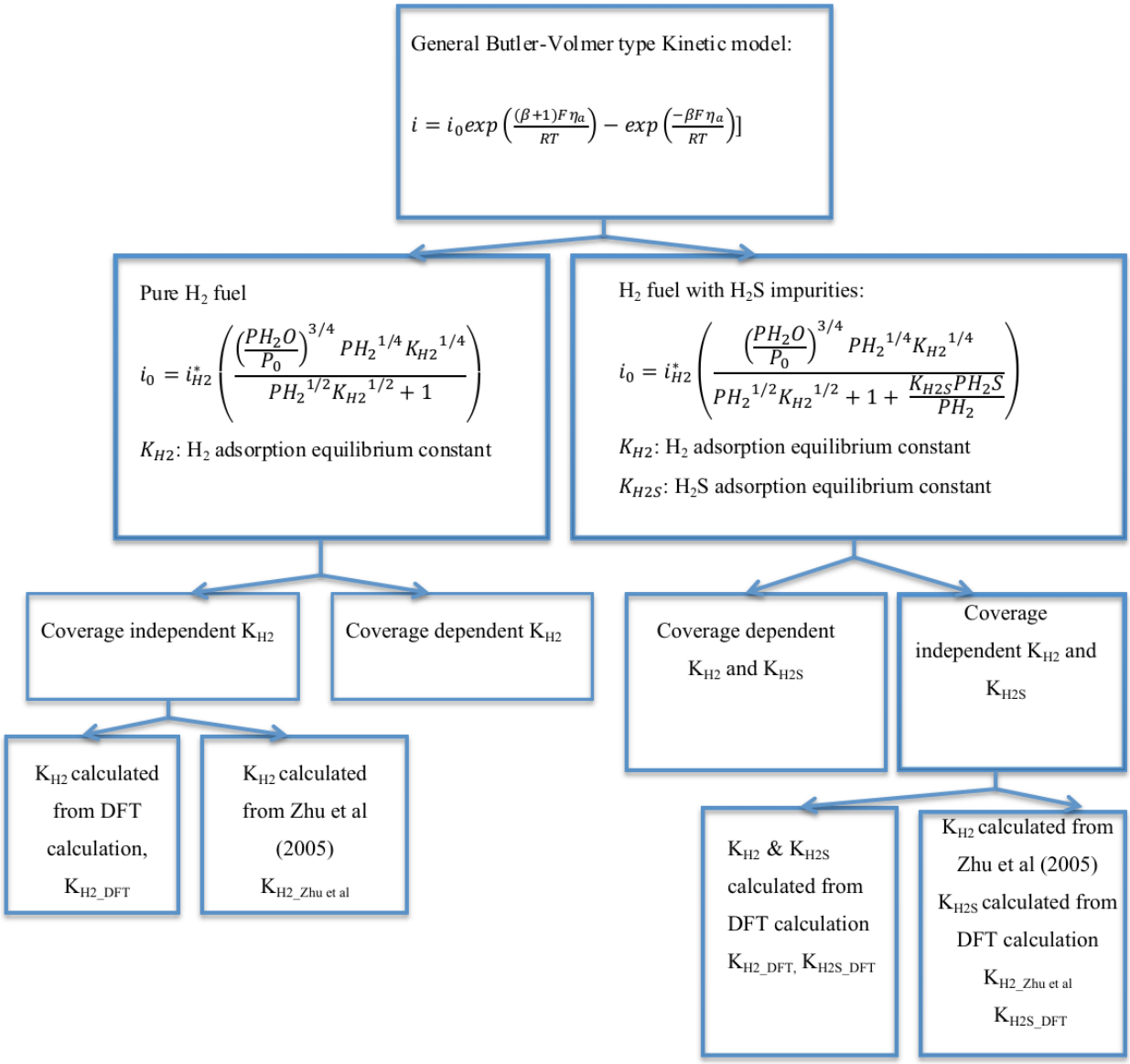

Figure 2-1: Kinetic models that are developed in Chapter 2

2.1 Introduction

Different approaches have been developed to model the hydrogen electrochemical reactions in the Ni-based SOFC anodes. These range from nanoscopic scale (quantum chemistry, molecular dynamics) to mesoscopic scale (elementary kinetics) to macroscopic scale (empirical global kinetics) models. In nanoscopic scale model, density-functional theory (DFT) is used for *ab initio* thermodynamics calculation

such as studying the hydrogen spillover (Shishkin and Ziegler, 2009). *ab initio* refers to the result obtained from DFT as it does not rely on empirical or fitted parameters. Elementary kinetics describes the chemical reaction by the elementary reaction steps. The mass action law is used for the rate of each reaction step (Vogler *et al*., 2009). Mass action law in chemical kinetics defines the rate of a chemical reaction to be proportional to the product of the reactants. Elementary kinetic models can be coupled to macro-scale kinetic and transport models. Butler–Volmer type global kinetic expression is generally used for macroscopic modeling of SOFC electrode kinetics. This expression lumps all nanoscopic-scale and microscopic-scale reactions and some of the surface transport processes (Zhu *et al*., 2005). For such Butler-Volmer type formulation, the current density is expressed as a function of overpotential and is parameterized by fitting to experimental data (Bessler *et al*., 2010).

2.2 Methodology

The detailed analysis proposed by Zhu *et al*. (2005) is adopted to derive a Butler-Volmer formulation from the elementary steps of hydrogen oxidation reaction in the Ni-YSZ three-phase region. The H_2 oxidation reaction include five elementary reactions and had been previously proposed by Boer (1998) . The effect of sulfur poisoning is considered by adding the H_2S adsorption reaction as an elementary reaction to the H_2 elementary step reactions. A Langmuir-type isotherm in which the adsorption energetics is independent of the surface coverage is considered for both H_2 and H_2S adsorption reactions. In the next step, the derived Butler-Volmer type kinetic formulation is further modified to a "coverage-dependent Butler-Volmer type kinetic model" by considering the dependency of the H_2 and H_2S adsorption reaction energetics on the coverage of the adsorbed H and S surface species on Ni surface.

Coverage-independent equilibrium constants are obtained from Zhu *et al*. (2005) approach and DFT calculated energetics by Monder and Karan (2010). Coverage-dependent equilibrium constants are obtained from DFT calculated energetics by Monder and Karan (2013).

2.2.1 Anode electrochemistry with the presence of H_2S

The overall hydrogen oxidation reaction can be expressed as:

$$H_2(g) + \frac{1}{2}O_2(g) \leftrightharpoons H_2O(g) \quad (2.1)$$

For SOFCs, the global half-cell anode reaction can be written as follows:

$$H_2(g) + O_O^X(YSZ) \leftrightharpoons H_2O(g) + V_{\ddot{O}}(YSZ) + 2e^-(Ni) \quad (2.2)$$

The above reaction consists of several elementary steps. In this work, a mechanism comprising five elementary reactions is considered for the hydrogen oxidation in the Ni/YSZ three phase regions (Boer 1998) as reported below.

Adsorption/desorption of hydrogen on Ni surface

$$H_2(g) + 2(Ni) \leftrightharpoons 2H(Ni) \quad (2.3)$$

Charge transfer reactions at the TPB region

$$H(Ni) + O^{2-}(YSZ) \leftrightharpoons (Ni) + OH^-(YSZ) + e^-(Ni) \quad (2.4)$$

$$H(Ni) + OH^-(YSZ) \leftrightharpoons (Ni) + H_2O(YSZ) + e^-(Ni) \quad (2.5)$$

Adsorption/desorption on the YSZ surface

$$H_2O(YSZ) \leftrightharpoons (YSZ) + H_2O(g) \quad (2.6)$$

Transfer of oxygen ions between the surface and the bulk YSZ

$$O_O^X(YSZ) + (YSZ) \leftrightharpoons O^{2-}(YSZ) + V_{\ddot{O}}(YSZ) \quad (2.7)$$

Here, $H(Ni)$, (Ni) and $e^-(Ni)$ are the adsorbed atomic hydrogen, the Ni empty site and the electron within the Ni anode, respectively and $O_O^X(YSZ)$, $V_{\ddot{O}}(YSZ)$, $O^{2-}(YSZ)$, $OH^-(YSZ)$ and $H_2O(YSZ)$ are the lattice Oxygen, Oxygen vacancy within the YSZ, oxygen ion, hydroxide ion and absorbed water molecule on YSZ surface, respectively.

In the presence of H_2S, an additional reaction considering sulfur adsorption on the Ni surface is included:

$$H_2S + (Ni) \leftrightharpoons S(Ni) + H_2(g) \quad (2.8)$$

Hydrogen and sulfur atoms adsorb only on the nickel surface, H_2O and OH^- adsorb on YSZ surface. None of the steps are limited by diffusion or migration of species. That is, all steps are considered to be in

equilibrium and the reaction rate set to zero. To derive the overall reaction rate expression, the pseudo-steady state hypothesis for all steps except the rate-limiting step is considered.

Derivation of the coverage-independent Butler-Volmer type Kinetic model with sulfur poisoning:

The hydrogen oxidation elementary reactions (2.3 through 2.7), in addition to the H_2S adsorption reaction (2.8), are considered for kinetic expression derivation. In this set of reactions, seven surface species and three gas species are involved. By definition, the sum of site fractions on the Ni and YSZ surfaces should be unity:

$$\theta_H + \theta_{Ni} + \theta_S = 1 \tag{2.9}$$

$$\theta_O + \theta_{OH} + \theta_{H2O} + \theta_{YSZ} = 1 \tag{2.10}$$

The site fractions of the surface species are defined as follows: θ_H is the adsorbed atomic hydrogen on the Ni surface, θ_{Ni} is an empty site on the Ni; θ_S is the adsorbed atomic sulfur on the Ni surface. $\theta_O, \theta_{OH}, \theta_{H2O}$ and θ_{YSZ} represent the $O^{2-}(YSZ)$, $OH^{-}(YSZ)$, $H_2O(YSZ)$ and an empty site on the YSZ surface. Following the approach of Zhu et al. (2005), the second step of the charge transfer reaction (reaction 2.5) is considered rate limiting. Other fast reactions are in pseudo-equilibrium and the species activities can be obtained from the equilibrium constants of fast reactions and reaction rate constant of reaction 2.5. In the following relations, and K_1, K_2 K_4, K_5, and K_6 correspond to the equilibrium constants of reactions 2.3, 2.4, 2.6, 2.7 and 2.8. Adsorption of H_2 and H_2S are described by the Langmuir-type isotherm with the reaction energetics being independent of the surface coverage.

$$\frac{\boldsymbol{\theta_H^2}}{\boldsymbol{\theta_{Ni}^2 P_{H2}}} = \boldsymbol{K_1} \tag{2.11}$$

$$\frac{\theta_{Ni}\theta_{OH}}{\theta_H\, \theta_O} = K_2\ exp\left(\frac{FE_a}{RT}\right) \tag{2.12}$$

$$\frac{\theta_{YSZ}\, P_{H2O}}{\theta_{H2O}} = K_4 \tag{2.13}$$

$$\frac{\theta_O}{\theta_{YSZ}} = K_5 \tag{2.14}$$

$$\frac{P_{H2}\, \theta_S}{\theta_{Ni}\, P_{H2S}} = K_6 \tag{2.15}$$

Reaction 2.4 is a charge-transfer reaction considered to be in equilibrium. Therefore, E_a representing the difference between the electric potential ($\emptyset_{\mathrm{el}}$) and ionic potential ($\emptyset_{\mathrm{ion}}$) of electrode appears in its relation.

The rate of the charge-transfer reaction can be expressed in terms of rate of electrons generated or current. Flux of charge-transfer or the current density of the rate limiting reaction (2.5) can be written as follows:

$$i = l_{TPB}F\left(k_{3,a}\theta_H\theta_{OH}\,exp\left(\frac{\beta_{3,a}\,FE_a}{RT}\right) - k_{3,c}\theta_{H2O}\theta_{Ni}\,exp\left(\frac{-\beta_{3,c}\,FE_a}{RT}\right)\right) \tag{2.16}$$

with $k_{3,a}$and $k_{3,c}$ being the anodic and cathodic thermal rate constants (functions of temperature) $\beta_{3,a}$ and $\beta_{3,c}$ are the anodic and cathodic symmetry factors. l_{TPB} is the TPB length in anode.

By considering the constraint that the sum of surface coverages is equal to one and after some algebraic manipulations, species site fractions on the YSZ surface can be derived in terms of gaseous partial pressures and surface coverages of Ni and hydrogen (θ_H, θ_{Ni}). Site fraction of species on the YSZ surface (θ_{H_2O}, θ_{YSZ}, θ_O and θ_{OH}) in terms of θ_H and θ_{Ni} are presented as below.

$$\theta_{H_2O} = \frac{P_{H_2O}}{P_{H2O}+K_4+{K_4}/{K_5}+\left({\theta_H}/{\theta_{Ni}}\right)K_2\exp\left({FE_a}/{RT}\right)K_4/K_5} \tag{2.17}$$

$$\theta_{YSZ} = \frac{K_4}{P_{H2O}+K_4+{K_4}/{K_5}+\left({\theta_H}/{\theta_{Ni}}\right)K_2\exp\left({FE_a}/{RT}\right)K_4/K_5} \tag{2.18}$$

$$\theta_O = \frac{K_4/K_5}{P_{H2O}+K_4+{K_4}/{K_5}+\left({\theta_H}/{\theta_{Ni}}\right)K_2\exp\left({FE_a}/{RT}\right)K_4/K_5} \tag{2.19}$$

$$\theta_{OH} = \frac{\left({\theta_H}/{\theta_{Ni}}\right)K_2\exp\left({FE_a}/{RT}\right)K_4/K_5}{P_{H2O}+K_4+{K_4}/{K_5}+\left({\theta_H}/{\theta_{Ni}}\right)K_2\exp\left({FE_a}/{RT}\right)K_4/K_5} \tag{2.20}$$

By substituting the surface coverages in the current density expression (equation 2.16) and further algebraic manipulation, an expression for current density in terms of the equilibrium constants (2.11 – 2.15) is obtained. The anodic and cathodic parts of the current density can be written as:

$$i_a = l_{TPB}F(k_{3,a}\theta_H\frac{\left({\theta_H}/{\theta_{Ni}}\right)K_2\exp\left({FE_a}/{RT}\right)K_4/K_5}{P_{H2O}+K_4+{K_4}/{K_5}+\left({\theta_H}/{\theta_{Ni}}\right)K_2\exp\left({FE_a}/{RT}\right)K_4/K_5}\exp\left(\frac{\beta_{3,a}\,FE_a}{RT}\right)) \tag{2.21}$$

$$i_c = l_{TPB}F(k_{3,a}/K_3\,\theta_{Ni}\frac{P_{H_2O}}{P_{H2O}+K_4+{K_4}/{K_5}+\left({\theta_H}/{\theta_{Ni}}\right)K_2\exp\left({FE_a}/{RT}\right)K_4/K_5}\exp\left(\frac{-\beta_{3,c}\,FE_a}{RT}\right)) \tag{2.22}$$

By assuming that the YSZ surface is fully covered with adsorbed oxygen ions we have $\theta_O \approx 1$, the current density expression can be simplified to:

$$i_a = l_{TPB}F(k_{3,a}\theta_H \frac{\frac{K_4K_2}{K_5}\left(\theta_H/\theta_{Ni}\right)\exp\left(FE_a/RT\right)}{K_4/K_5} \exp\left(\frac{\beta_{3,a}\,FE_a}{RT}\right)) \quad (2.23)$$

$$i_c = l_{TPB}F(\frac{k_{3,a}}{K_3}\theta_{Ni}\frac{P_{H2O}}{(K_4/K_5)}\exp\left(\frac{-\beta_{3,c}\,FE_a}{RT}\right)) \quad (2.24)$$

Further, by substituting the term θ_H from equation 2.11, combining the exponential terms in the numerator and some further algebraic manipulations, the relations shown below are obtained:

$$i_a = l_{TPB}Fk_{3,a}K_1K_2\,P_{H2}\;\theta_{Ni}\exp\left(\frac{(\beta_{3,a}+1)FE_a}{RT}\right)) \quad (2.25)$$

$$i_c = l_{TPB}F(\frac{k_{3,a}}{K_3}\theta_{Ni}\frac{P_{H2O}}{(K_4/K_5)}\exp\left(\frac{-\beta_{3,c}\,FE_a}{RT}\right)) \quad (2.26)$$

$$i = l_{TPB}Fk_{3,a}\theta_{Ni}\;\left[K_1K_2P_{H2}\exp\left(\frac{(\beta_{3,a}+1)FE_a}{RT}\right) - \frac{P_{H2O}}{K_3\,(K_4/K_5)}\exp\left(\frac{-\beta_{3,c}\,FE_a}{RT}\right)\right] \quad (2.27)$$

The next step is arranging the current density in the form of Butler-Volmer equation expressed by equation (2.28).

$$i = i_0[exp\left(\frac{(\beta_{3,a}+1)F\eta}{RT}\right) - exp\left(\frac{-\beta_{3,c}\,F\eta}{RT}\right)] \quad (2.28)$$

Activation overpotential (η_a) represents the difference between E_a (local difference between the potential of electronic phase and potential of ionic phase) and E_a^{eq}(local equilibrium potential difference between the electronic phase and the ionic phase).

$$\eta_a = E_a - E_a^{eq} \quad (2.29)$$

In order to arrange the current density in the form of Butler-Volmer equation, E_a^{eq} should be found. By setting the current density (i) from equation (2.27) to zero and some further algebraic manipulations, E_a^{eq} can be calculated.

$$E_a^{eq} = \frac{-RT}{2F}\ln\left(\frac{K_3K_2K_1K_4}{K_5}\,\frac{P_{H2}}{P_{H2O}}\right) \quad (2.30)$$

By assuming that $\beta_{3,a} + \beta_{3,c} = 1$, further restriction of $\beta_{3,c} = 0.5$ (Zhu et al. 2005), and more algebraic manipulations, the current density expression formulated in Butler-Volmer form is found as:

$$i = l_{TPB} F k_{3,c} (K_3 K_2 K_1)^{1/4} (\frac{K_5}{K_4})^{\frac{3}{4}} (\theta_{Ni}) {P_{H2O}}^{\frac{3}{4}} {P_{H2}}^{1/4} [exp\left(\frac{(\beta_{3,a}+1)F\eta}{RT}\right) - exp\left(\frac{-\beta_{3,c}F\eta}{RT}\right)] \quad (2.31)$$

In the above expression, the terms outside the square brackets are lumped together to define exchange current density (i_0) as follows:

$$i_0 = l_{TPB} F k_{3,c} (K_3 K_2 K_1)^{1/4} (\frac{K_5}{K_4})^{\frac{3}{4}} (\theta_{Ni}) {P_{H_2O}}^{\frac{3}{4}} {P_{H_2}}^{1/4} \quad (2.32)$$

Deriving an expression for θ_{Ni} from equilibrium constants and surface coverage constraint on Ni and substituting into equation above yields the final relation for i_0:

$$\frac{\theta_H}{\theta_{Ni}} + 1 + \frac{\theta_S}{\theta_{Ni}} = \frac{1}{\theta_{Ni}} \quad (2.33)$$

$$\frac{\theta_H}{\theta_{Ni}} = {P_{H_2}}^{1/2} {K_1}^{1/2} \quad (2.34)$$

$$\frac{\theta_S}{\theta_{Ni}} = \frac{K_6 P_{H_2} S}{P_{H_2}} \quad (2.35)$$

$${P_{H_2}}^{1/2} {K_1}^{1/2} + 1 + \frac{K_6 P_{H_2} S}{P_{H_2}} = \frac{1}{\theta_{Ni}} \quad (2.36)$$

$$i_0 = l_{TPB} F k_{3,c} (K_3 K_2 K_1)^{1/4} (\frac{K_5}{K_4})^{\frac{3}{4}} . \left(\frac{1}{{P_{H_2}}^{1/2} {K_1}^{1/2} + 1 + \frac{K_6 P_{H_2} S}{P_{H_2}}}\right) {P_{H2O}}^{\frac{3}{4}} . {P_{H2}}^{1/4} \quad (2.37)$$

$$i_0 = l_{TPB} F k_{3,c} (K_3 K_2)^{\frac{1}{4}} (\frac{K_5}{K_4})^{\frac{3}{4}} . P_0^{\frac{3}{4}} \left(\frac{\left(\frac{P_{H2O}}{P_0}\right)^{\frac{3}{4}} {P_{H_2}}^{1/4} {K_1}^{1/4}}{{P_{H_2}}^{1/2} {K_1}^{1/2} + 1 + \frac{K_6 P_{H_2} S}{P_{H_2}}}\right) \quad (2.38)$$

Since there are two charge-transfer reactions, the overall current density is twice the current density and is obtained as indicated below:

$$i_0 = 2 l_{TPB} F k_{3,c} (K_3 K_2)^{1/4} (\frac{K_5}{K_4})^{3/4} P_0^{3/4} \left(\frac{\left(\frac{P_{H2O}}{P_0}\right)^{\frac{3}{4}} {P_{H_2}}^{1/4} {K_1}^{1/4}}{{P_{H_2}}^{1/2} {K_1}^{1/2} + 1 + \frac{K_6 P_{H_2} S}{P_{H_2}}}\right) \quad (2.39)$$

With all the constants and equilibrium constants lumped into i_{H2}^{*} parameter, the exchange current density can be written as follows:

$$i_{H2}^{*} = 2l_{TPB}Fk_{3,c}\,(K_3K_2)^{1/4}\,(\frac{K_5}{K_4})^{3/4}\,P_0^{3/4} \tag{2.40}$$

$$i_0 = i_{H2}^{*}\left(\frac{\left(\frac{P_{H2O}}{P_0}\right)^{\frac{3}{4}}{P_{H_2}}^{1/4}{K_1}^{1/4}}{{P_{H_2}}^{1/2}{K_1}^{1/2}+1+\frac{K_6P_{H_2S}}{P_{H_2}}}\right) \tag{2.41}$$

The volumetric exchange current density (i_0) is a function of i_{H2}^{*} (exchange current factor), local adsorption equilibrium constants, local partial pressure of gas species and local surface coverage. Exchange current factor is a function of TPB length, rate and equilibrium constant of the elementary steps of the hydrogen oxidation reaction. K_1 (also referred as K_{H2}) is the equilibrium constant of the H_2 adsorption. K_6, (also referred as K_{H2S}) is the equilibrium constant of H_2S adsorption. In the coverage-independent model K_{H2} and K_{H2S} vary with temperature but are independent of the species coverage. Calculations of these constants are shown in next section of thermodynamics of H_2 and H_2S adsorption with coverage-independent energies.

Calculation of exchange current density factor:

Exchange current density factor is often treated as an empirical parameter that can be adjusted to fit the measured cell performance. Its dependency on the temperature can be expressed as:

$$i_{H2}^{*} = i_{ref,H2}^{*}\exp[-\frac{E_{a,H2}}{R}\left(\frac{1}{T}-\frac{1}{T_{ref}}\right)] \tag{2.42}$$

The empirically obtained value reported by Zhu and Kee (2008) at T_{ref} =800 ºC is used as reference exchange current density factor ($i_{ref,H2}^{*}$) to calculate i_{H2}^{*} at other temperatures. $E_{a,H2}$ is an activation energy. $i_{ref,H2}^{*}$ can be normalized with respect to the reference TPB length (calculated from Zhu and Kee, 2008) to be only a function of rate and equilibrium constants. The normalized $i_{ref,H2}^{*}$ can then be multiplied by the TPB length per unit volume to obtain the $i_{ref,H2}^{*}$ corresponding to our model. TPB length is calculated from the coordination theory with the details explained in Appendix A. The calculated

TPB length from Zhu and Kee (2008) and TPB length from our model have the same value. Therefore, $i^*_{ref,H2}$ of our model is also equal to $i^*_{ref,H2}$ of Zhu and Kee (2008).

2.2.2 Thermodynamics of H_2 and H_2S adsorption on Ni: Coverage-independent energies

The equilibrium constant for adsorption of gases or liquids on solid surfaces are not readily available or computed, e.g. via the use of tabulated Gibbs energy. The reason is that energies of the adsorbed species are not available or easily computed. In this work, the coverage-independent kinetic model requires the calculation of K_{H2} and K_{H2S}. The equilibrium constant of H_2 adsorption reaction is calculated based on two different approaches. The first approach is based on the formulation/expression reported by Zhu *et al.*(2005), which is reported below:

$$K_{H2} = \frac{\gamma_0}{A_{des}\Gamma^2\sqrt{2\pi RTW_{H2}}}.\exp(\frac{E_{des}}{RT}) \quad (2.43)$$

With $E_{des}, A_{des}, \gamma_0$ and Γ being the activation energy for the H_2 desorption reaction, pre-exponential factor, sticking coefficient and the surface site density. The calculated value of K_{H2} at T=700 ºC is 1.409×10^{-5} $\frac{1}{Pa}$. The second approach is to obtain the equilibrium constants of H_2 and H_2S adsorption from DFT based calculations proposed by Monder and Karan (2010). DFT based estimation of K_{H2} and K_{H2S} are presented in the next section.

DFT based estimation of equilibrium constants for H_2S and H_2 adsorption reactions:

The equilibrium constant of the H_2S and H_2 adsorption reactions are calculated from *ab initio* adsorption thermodynamics of H_2 and H_2S on Ni (111) (Monder and Karan 2010). The model considered a unit cell of Ni (111) with 2 atom by 2 atom surface denoted as C. Each surface species is a combination of hydrogen and sulfur atoms on C. In the work of Monder and Karan (2010), seven reactions with eight different surface species ($C, C_H, C_{2H}, C_{4H}, C_S, C_{2S}\, C_{2H,S}, C_{2H,2S}$) are considered for the adsorption thermodynamics of H_2 and H_2S on this unit cell C. Each of the seven reactions has a different free energy due to the different surface species involved in the reaction. Therefore, it could be inferred that the

thermodynamics of the H_2 and H_2S adsorption is implicitly coverage dependent. For this study, among the seven reactions, two reactions were chosen to describe the H_2S adsorption, and one reaction was chosen to present the H_2 adsorption reaction and calculate the K_{H2S} and K_{H2}.

K_{H2S} can be estimated by considering the following reactions on Ni (111) surface:

$$H_2S(g) + C \leftrightharpoons C_{2H,S} \tag{2.44}$$

$$C_{2H,S} \leftrightharpoons H_2 + C_S \tag{2.45}$$

K_{H2} can be estimated by considering the following reaction on Ni (111) surface:

$$\frac{1}{2}H_2(g) + C \leftrightharpoons C_H \tag{2.46}$$

The surface coverage of H and S adsorbed species (θ_H and θ_S) are defined as:

$$\theta_H = \frac{1}{4}\theta_H{}' + \frac{1}{2}\theta'_{2H,S} \tag{2.47}$$

$$\theta_S = \frac{1}{4}\theta_S{}' + \frac{1}{4}\theta'_{2H,S} \tag{2.48}$$

$\theta'_{2H,S}$, $\theta_S{}'$and $\theta_H{}'$ are the surface coverage of $C_{2H,S}$, C_S and C_H species.

Because of the difference in the surface coverage species on the unit cell C and the H and S coverages, and also not considering all the seven reactions, the calculated K_{H2S} and K_{H2} would be different from the *ab initio* thermodynamics results (Monder and Karan 2010). The data from *ab initio* thermodynamics model (Monder and Karan 2010) at 700ºC is used to calculate the free energy of these reactions. The calculated enthalpies include the DFT calculated electronic energy ($E_{el,i}$), zero point vibrational energy ($E_{ZPV,i}$) and thermal corrections($E_{th,i}$).

$$G_i^0 = H_i^0 - TS_i^0 \tag{2.49}$$

$$H_i^0 = E_{el,i} + E_{ZPV,i} + E_{th,i} + PV_{m,i} \tag{2.50}$$

K_{H2S} can be calculated from the energetics of reactions 2.44 and 2.45. $\Delta G^0_{1,H2S,ads}$ and $\Delta G^0_{2,H2S,ads}$ represent the standard Gibbs free energy of the reactions 2.44 and 2.45. $\Delta G^0_{1,H2S,ads} = -0.14\, ev$ and $\Delta G^0_{2,H2S,ads} = -1.22\, ev$. The summation of these two reactions can be used to calculate the free energy for the H_2S adsorption reaction and thereby the associated equilibrium constant, K_{H2S}.

$$H_2S(g) + C \leftrightharpoons H_2 + C_S \tag{2.51}$$

$$\Delta G^0_{H2S,ads} = \Delta G^0_{1,H2S,ads} + \Delta G^0_{2,H2S,ads} = -1.36(\text{ev}) = -131219\frac{J}{mol} \tag{2.52}$$

Here, the activity (a_i) of surface species and gas species is defined as:

$$a_i = \theta_i = \frac{C_i}{C_T} \tag{2.53}$$

$$a_i = \frac{P_i}{P_T} \tag{2.54}$$

K_{H2S} can be written as follows:

$$K_{H2S} = \frac{\theta_S \frac{P_{H2}}{P_0}}{\theta_V \frac{P_{H2S}}{P_0}} = \frac{\theta_S P_{H2}}{\theta_V P_{H2S}} = \exp\left(-\frac{\Delta G^0_{H_2S,ads}}{RT}\right) \tag{2.55}$$

By substituting $\Delta G^0_{H_2S,ads}$, T and R values in the relation above, the value of the K_{H2S} is calculated to be 1.1083×10^7. Similarly, K_{H2} can be calculated from the energetics of reaction 2.46. $\Delta G^0_{H2,ads}$ represents the Gibbs free energy of reaction 2.46 and is equal to $0.14\ ev$ or $13507.94\ \frac{J}{mol}$. Accordingly, the equilibrium constant of reaction 2.46 (K'_{H2}) at T=700ºC is calculated to be:

$$K'_{H2} = \frac{\theta_H}{\left(\frac{P_{H2}}{P_0}\right)^{0.5}\theta_V} = \exp\left(-\frac{\Delta G^0_{H2,ads}}{RT}\right) = 0.188 \tag{2.56}$$

The K_{H2} that we have considered in the derivation of our kinetic model is $K_{H2} = \frac{\theta_H^2}{P_{H2}\theta_V^2}$, therefore:

$$K_{H2} = \frac{(K'_{H2})^2}{P_0} = \frac{\theta_H^2}{P_{H2}\theta_V^2} = \frac{0.188\text{^}2}{101325} = 3.48\times10^{-7}\left(\frac{1}{Pa}\right) \tag{2.57}$$

The DFT-based H_2 and H_2S adsorption equilibrium constants were calculated at 700ºC from the *ab initio* thermodynamics model. For calculation of K_{H2} and K_{H2S} at other temperatures the readers are referred to Monder and Karan (2010).

Calculation of hydrogen and sulfur coverages:

The hydrogen and sulfur coverages are calculated for two cases. In the first case, H coverage is calculated for only H_2 adsorption reaction. In the second case, both H and S coverages are calculated considering the competing H_2 and H_2S adsorption reactions.

1) Hydrogen coverage on Ni in the presence of pure hydrogen gas

The H coverage is calculated by using the DFT based K_{H2} at 700 ºC (K_{H2}=3.48×10^{-7} $\frac{1}{Pa}$) considering Langmuir isotherm and that $\theta_V = 1 - \theta_H$ as follows:

$$\theta_H = (P_{H2}K_{H2})^{0.5}/((P_{H2}K_{H2})^{0.5} + 1) \quad (2.58)$$

From the above expression, it is expected that an increase in P_{H2} and K_{H2} will increase the H coverage.

Figure 2-2 shows the changes of hydrogen coverage as a function of hydrogen partial pressure.

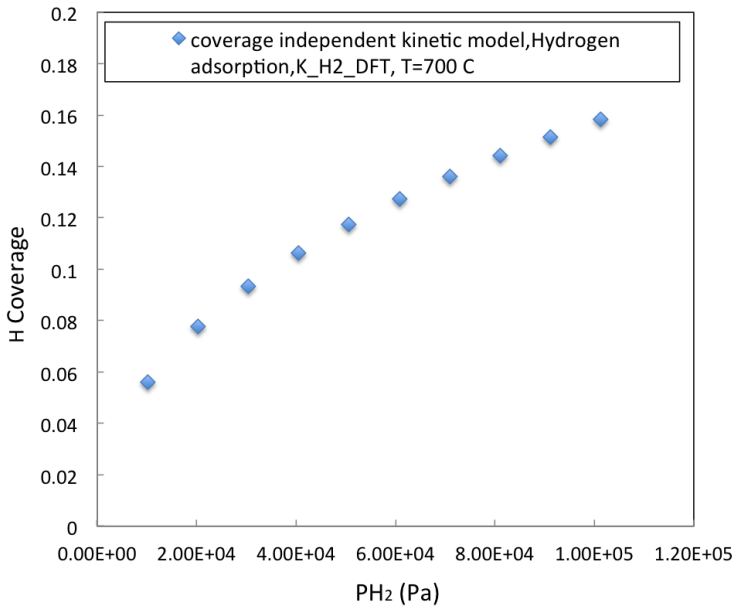

Figure 2-2: Hydrogen coverage as a function of hydrogen partial pressure with pure H_2 adsorption (coverage-independent kinetic model), [T=700 ºC]

It is predicted that the hydrogen coverage changes from 0.0562 to 0.158 by changing the P_{H2} from 0.1 atm to 1 atm.

2) Hydrogen and sulfur coverages from adsorption of a mixture of H_2 and H_2S

The H and S coverages are calculated by using the DFT based estimates of K_{H2} and K_{H2S} at 700 ºC by solving chemical potential equilibrium equations. The results are based on considering the competitive adsorption of H_2 and H_2S on Ni surface. By using the K_{H2} and K_{H2S} formulation and taking the $\theta_V = 1 - \theta_H - \theta_S$, the hydrogen and sulfur coverages can be calculated by solving equations 2.59 and 2.60 simultaneously:

$$K_{H2} = \frac{\left(\frac{\theta_H}{1-\theta_H-\theta_S}\right)^2}{P_{H2}} \tag{2.59}$$

$$K_{H2S} = \frac{\theta_S}{1-\theta_H-\theta_S}\frac{P_{H2}}{P_{H2S}} \tag{2.60}$$

Surface coverages of H and S are calculated at different values of P_{H2S}/P_{H2} for two different total pressures of 0.97 atm and 0.2 atm. Figure 2-3 shows the calculated H and S coverages as a function of P_{H2S}/P_{H2} at $P_{H2} + P_{H2S} = 0.91\ atm$ and $P_{H2} + P_{H2S} = 0.2\ atm$.

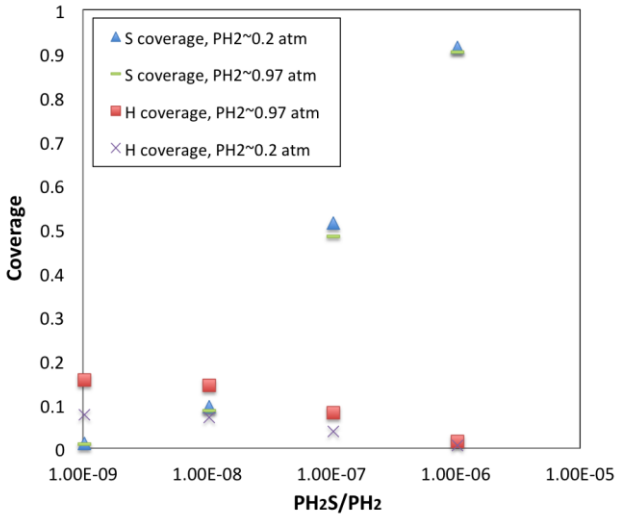

Figure 2-3: Hydrogen and sulfur coverage as a function of P_{H2S}/P_{H2} (coverage-independent kinetic model), [P_{H2S}+ P_{H2}= 0.2 atm and P_{H2S}+ P_{H2}= 0.97 atm; T=700 ºC]

By comparing the H and S coverage values in these two figures, we see that for identical P_{H2S}/P_{H2}, the H coverage is higher at P_{H2}~0.97 atm than at P_{H2}~0.2 atm, whereas the S coverage is lower at P_{H2}~0.97 atm than at P_{H2}~0.2 atm. This shows the dependency of poisoning on both P_{H2S}/P_{H2} and P_{H2} parameters. The key point to take away is that the coverage of electro-active species (H) is significantly affected by both the total pressure and by the typically ascribed parameter, P_{H2S}/P_{H2}.

Effect of sulfur poisoning on the coverage-independent Butler-Volmer equation:

The effect of the sulfur poisoning on the kinetics of H_2 oxidation is studied by comparing the Butler-Volmer expression for the two cases: pure H_2 and H_2S contaminated H_2. The current density from Butler-Volmer expression for pure H_2 electro-oxidation is calculated by equation (2.31) with the exchange current density (i0) and i_{H2}^{*} calculated by the equations (2.41) and (2.42). By considering that the anode activation overpotential, η_a is equal in all cases, the effect of H_2S can be investigated by only comparing the exchange current density. Here, i_{0_H2} and i_{0_H2S} represent the exchange current density for hydrogen electro-oxidation reaction in absence and presence of H_2S, respectively. The reduction in the exchange current density caused by sulfur poisoning can be calculated by the following expression:

$$\frac{i_{0_{H2}}-i_{0_{H2S}}}{i_{0_{H2}}} = 1-\frac{\frac{\left(\frac{PH_2O}{P_0}\right)^{\frac{3}{4}}.PH_2{}^{\frac{1}{4}}K_{H2}{}^{\frac{1}{4}}}{PH_2{}^{\frac{1}{2}}K_{H2}{}^{\frac{1}{2}}+1+\frac{K_6PH_2S}{PH_2}}}{\frac{\left(\frac{PH_2O}{P_0}\right)^{\frac{3}{4}}PH_2{}^{\frac{1}{4}}K_1{}^{\frac{1}{4}}}{PH_2{}^{\frac{1}{2}}K_{H2}{}^{\frac{1}{2}}+1}} = 1-\frac{PH_2{}^{\frac{1}{2}}K_{H2}{}^{\frac{1}{2}}+1}{PH_2{}^{\frac{1}{2}}K_{H2}{}^{\frac{1}{2}}+1+\frac{K_{H2S}PH_2S}{PH_2}} = \left(\frac{\frac{K_{H2S}PH_2S}{PH_2}}{PH_2{}^{\frac{1}{2}}K_{H2}{}^{\frac{1}{2}}+1+\frac{K_{H2S}PH_2S}{PH_2}}\right) \qquad (2.61)$$

The exchange current density effectively decreases with an increase in P_{H2S}/P_{H2} ratio. Figure 2-4 shows the reduction in exchange current density plotted as a function of P_{H2S}/P_{H2}:

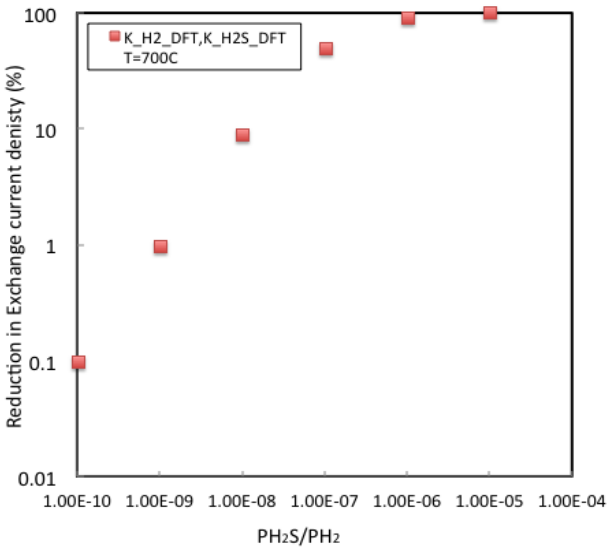

Figure 2-4: Reduction in exchange current density as a function of P_{H2S}/P_{H2} (Coverage-independent kinetic model), [P_{H2}+ P_{H2S}= 0.97 atm; T=700 ºC]

The effect of sulfur poisoning on the exchange current density is not only dependent on P_{H2S}/P_{H2} but also on the partial pressure of the hydrogen and the equilibrium constants of H_2 and H_2S adsorption reactions. Figure 2-5 shows the effect of P_{H2} on the extent of reduction in exchange current density at 0.1 ppm H_2S. The DFT-based calculated K_{H2} and K_{H2S} values are used for calculations. The total pressure is the sum of P_{H2} and P_{H2S}.

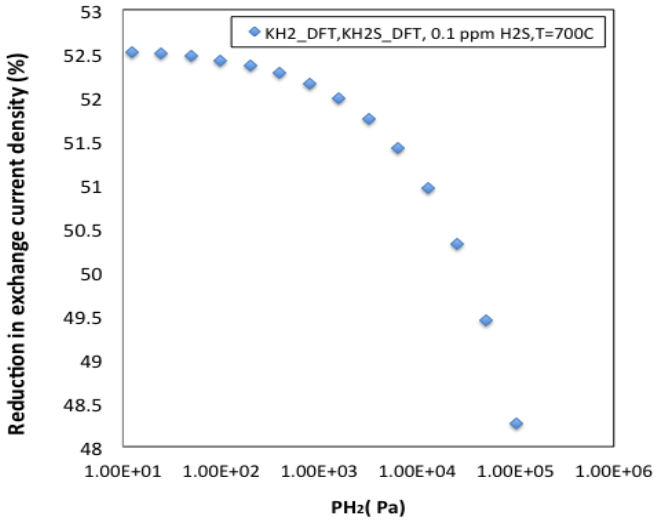

Figure 2-5: Reduction in exchange current density as a function of P_{H2} (coverage-independent kinetic model), [T=700 ºC]

This figure shows that an increase in the hydrogen partial pressure (P_{H2}) decreases the reduction in current density. Figure 2-6 shows the effect of K_{H2S} and K_{H2} on the extent of reduction in exchange current density caused by sulfur poisoning for H_2S concentration of 0.1 ppm. The DFT calculated K_{H2} and K_{H2S} values are used in the calculation of reduction in current density at $P_{H2} + P_{H2S} = 0.97\ atm$. As expected, an increase in K_{H2} results in a decrease in the reduction in current density whereas an increase in K_{H2S} increases the reduction in current density.

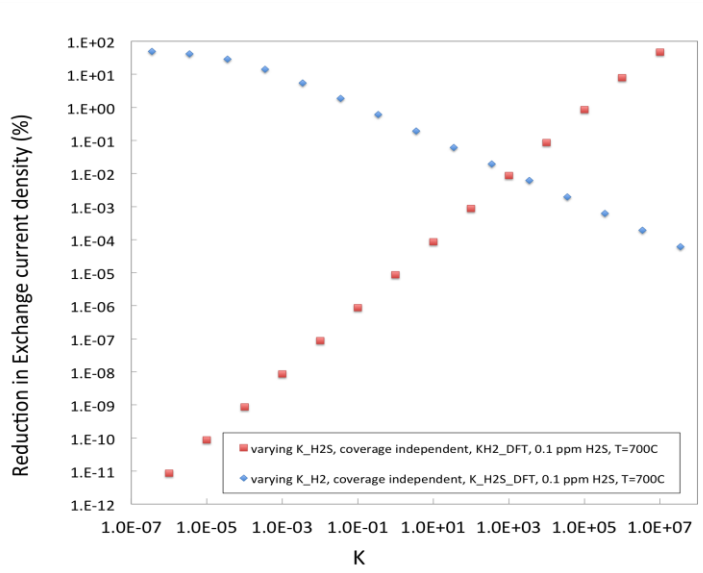

Figure 2-6: Reduction in exchange current density as a function of K_{H2} and K_{H2S} (coverage-independent kinetic model), [P_{H2}+ P_{H2S}= 0.97 atm; T=700 ºC]

As expected, it can be observed from figure 2-6, K_{H2S} and K_{H2} values have a great impact on the extent of the sulfur poisoning effect on the current density. The simplifying assumptions of having a constant and coverage-independent K_{H2S} and K_{H2} values would cause errors in calculating the current density. Therefore, the dependency of K_{H2S} and K_{H2} on the surface coverage should be considered. There have been only a few studies that have considered the coverage-dependent adsorption energies for the chemisorption of H_2S on Ni. However, these models have some deficiencies as discussed in Monder and Karan (2010). For example, in a DFT-based model of Wang and Liu (2007), the competitive adsorption of H_2 on Ni surface is ignored. In addition to that, species activity, thermal corrections and entropy of all surface species are not considered. In another DFT-based model by Galea *et al*, (2007), thermal corrections of the reaction enthalpy is ignored by assuming that the translational and rotational entropy of the gas species is lost on adsorption.

2.2.3 Coverage-dependent thermodynamics of H_2 and H_2S adsorption on Ni

Prior to deriving a coverage-dependent Butler-Volmer type kinetic expression, the thermodynamics of coverage-dependent H_2 and H_2S adsorption on Ni surface will be discussed. In section 2.2.2, in the derivation of the Butler–Volmer type expression with H_2S impurities, a Langmuir-type adsorption was assumed for H_2 and H_2S adsorption reactions in which the adsorption energy is not dependent on the adsorbate coverages. In this section, the dependency of the H_2 and H_2S adsorption reactions on the adsorbate coverages are considered by using a coverage-dependent thermodynamics for H_2S and H_2 adsorption reactions developed by Monder and Karan (2013). The following are presented in this section: a brief presentation of the DFT-derived coverage-dependent energetics; the derivation of the H_2 and H_2S adsorption equilibrium constants; and the calculation of H and S coverages at equilibrium conditions for adsorption of pure H_2 and for adsorption of H_2/H_2S mixture.

Brief presentation of the DFT-derived coverage-dependent energetics:

The dependency of the adsorption energetics on the surface coverage is captured by directly calculating the chemical potential of surface species from the chemical potential of the H and S surface species by the relations (2.62) and (2.63), following the reference of Monder and Karan (2013).

$$\mu_H = E_H(0) + 2\alpha_H \{\theta_H - \theta_H(0)\} + \beta_{HS}\theta_S{}^* + \mathrm{k_B T}\ln\left(\frac{\theta_\mathrm{H}}{(1-\theta_S-\theta_H).\Pi\left\{\frac{\exp\left(-h\frac{\nu_{H,k}}{2k_BT}\right)}{1-\exp\left(-h\frac{\nu_{H,k}}{2k_BT}\right)}\right\}}\right) \tag{2.62}$$

$$\mu_\mathrm{S} = \mathrm{E_S}(0) + 2\alpha_\mathrm{S} \{\theta_\mathrm{S} - \theta_\mathrm{S}(0)\} + \beta_\mathrm{HS}\theta_\mathrm{H}{}^* + \mathrm{k_B T}\ln\left(\frac{\theta_\mathrm{S}}{(1-\theta_S-\theta_H).\Pi\left\{\frac{\exp\left(-h\frac{\nu_{S,k}}{2k_BT}\right)}{1-\exp\left(-h\frac{\nu_{S,k}}{2k_BT}\right)}\right\}}\right) \tag{2.63}$$

The first three terms account for the Electronic energy change. $\mathrm{E_H}(0)$ and $\mathrm{E_S}(0)$ are the zero coverage adsorption energies; $\theta_H(0)$ and $\theta_S(0)$ are the threshold coverages below which there is no dependency on coverage; α_H and α_S are the self-interaction parameters and β_{HS} is the binary interaction parameter. The

last term considers the vibrational energy.

$$q_{i,k}(\text{vib}) = \frac{\exp\left(\frac{-h\nu_{i,k}}{2k_BT}\right)}{(1-\exp(\frac{-h\nu_{i,k}}{k_BT}))} \quad (2.64)$$

$\Pi(q_{i,k}(\text{vib}))$ is the product over the number of vibrational modes for adsorbed species i. $\nu_{i,k}$ is the k^{th} vibrational frequency for species *i*, *h* and k_B are the Planck and Boltzmann constants. Details of the calculation of the chemical potential of the surface species are presented in Appendix B. The reader is also referred to the Monder and Karan (2013) for more details. Chemical potential of the H_2 and H_2S gas species as an ideal gas are calculated from the following relation:

$$\mu_j = \mu_j^0 + RT\ln(P_i) \quad (2.65)$$

μ_j^0 is the standard state chemical potential and P_i is the partial pressure of the gas species. By substituting the chemical potential of gas and surface species in the two equilibrium equations of H_2 and H_2S adsorption reactions, two equations with two unknowns of θ_H and θ_S are obtained and can be solved.

H_2S and H_2 adsorption reaction equilibrium constants

The equilibrium constants for the H_2 and H_2S adsorption reactions are calculated by a series of algebraic manipulations on the chemical equilibrium equations. Starting from K_{H2} formulation defined as $\frac{\theta_H^2}{\theta_{Ni}^2 P_{H_2}}$ and by deriving an expression for P_{H2} obtained from chemical equilibrium equation, one would get an expression for K_{H2} in terms of vibrational, electronic and standards chemical potential of gaseous species.

$$H_2(g) + 2(Ni) \leftrightharpoons 2H(Ni) \quad (2.66)$$

At equilibrium,

$$2\mu_H - \mu_{H2} = 0 \quad (2.67)$$

Here, μ_H is the chemical potential difference of bare Ni and H-covered Ni.

$$2\mu_H - \mu_{H2}^0 = RT\ln(\frac{P_{H2}}{P_0}) \quad (2.68)$$

$$P_{H2} = P_0 \exp\left(\frac{2\mu_H}{RT}\right).\exp(\frac{-\mu_{H2}^0}{RT}) \quad (2.69)$$

By substituting the chemical potential of H with the units of (J/mol) and using the notations of E_H and $\Pi(q_{H,k})$ for the electronic and vibrational energies, we have:

$$\mu_H = F(E_H) + RTlog\{\frac{\theta_H}{(1-\theta_S-\theta_H).\Pi(q_{H,k})}\} \quad (2.70)$$

$$\mathrm{P_{H2}} = P_0 \exp\left(\frac{2FE_H}{RT} + 2log\left\{\frac{\theta_H}{(1-\theta_S-\theta_H).\Pi(q_{H,k})}\right\}\right)\exp(\frac{-\mu^0_{\mathrm{H2}}}{RT}) \quad (2.71)$$

$$\mathrm{P_{H2}} = P_0 \exp\left(\frac{2FE_H}{RT}\right)\left(\frac{\theta_H}{(1-\theta_S-\theta_H).\Pi(q_{H,k})}\right)^2 \exp(\frac{-\mu^0_{\mathrm{H2}}}{RT}) \quad (2.72)$$

By substituting the derived expression for $\mathrm{P_{H2}}$ in equilibrium constant, the desired expression for K_{H2} is derived:

$$K_{H2} = \frac{\Pi(q_{H,k})^2}{P_0} exp\left(-\frac{2FE_H}{RT}\right) exp(\frac{\mu^0_{H2}}{RT}) \quad (2.73)$$

Following the same procedure for K_{H2S} defined as $\frac{P_{H_2}\,\theta_S}{\theta_{Ni}\,P_{H_2S}}$, finding P_{H2}/P_{H2S} as a function of H and S coverages and substituting in the K_{H2S} expression would result in an expression for K_{H2S}.

$$\mu_S + \mu_{H2} - \mu_{H2S} = 0 \quad (2.74)$$

$$0 = \mu_S + \mu^0_{H2} + RTln(\frac{P_{H2}}{P_0}) - \mu^0_{H2S} - RTln\left(\frac{P_{H2S}}{P_0}\right) \quad (2.75)$$

$$-\frac{\mu_S}{RT} - \frac{(\mu^0_{H2}-\mu^0_{H2S})}{RT} = ln\left(\frac{P_{H2}}{P_{H2S}}\right) \quad (2.76)$$

$$\frac{P_{H2}}{P_{H2S}} = exp\left(\frac{-\mu_S}{RT}\right).exp\left(\frac{\mu^0_{H2S}-\mu^0_{H2}}{RT}\right) \quad (2.77)$$

By substituting the chemical potential of S with the units of (J/mol) and using the notations of E_S and $\Pi(q_{S,k})$ for the electronic and vibrational energies, we have:

$$\mu_S = F(E_s) + RTlog\{\frac{\theta_S}{(1-\theta_S-\theta_H).\Pi(q_{S,k})}\} \quad (2.78)$$

$$\frac{P_{H2}}{P_{H2S}} = exp(-\frac{FE_S}{RT})\left(\frac{\theta_S}{(1-\theta_S-\theta_H).\Pi(q_{S,k})}\right)^{-1} exp\left(\frac{\mu^0_{H2S}-\mu^0_{H2}}{RT}\right) \quad (2.79)$$

By substituting the derived expression for $\frac{P_{H2}}{P_{H2S}}$ in K_{H2S}, the desired expression is derived:

$$K_{H2S} = exp(-\frac{FE_S}{RT}).\Pi(q_{S,k}).exp\left(\frac{\mu^0_{H2S}-\mu^0_{H2}}{RT}\right) \quad (2.80)$$

Both derived expressions for the equilibrium constants of H_2 and H_2S adsorptions reactions in coverage-dependent thermodynamics are functions of adsorbed H and S atoms on Ni surface. By calculating the equilibrium constant for H_2 adsorption, it could be realized that in the case for adsorption from a pure H_2 stream, E_H is constant for $\theta_H < \theta_H(0)$. E_H increases with an increase in P_{H2} and hydrogen coverage for $\theta_H > \theta_H(0)$, $(\theta_H(0) = 0.511)$. Therefore, it is expected to have a decrease in the K_{H2} for $\theta_H > \theta_H(0)$ with increase in P_{H2} or θ_H. Another point to mention is that, logically, one would expect the convergence of coverage-dependent DFT-based equilibrium constants and coverage-independent DFT-based equilibrium constants at low H and S coverages. However, it can be predicted that these equilibrium constants do not converge at low coverages. In other words, coverage-dependent DFT-based calculated K_{H2} and coverage-independent DFT-based calculated K_{H2} do not converge at low H coverage or low P_{H2}. Similarly, coverage-dependent DFT-based calculated K_{H2S} and coverage-independent DFT-based calculated K_{H2S} do not converge at low S coverage or low P_{H2S}/P_{H2}. As mentioned earlier in subsection 2.2.2 the reasons for this behavior are not accounting for all the reactions as considered in Monder and Karan (2010), and difference in the surface coverage species on the unit cell C and the H and S coverages,

Calculation of hydrogen and sulfur coverages:

Sulfur and hydrogen coverages can be calculated at equilibrium conditions for H and S adsorption from H_2 and H_2S mixtures. Due to our assumptions of chemical equilibrium condition, the coverage-dependent Gibbs free energy of the adsorption reactions can be set to zero at a constant temperature and pressure. For known pressure, temperature and gas phase composition and by substituting the chemical potential of the gas and surface species in the equilibrium equations, two equations with two unknowns of sulfur and hydrogen coverages are obtained. Solving for the unknowns, the surface coverages of hydrogen and sulfur on the Ni surface are obtained.

Sulfur coverage from adsorption of a mixture of H_2 and H_2S

The calculated θ_S as a function of P_{H2S}/P_{H2} is shown and compared for both coverage-dependent and

coverage-independent kinetic models in figure 2-7. The computed S coverage from coverage-independent model is considerably higher than that from the coverage-dependent model at higher P_{H2S}/P_{H2} values. This behavior can be interpreted by examining the K_{H2S} behavior. As shown in figure 2-8, K_{H2S} of coverage-dependent model decreases with increase in P_{H2S}/P_{H2} and becomes lesser than the K_{H2S} of coverage-independent model at high $P_{H2}S/P_{H2}$ values. That is the reason to observe higher S coverage in coverage-independent model than in the coverage-dependent model at high P_{H2S}/P_{H2} values.

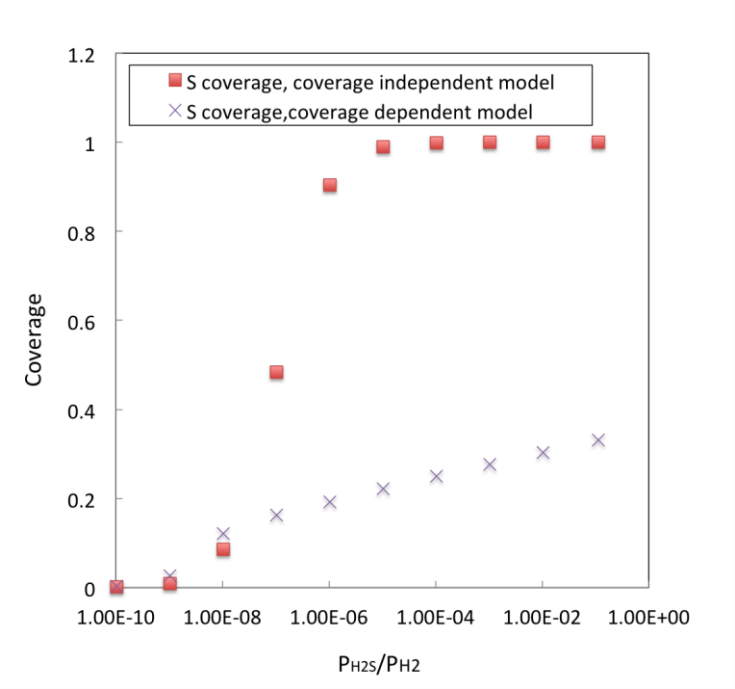

Figure 2-7: Equilibrium sulfur coverage as a function of P_{H2S}/P_{H2} predicted by coverage-independent and coverage-dependent kinetic model [P_{H2}+ P_{H2S}= 0.97 atm; T=700 ºC]

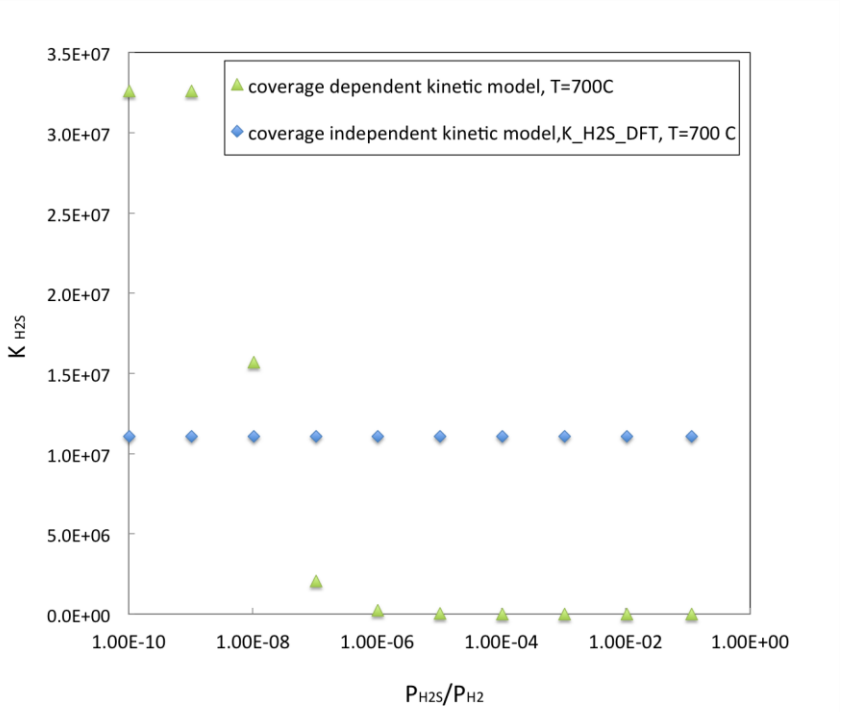

Figure 2-8: H_2S adsorption equilibrium constant as a function of P_{H2S}/P_{H2} [P_{H2}+ P_{H2S}= 0.97 atm; T=700 ºC]

2.2.4 Derivation of the "coverage dependent Butler-Volmer type" kinetic model with sulfur poisoning:

In order to derive a coverage dependent Butler-Volmer (B.V.) kinetic expression, the reaction energetics of the previously derived Butler-Volmer equation must be modified to include dependency on surface coverages. This can be achieved by implementing the coverage-dependent thermodynamics of H_2 and H_2S adsorption in the kinetic expression. The exchange current density of the derived Butler-Volmer type equation in the presence of H_2S was defined by equation (2.41). The coverage dependent kinetic formulation can be achieved by implementing the coverage dependent K_{H2S} and K_{H2} from equations (2.73) and (2.80) into equation (2.41). The expression can also be simplified by expressing the exchange current density in terms of H and S coverage as well:

$$i_0 = i_{H2}^* \left(\frac{\left(\frac{PH_2O}{P_0}\right)^{\frac{3}{4}} \left(\frac{\theta_H}{\theta_{Ni}}\right)^{0.5}}{\frac{1}{\theta_{Ni}}} \right) = i_{H2}^* \left(\frac{PH_2O}{P_0}\right)^{\frac{3}{4}} \theta_H^{0.5} \theta_{Ni}^{0.5} \tag{2.81}$$

At any temperature, pressure and gas phase composition, the equilibrium surface coverages can be calculated and implemented in the coverage-dependent Butler-Volmer expression. In the next section, the effect of the sulfur poisoning on the exchange current density for both coverage-dependent and coverage-independent Butler-Volmer type kinetic models is examined.

2.2.5 Effect of H_2S on the kinetics of H_2 oxidation

In this section, the effect of H_2S poisoning of Nickel computed from both coverage-independent and coverage-dependent Butler-Volmer equations are studied by comparing the corresponding exchange current density. Six different kinetic models are presented as demonstrated in Figure 2-1.

- The kinetic model with only H_2 adsorption (without H_2S) is presented for three cases with the following H_2 adsorption equilibrium constants: $K_{H2\_Zhu\ et\ al}$ from Zhu *et al.* (2005) approach; K_{H2_DFT} from coverage-independent DFT calculated energetics (Monder and Karan, 2010), and K_{H2_DFT} from coverage-dependent DFT calculated energetics (Monder and Karan, 2013). The DFT results are for hydrogen adsorption on Ni (111) surface.
- The kinetic model with both H_2 and H_2S adsorption reactions are presented for the three cases with the following sets of adsorption equilibrium constants: $K_{H2\_Zhu\ et\ al}$ and K_{H2S_DFT}; K_{H2_DFT} and K_{H2S_DFT} from coverage-independent DFT calculated energetics, and K_{H2_DFT} and K_{H2S_DFT} from coverage-dependent DFT calculated energetics. The parameters used in the Butler-Volmer equations are listed in Table 2-1 below.

Table 2-1: Kinetic models parameters

Parameters	Values
Pressure	101325 Pa
H_2 mole fraction	0.97- n_H_2S
H_2O mole fraction	0.03
H_2S mole fraction (n_H_2S)	1×10^{-10} to 1×10^{-1}
$i^*_{ref,H2}$	$4.8\times10^{9}\ \frac{A}{m3}$
i^*_{H2}	$1.205\times10^{9}\ \frac{A}{m3}$
K_{H2_DFT}	$3.48\times10^{-7}\ \frac{1}{Pa}$
$K_{H2\ \_Zhu\ et\ al}$	$1.409\times10^{-5}\ \frac{1}{Pa}$
K_{H2S_DFT}	$1.1\times10^{+7}$
T	700 ºC
T_{ref}	800 ºC

Figure 2-9 shows the changes of i_0 in aforementioned 6 models at different P_{H2S}/P_{H2}. Concerning the models without H_2S, following behaviors can be observed: The exchange current density remains constant. Exchange current density (i_0) of the coverage-independent model with $K_{H2\_Zhu\ et\ al}$ is higher than the i_0 of the coverage independent model with K_{H2_DFT} due to higher value of $K_{H2\_Zhu\ et\ al}$ than K_{H2_DFT}. The i_0 of the coverage-dependent model is slightly higher than the coverage-independent model with K_{H2_DFT} due to its higher equilibrium constant as it is shown in figure 2-10 that coverage-dependent K_{H2} is higher than the coverage-independent K_{H2_DFT} at low P_{H2S}/P_{H2} of 1×10^{-10}. Concerning the models with H_2S

poisoning, the i_0 decreases with an increase in P_{H2S}/P_{H2}. Exchange current density of the coverage-independent models with K_{H2_DFT} and $K_{H2\_Zhu\ et\ al}$ at low $P_{H2}S/P_{H2}$ matches the i_0 of the coverage independent models without H_2S with K_{H2_DFT} and $K_{H2\_Zhu\ et\ al}$ respectively. Reduction in i0, at high P_{H2S}/P_{H2} is less abrupt in coverage-dependent model than in coverage-independent with K_{H2_DFT}, that is due to lower K_{H2S} values of coverage-dependent model than coverage-independent model (K_{H2_DFT}) at high P_{H2S}/P_{H2} (referring to figure 2-8).

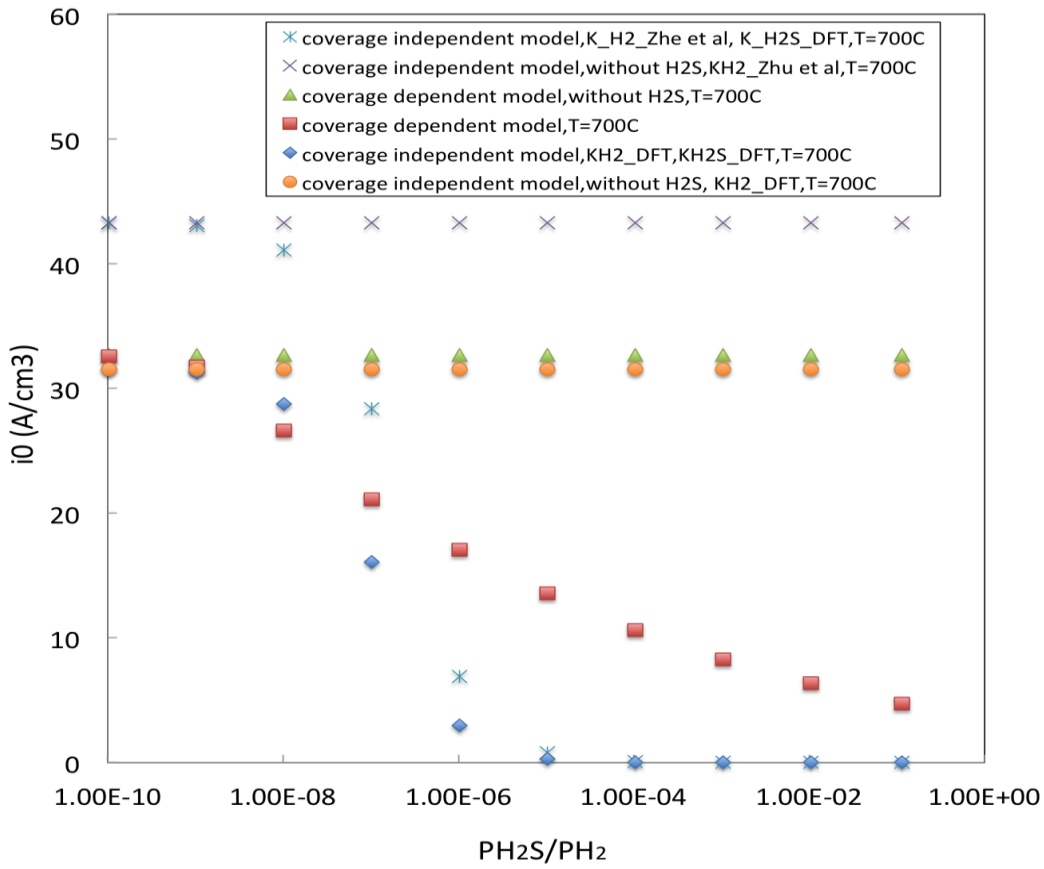

Figure 2-9: Exchange current density as a function of P_{H2S}/P_{H2} for conditions in Table 2.1

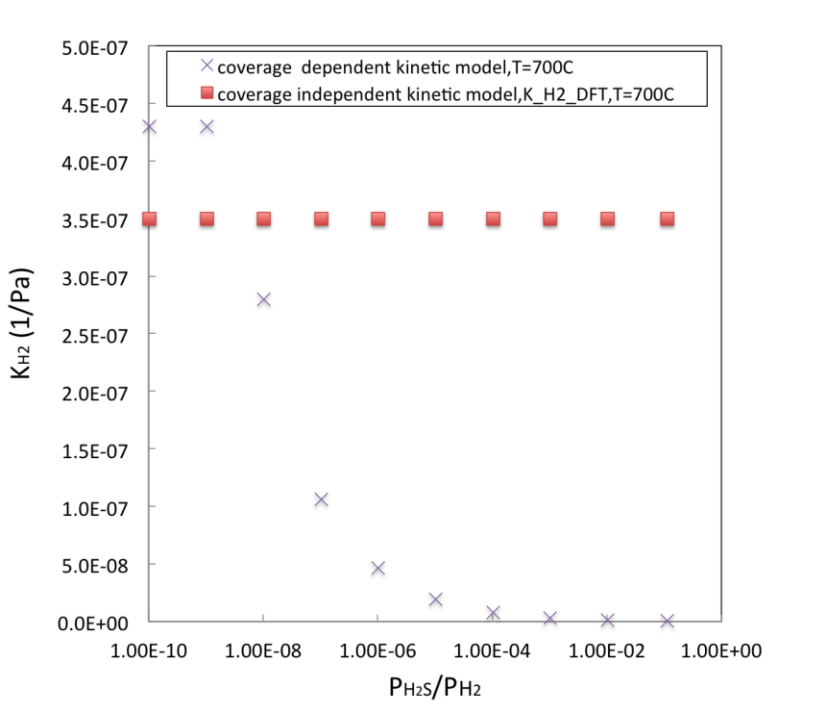

Figure 2-10: **Hydrogen adsorption equilibrium constant as a function of P_{H2S}/P_{H2}**

Predicted reduction in exchange current density by coverage-dependent and independent models:

In this section, the reduction in HOR exchange current density due to sulfur adsorption from H_2S is compared for the two different kinetic models, i.e. coverage-dependent and coverage-independent kinetic models. Figure 2-11 shows the relative reduction in exchange current density due to sulfur poisoning for coverage dependent and independent kinetic models.

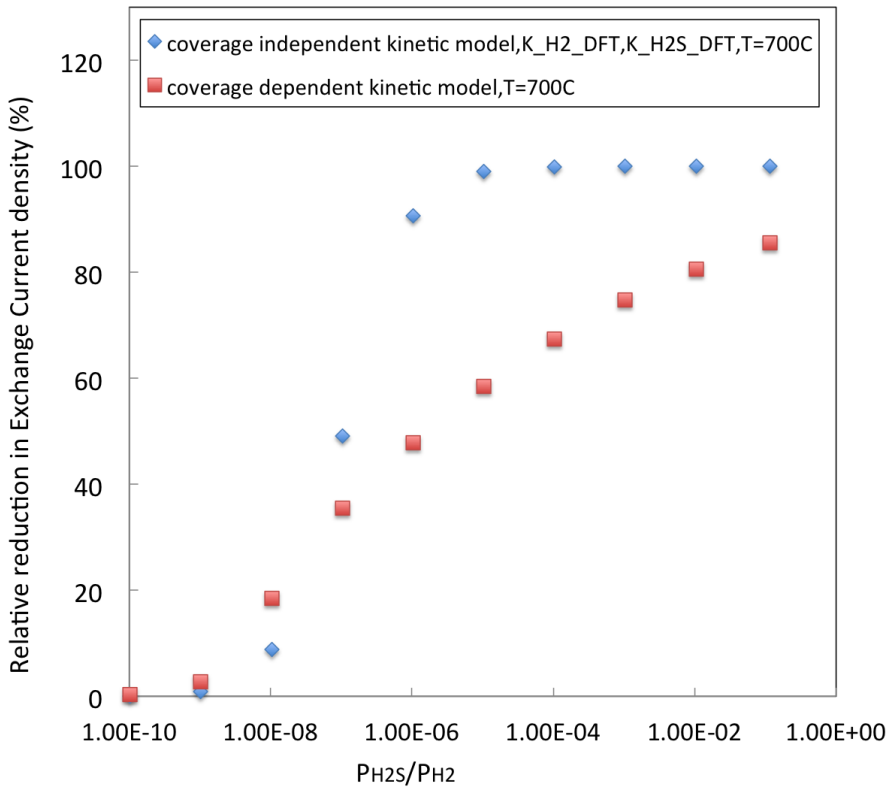

Figure 2-11: Reduction in exchange current density for coverage-dependent and coverage-independent kinetic models [T=700°C]

For coverage-independent model, the reduction in exchange current density predicted by the coverage-independent model changes abruptly from about 10% to more than 90% over a small range of P_{H2S}/P_{H2} approximately from 1×10^{-8} to 1×10^{-6}. The model predicts a reduction in exchange current density of almost 100 % for P_{H2S}/P_{H2} greater than 1×10^{-5}. Reduction in exchange current predicted by coverage-independent model is different than the coverage-dependent model in terms of the total reduction over the P_{H2S}/P_{H2} range and the slope of the curve. Reduction in exchange current density predicted by coverage-dependent model increase steadily from about 10% to more than 80% over a broad range of P_{H2S}/P_{H2} approximately from 1×10^{-8} to1×10^{-1}. Predicted reduction in exchange current density in coverage-dependent model is lower than the coverage-independent model at higher P_{H2S}/P_{H2}.

2.3 Conclusion

A new kinetic model in the form of modified Butler-Volmer expression was developed that captures the effect of the presence of H_2S impurities and sulfur poisoning on the H_2 electrochemical reaction in the Ni-based anodes of SOFCs. The K_{H2} and K_{H2S} being the equilibrium constants of the H_2 and H_2S adsorption reactions, appear in the kinetic formulation. The kinetic model can be divided into two groups: coverage dependent and coverage independent models based on the dependency of the K_{H2} and K_{H2S} on the S and H coverages on Ni surface. In the coverage-independent kinetic model, K_{H2} and K_{H2S} are constant values that do not change by the change of S and H coverages. In the coverage dependent kinetic model K_{H2} and K_{H2S} are functions of the S and H coverages. For both models, an increase in H_2S concentration results in a greater reduction in the exchange current density. The relative reduction in exchange current density predicted by coverage independent model is more dramatic than the predicted reduction by coverage dependent model. Much of the reduction in the exchange current density predicted by coverage independent model occurs from H_2S concentration of 0.01 ppm to 1 ppm and it almost remains constant for H_2S concentration higher than 1 ppm. The relative reduction in the exchange current density predicted by coverage dependent model increases gradually with an increase in the H_2S concentration. The predicted reduction in this model is almost 50 % for 1ppm H_2S concentration.

Chapter 3

Multiphysics electrochemical performance model of anode half-cell SOFC with the sulfur poisoning effect

This Chapter presents the development of a *multiphysics electrochemical performance* model for anode half-cell in the presence of H_2S. The model is called multiphysics electrochemical performance as it predicts the effect of the H_2S poisoning on the electrochemical performance of the cell by considering the involved key physical phenomena. The model considers a two-dimensional (2D) geometry consisting of a fuel gas channel, a porous anode and an electrolyte. The model couples all the key transport phenomena including momentum, mass and charge transport with the electrode kinetics, derived in Chapter two. The *multiphysics electrochemical performance* model is categorized based on the type of the Butler-Volmer kinetic expression used as kinetic model.

3.1 Introduction

In development of the *multiphysics electrochemical performance model***,** the kinetic model for the hydrogen electrochemistry considering the effect of sulfur poisoning, derived in previous chapter, is implemented into the 2-dimensional porous anode model. The 2-dimensional porous anode model considers the multi-component transport of gases in the porous anode and in the fuel channel, the ionic and electronic species transport in the porous anode, and the ionic species transport in the electrolyte layer. In addition to predicting the effect of H_2S on the electrochemical performance (current-voltage curves), the distributions of species concentration, pressure and electrical potential are examined. The effects of different kinetic formulations, discussed in Chapter 2, on anode performance are explored. It may be recalled that the kinetic models differ in the manner in which the H_2 and H_2S adsorption reactions are treated, i.e. whether the equilibrium constants (K_{H2} and K_{H2S}) are considered to be coverage-

independent or coverage-dependent. The multiphysics electrochemical performance models are divided and named based on the type of kinetic model (derived in Chapter 2) being implemented in model. Figure 3-1 summarizes the multiphysics electrochemical performance models presented in Chapter 3

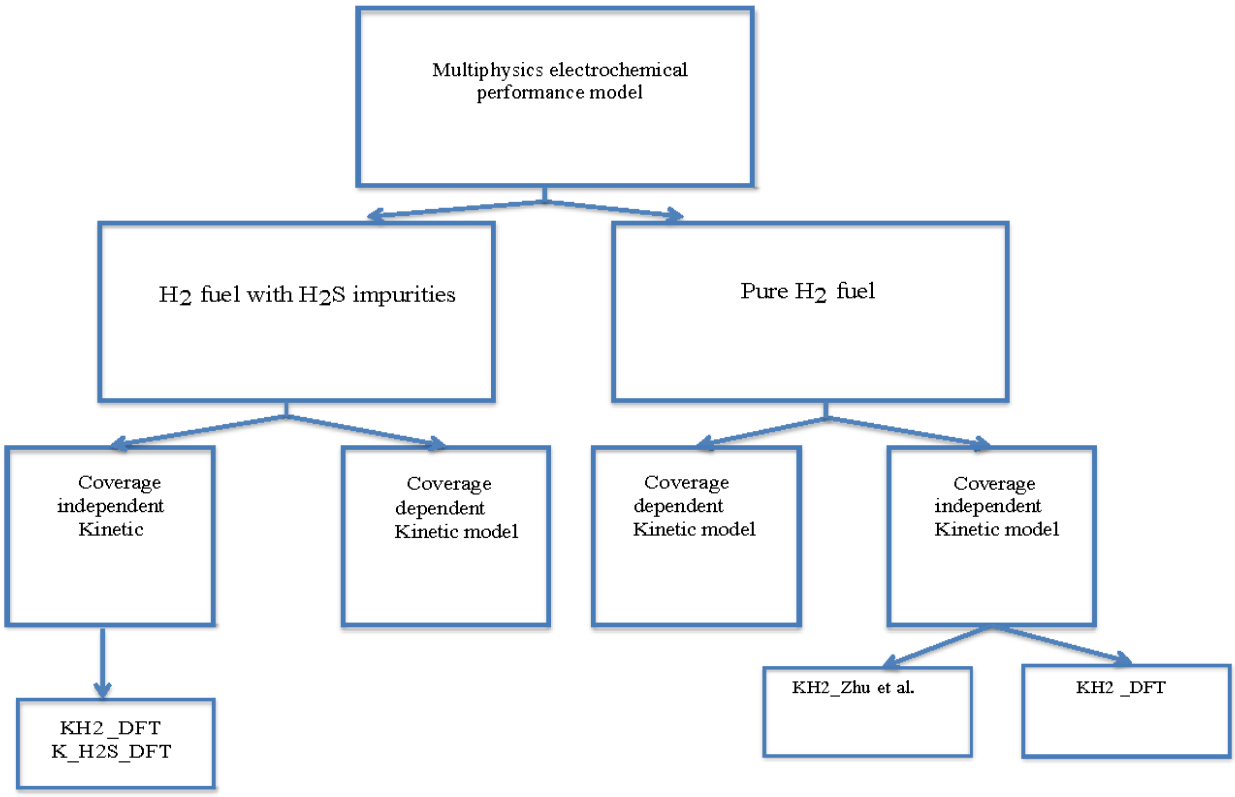

Figure 3-1: Multiphysics electrochemical performance models reported in this thesis

In the following sections, the model geometry, the computational domains and the transport phenomena equations considered in each model domain are explained. The main features of the model, the electrochemical performance of each model and the relative loss in the performance due to the sulfur poisoning will be shown. The results will also be compared to the experimental data.

3.1.1 Anode Electrochemistry

Anode electrochemistry formulations consist of general Butler-Volmer type expression used for the hydrogen electro-oxidation in addition to the derived formulations in Chapter 2 that captures the effect of the sulfur poisoning. General form of the Butler–Volmer equation is expressed by following equations:

$$i = i_0[exp\left(\frac{\alpha_a F\eta_a}{RT}\right) - exp\left(\frac{\alpha_c F\eta_a}{RT}\right)] \tag{3.1}$$

$$i_0 = i^*_{H2}\left(\frac{\left(\frac{P_{H2O}}{P_0}\right)^{\frac{3}{4}} {P_{H_2}}^{1/4} {K_1}^{1/4}}{{P_{H_2}}^{1/2}{K_1}^{1/2}+1+\frac{K_6 P_{H_2S}}{P_{H_2}}}\right) \tag{3.2}$$

Exchange current density is calculated by equation (3.2) in the absence of sulfur poisoning effect and is calculated by equation (2.41) or (2.81) in the presence of H_2S in the fuel mixture to capture the sulfur poisoning effect. η_a is the local activation overpotential and is defined as :

$$\eta_a = \emptyset_{\text{el}} - \emptyset_{\text{ion}} - E_a^{eq} \tag{3.3}$$

$\emptyset_{\text{el}}$ and $\emptyset_{\text{ion}}$ represent the electronic and ionic phase potentials. E_a^{eq} is the local equilibrium phase potential difference and is calculated as follows:

$$E_a^{eq} = \frac{\Delta G^0}{2.F} + \frac{RT}{2.F} ln \frac{P_{H2O}}{P_{H2}} \tag{3.4}$$

$$\Delta G^0 = \mu^0_{H2O} - \mu^0_{H2} \tag{3.5}$$

μ^0_{H2O} and μ^0_{H2} are the standard chemical potentials of the H_2O and H_2 species.

3.2 Model domains

The geometry that is considered for our two-dimensional model consists of a fuel channel, a porous anode with Ni-YSZ composite matrix, a YSZ electrolyte and an ideal cathode boundary as it is shown in figure 3-2 below. An ideal cathode boundary at the cathode electrolyte interface implies that ohmic and activation losses are zero for the cathode. The fuel channel is 1.5 cm long with 1 mm height. The thickness of the Ni-YSZ anode and electrolyte layers are 550 μm and 20 μm respectively with 1 cm length. Figure 3-2 shows the model geometry.

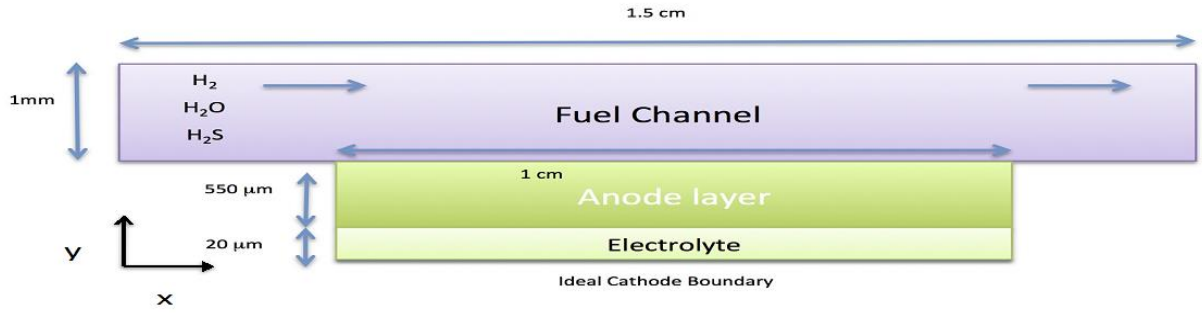

Figure 3-2: Schematic diagram of the half-cell geometry

A reactant mixture consisting of hydrogen and water vapor enters the fuel channel from the left side in the figure 3-2. For cases where H_2S is considered in the model, the feed mixture will also contain H_2S in addition to H_2 and H_2O. The hydrogen in the fuel mixture in the gas channel is transported through the pores of anode domain. During the transport in the porous anode, these species interact with the Ni and YSZ surfaces. Oxygen ions being transported through the electrolyte (YSZ) react with adsorbed hydrogen at the TPB. Water and electrons are the products of the electrochemical reaction and are transported through the pores of the porous anode to the gas channel and through the Ni phase to the external circuit, respectively as shown in figure 1-2. The fully coupled multi-physics model considers the transport of mass, momentum and charged species in the following domains:

- Multicomponent gas species transport in the gas channel.

- Multicomponent gas species transport in the porous anode.

-Momentum transport in the gas channels.

-Momentum transport in the porous anode.

-Charge transport (electrons and oxygen ions) in the porous composite anode.

-Charge transport (oxygen ions) in the electrolyte.

These transport phenomena expressed in terms of PDE (partial differential equations) in each domain with necessary boundary conditions for each PDE will be discussed later. Microstructural effects of anode porous layer are accounted for through effective properties. In calculating the effective properties, the

average size and volume fractions of each phase in addition to the percolation effects are considered. The electrochemical reaction of hydrogen is captured by Butler-Volmer type kinetic expression in the anode domain. In the presence of the H_2S in the H_2 feed, sulfur is also adsorbed on the Ni surface. The competitive adsorption of the H_2S and H_2 that is captured in our kinetic formulations is dependent on the partial pressure of H_2 and H_2S and the energetics of the reaction. In the coverage-dependent kinetic model in which the energetics of H_2 and H_2S adsorption reactions are dependent on coverage, the distributed sulfur and hydrogen surface coverage in the anode domain is calculated by adding a module to solve the chemical equilibrium of H_2 and H_2S adsorption reactions. This module that is called the "Coverage module" is solved simultaneously with the PDEs of the transport model. The next section will address the anode electrochemistry models implemented in the 2D porous anode model.

3.3 Transport model

3.3.1 Mass transport for multicomponent gas species mixture:

The general form of mass conservation can be expressed as:

$$\frac{\partial}{\partial t}(\rho_i) = -\nabla.[\mathbf{j_i} + w_i\rho\mathbf{v}] + r_i \tag{3.6}$$

ρ_i , j_i, w_i, v, ρ represent the density of species i, diffusive flux of species i due to the concentration gradient, mass fraction of species i, mass average velocity and density of the gas mixture, respectively. $w_i\rho u$ is the convective flux for species i and r_i is the rate of production or consumption of species i. The steady state mass transport in the electrode and in the gas channel can be described by the convective-diffusion mass transport equation:

$$\nabla.[\mathbf{j_i} + w_i\rho\mathbf{v}] = r_i \tag{3.7}$$

In the multicomponent species transport, the Maxwell-Stefan equation is used for diffusive flux formulation. Based on this formulation, diffusive flux is proportional to the diffusional driving force and is expressed by:

$$\mathbf{j_i} = -\rho w_i \sum_{\substack{j=1 \\ i \neq j}}^{n} \widetilde{D}_{ij} \mathbf{d_j} \tag{3.8}$$

$\widetilde{D}_{ij}$ is the multicomponent Fick diffusivity of species *i* in *j*. d_j is the diffusional driving force.

$$d_j = \nabla x_j + \left(x_j - w_j\right) \frac{\nabla \mathrm{p}}{p} \tag{3.9}$$

x_j is the mole fraction of species j. By substituting the diffusive flux in the convective-diffusion mass transport equation, the final equation for multicomponent species transport is obtained:

$$\nabla . [\, -\rho w_i \sum_{\substack{j=1 \\ i \neq j}}^{n} \widetilde{D}_{ij} (\nabla x_j + \left(x_j - w_j\right) \frac{\nabla \mathrm{p}}{p}) + (w_i \rho \mathrm{v})] = \mathrm{r_i} \tag{3.10}$$

The multicomponent Fick diffusivity ($\widetilde{D}_{ij}$) is related to the binary diffusion coefficients ($\mathrm{D_{ij}}$) by:

$$\widetilde{D}_{ii} = \frac{-w_j^2}{x_i x_j} \mathrm{D_{ij}} \tag{3.11}$$

$$\widetilde{D}_{jj} = \frac{-w_i^2}{x_i x_j} \mathrm{D_{ij}} \tag{3.12}$$

$$\widetilde{D}_{ij} = \widetilde{D}_{ji} = \frac{-w_i w_j}{x_i x_j} \mathrm{D_{ij}} \tag{3.13}$$

Mass transport of multicomponent gas mixture in gas channel:

In the gas channel, there is no reaction and r_i is zero, therefore, the mass transport equation in the gas channel reduces to the following:

$$\nabla . [\, -\rho w_i \sum_{\substack{j=1 \\ i \neq j}}^{n} \widetilde{D}_{ij} (\nabla x_j + \left(x_j - w_j\right) \frac{\nabla \mathrm{p}}{p}) + (w_i \rho \mathrm{v})] = 0 \tag{3.14}$$

Mass transport of multicomponent gas mixture in porous anode:

The mass transport equation in the porous anode is:

$$\nabla . [\, -\rho w_i \sum_{\substack{j=1 \\ i \neq j}}^{n} \widetilde{D}^{eff}{}_{ij} (\nabla x_j + \left(x_j - w_j\right) \frac{\nabla \mathrm{p}}{p}) + (w_i \rho \mathrm{v})] = \mathrm{r_i} \tag{3.15}$$

Effective binary diffusion coefficient $\left(\widetilde{D}^{eff}{}_{ij}\right)$ takes into account the effect of porosity (ϵ) and the tortuosity (τ) of the porous media.

$$\mathrm{D}_{ij}^{eff} = \frac{\epsilon}{\tau} D_{ij} \tag{3.16}$$

Reaction rate (r_i) for the H_2 being produced is calculated by:

$$r_i = \frac{i_V M_{H2}}{2F} \tag{3.17}$$

With F being the Faradays constant, i_V being the volumetric current density (A/m^3), and M_{H2} being the molecular weight of the hydrogen.

3.3.2 Momentum transport

Navier-Stokes equation coupled to the continuity equation is used to model the flow in the channel. Temperature and composition-dependent viscosity and density are used for momentum transport modeling in the fuel channel.

$$\rho(\mathbf{v}.\nabla\mathbf{v}) - \nabla.\left[\mu(\nabla\mathbf{v} + (\nabla\mathbf{v})^T) - \left(\frac{2}{3}\mu\right)(\nabla.\mathbf{v})\mathbf{I}\right] - \nabla P = \frac{\partial}{\partial t}(\rho\mathbf{v}) \tag{3.18}$$

μ , ρ, v and P are the viscosity, density, velocity vector and the pressure of the gas mixture. **I** is the identity matrix. This generalized equation can be adopted for both gas channel and the porous media.

Momentum transport in the gas channel

Momentum conservation equation in the gas channel, without reaction and at steady state is solved with continuity equation in this domain:

$$\rho(\mathbf{v}.\nabla\mathbf{v}) - \nabla.\left[\mu(\nabla\mathbf{v} + (\nabla\mathbf{v})^T) - \left(\frac{2}{3}\mu\right)(\nabla.\mathbf{v})\mathbf{I}\right] - \nabla P = 0 \tag{3.19}$$

$$\nabla.(\rho\mathbf{v}) = 0 \tag{3.20}$$

Momentum transport in the porous media

The Navier-Stokes equation can be further modified to include the Darcy's term and is solved with the continuity equation in this domain.

$$\left(\frac{\mu}{\kappa} + R_a\right)\mathbf{v} = \nabla.\left[-P\mathbf{I} + \frac{\mu}{\epsilon}(\nabla\mathbf{v} + (\nabla\mathbf{v})^T) - \frac{2}{3}\mu(\nabla.\mathbf{v})\mathbf{I}\right] \tag{3.21}$$

$$\nabla.(\rho\mathbf{v}) = R_a \tag{3.22}$$

ϵ is the porosity or void fraction of the electrode. κ is the permeability of the gas . R_a is the net rate of mass production in anode.

$$R_a = \frac{i_V(M_{H2O} - M_{H2})}{2F} \tag{3.23}$$

3.3.3 Electronic and ionic charge transport

Electric and ionic potential fields are related to the rate of production of the charged species as the result of electrochemical reaction. The Ohm's law is used to express the ionic and electronic potential fields in anode and electrolyte domains. The electronic charge transport in anode, ionic charge transport in the electrolyte and anode domains are expressed by the following equations respectively:

$$\nabla.(-\sigma_{el}^{eff}\nabla\emptyset_{\mathrm{el}}) = i_V \tag{3.24}$$

$$\nabla.(-\sigma_{ion}\ \nabla\emptyset_{\mathrm{ion}}) = 0 \tag{3.25}$$

$$\nabla.(-\sigma_{ion\_an}^{eff}\nabla\emptyset_{\mathrm{ion\_an}}) = -i_V \tag{3.26}$$

σ_{el}^{eff}, σ_{ion} and $\sigma_{ion\_an}^{eff}$ are the effective electronic conductivity of anode, ionic conductivity of electrolyte and effective ionic conductivity of anode respectively. $\nabla\emptyset_{\mathrm{el}}$, $\nabla\emptyset_{\mathrm{ion}}$ and $\nabla\emptyset_{\mathrm{ion\_an}}$ are the electric phase potential for anode, ionic phase potential for electrolyte and anode respectively. i_V is the volumetric current density calculated by Butler-Volmer equation as in equation (3.1).

3.3.4 Governing equations and Boundary conditions

In this section the governing equations and the boundary conditions of each domain are presented.

-Mass transport of multicomponent gas mixture in gas channel:

$$\nabla.[-\rho w_i \sum_{\substack{j=1 \\ i\neq j}}^{n} \widetilde{D}_{ij}(\nabla x_j + (x_j - w_j)\frac{\nabla \mathrm{p}}{p}) + (w_i \rho \mathrm{v})] = 0 \tag{3.27}$$

Boundary conditions:

Mass fraction of the inlet chemical species that are H_2, H_2O and H_2S is defined in the fuel inlet channel.

$$\mathrm{w}_{\mathrm{H2}|\partial\Omega_{\mathrm{fuel,inlet}}} = \mathrm{w}_{\mathrm{H2,in}} \tag{3.28}$$

$$\mathrm{w}_{\mathrm{H2O}|\partial\Omega_{\mathrm{fuel,inlet}}} = \mathrm{w}_{\mathrm{H2O,in}} \tag{3.29}$$

$$\mathrm{w}_{\mathrm{H2S}|\partial\Omega_{\mathrm{fuel,inlet}}} = \mathrm{w}_{\mathrm{H2S,in}} \tag{3.30}$$

Continuity of the fluxes is set at the anode/electrolyte interface.

$$\mathbf{J_i}_{|\partial\Omega_{\mathrm{channel/anode}}} = \mathbf{J_i}_{|\partial\Omega_{\mathrm{anode|channel}}} \tag{3.31}$$

$\mathbf{J_i}$ is the total flux.

Convective flux boundary is set at the fuel outlet channel.

$$\mathbf{n}.\mathbf{J_{i|}}_{\partial\Omega_{\text{fuel,outlet}}} = \mathbf{n}.w_i\rho\mathbf{v} \tag{3.32}$$

No flux condition is set at the walls of fuel gas channel.

$$\mathbf{n}.\mathbf{J_{i|}}_{\partial\Omega_{\text{wall}}} = 0 \tag{3.33}$$

-Mass transport of multicomponent gas mixture in porous anode:

$$\nabla.\left[-\rho w_i \sum_{\substack{j=1 \\ i\neq j}}^{n} \widetilde{D}_{ij}\left(\nabla x_j + \left(x_j - w_j\right)\frac{\nabla \mathrm{p}}{p}\right) + (w_i\rho \mathrm{v})\right] = r_i \tag{3.34}$$

Boundary conditions:

No flux condition is set at the walls of the anode.

$$\mathbf{n}.\mathbf{J_{i|}}_{\partial\Omega_{\text{wall}}} = 0 \tag{3.35}$$

Continuity of the fluxes in set at the anode/electrolyte interface.

$$\mathbf{J_{i|}}_{\partial\Omega_{\text{channel/anode}}} = \mathbf{J_{i|}}_{\partial\Omega_{\text{anode|channel}}} \tag{3.36}$$

Momentum transport in gas channel:

$$\rho(\mathbf{v}.\nabla\mathbf{v}) - \nabla.\left[\mu(\nabla\mathbf{v} + (\nabla\mathbf{v})^T) - \left(\frac{2}{3}\mu\right)(\nabla.\mathbf{v})\mathbf{I}\right] - \nabla \mathrm{P} = 0 \tag{3.37}$$

$$\nabla.(\rho\mathbf{v}) = 0 \tag{3.38}$$

Boundary conditions

Fully developed, Laminar flow is set at the fuel inlet.

Atmospheric pressure normal to the outlet of the fuel channel is set at the outlet of the fuel channel.

$$p_{channel|}{}_{\partial\Omega_{\text{wall}}} = P_{atm} \tag{3.39}$$

Continuity boundary condition is set at the channel/porous anode interface.

$$p_{channel|}{}_{\partial\Omega_{\text{channel/electrolyte}}} = p_{electrode|}{}_{\partial\Omega_{\text{channel/electrolyte}}} \tag{3.40}$$

$$\mathbf{v}_{channel|}{}_{\partial\Omega_{\text{channel/electrolyte}}} = \mathbf{v}_{electrode|}{}_{\partial\Omega_{\text{channel/electrolyte}}} \tag{3.41}$$

No slip boundary at the walls of the channel.

$$\mathbf{v}|_{\partial\Omega_{\text{wall}}} = 0 \tag{3.42}$$

Momentum transport in porous anode:

$$\left(\frac{\mu}{\kappa} + R_a\right)\mathbf{v} = \nabla.\left[-\mathrm{P}\mathbf{I} + \frac{\mu}{\epsilon}(\nabla\mathbf{v} + (\nabla\mathbf{v})^T) - \frac{2}{3}\mu(\nabla.\mathbf{v})\boldsymbol{I}\right] \tag{3.43}$$

$$\nabla.(\rho\mathbf{v}) = \mathrm{R_a} \tag{3.44}$$

Boundary conditions

Continuity boundary condition is set at the channel/porous anode interface.

$$\mathbf{v}_{electrode|\partial\Omega_{\text{channel/electrolyte}}} = \mathbf{v}_{channel|\partial\Omega_{\text{channel/electrolyte}}} \tag{3.45}$$

$$p_{electrode|\partial\Omega_{\text{channel/electrolyte}}} = p_{channel|\partial\Omega_{\text{channel/electrolyte}}} \tag{3.46}$$

No slip boundary at the walls of porous anode.

$$\mathbf{v}|_{\partial\Omega_{\text{wall}}} = 0 \tag{3.47}$$

Ion and electron transport in porous anode and electrolyte:

Ion transport in electrolyte:

$$\nabla.(-\sigma_{ion}\ \nabla\emptyset_{\text{ion}}) = 0 \tag{3.48}$$

Boundary condition :

Zero ionic flux ($\mathrm{i_i}$) is implemented at the walls of electrolyte:

$$\mathbf{n}.\mathbf{i_i}|_{\partial\Omega_{\text{wall}}} = 0 \tag{3.49}$$

An ideal cathode boundary condition at the electrolyte/cathode interface which neglects all the losses of the cathode.

$$\mathrm{E_c} = \emptyset_{\text{el(c)}} - \emptyset_{\text{ion(c)}} = \mathrm{E_c}^{eq} \tag{3.50}$$

$$\emptyset_{ion(c)}|_{\partial\Omega_{cathode/electrolyte}} = \emptyset_{\text{el(c)}} - \mathrm{E_c}^{eq} \tag{3.51}$$

$\mathrm{E_c}$, $\mathrm{E_c}^{eq}$, $\emptyset_{ion(c)}$ and $\emptyset_{\text{el(c)}}$ are the potential of the cathode (difference between the potential of electronic phase and potential of ionic phase in cathode), equilibrium potential of cathode(equilibrium potential difference between the electronic phase and the ionic phase), and ionic potential of the cathode and electrical potential of cathode at the cathode/channel interface.

Continuity of ionic flux is set at the electrolyte/porous anode interface.

$$\mathbf{i}_{\mathbf{i}|\partial\Omega_{\text{electrolyte/anode}}} = \mathbf{i}_{\mathbf{i}|\partial\Omega_{\text{anode|electrolyte}}} \tag{3.52}$$

Ion transport in porous anode:

$$\nabla.\left(-\sigma_{ion\_an}^{eff}\nabla\emptyset_{\text{ion\_an}}\right) = -i_V \tag{3.53}$$

Boundary condition :

Zero ionic flux ($\mathbf{i_i}$) is implemented at the walls of the electrode and at the electrode/channel interface.

$$\mathbf{n}.\,\mathbf{i_i}|_{\partial\Omega_{\text{wall}}} = 0 \tag{3.54}$$

$$\mathbf{n}.\,\mathbf{i_i}|_{\partial\Omega_{\text{anode/channel}}} = 0 \tag{3.55}$$

Continuity of ionic flux is set at the porous anode/electrolyte interface.

$$\nabla.\left(-\sigma_{el}^{eff}\nabla\emptyset_{\text{el}}\right) = i_V \tag{3.56}$$

$$\mathbf{i}_{\mathbf{i}|\partial\Omega_{\text{electrolyte/anode}}} = \mathbf{i}_{\mathbf{i}|\partial\Omega_{\text{anode|electrolyte}}} \tag{3.57}$$

Electron transport in porous anode:

An anode reference potential is set at the gas channel/porous anode interface.

$$\phi_{el(a)}|_{\partial\Omega_{\text{anode/channel}}} = 0 \tag{3.58}$$

Electrical insulation i.e. zero electronic flux ($\mathbf{i_e}$) is implemented at the walls of the anode and at the anode/electrolyte interface.

$$\mathbf{n}.\,\mathbf{i_e}|_{\partial\Omega_{\text{wall}}} = 0 \tag{3.59}$$

$$\mathbf{n}.\,\mathbf{i_e}|_{\partial\Omega_{anode/electrolyte}} = 0 \tag{3.60}$$

Summary of key governing equations and the boundary conditions are summarized in table 3-1.

Table 3-1: Governing equations and the boundary conditions of the transport model

	Gas channel	Anode	Electrolyte
Multicomponent species transport	Governing equation: $\nabla.[-\rho w_i \sum_{\substack{j=1 \\ i\neq j}}^{n} \widetilde{D}_{ij}(\nabla x_j + (x_j - w_j)\frac{\nabla \mathrm{p}}{p}) + (w_i \rho \mathrm{v})] = 0$ Boundary conditions: $\mathrm{w}_{\mathrm{H2O}\mid\partial\Omega_{\mathrm{fuel,inlet}}} = \mathrm{w}_{\mathrm{H2O,in}}$ $\mathrm{w}_{\mathrm{H2O}\mid\partial\Omega_{\mathrm{fuel,inlet}}} = \mathrm{w}_{\mathrm{H2O,in}}$ $\mathrm{w}_{\mathrm{H2S}\mid\partial\Omega_{\mathrm{fuel,inlet}}} = \mathrm{w}_{\mathrm{H2S,in}}$ $\mathbf{J}_{\mathbf{i}\mid\partial\Omega_{\mathrm{channel/anode}}} = \mathbf{J}_{\mathbf{i}\mid\partial\Omega_{\mathrm{anode\mid channel}}}$ $\mathbf{n}.\mathbf{J}_{\mathbf{i}\mid\partial\Omega_{\mathrm{fuel,outlet}}} = \mathbf{n}.w_i\rho\mathbf{v}$ $\mathbf{n}.\mathbf{J}_{\mathbf{i}\mid\partial\Omega_{\mathrm{wall}}} = 0$	Governing equation: $\nabla.\left[-\rho w_i \sum_{\substack{j=1 \\ i\neq j}}^{n} \widetilde{D}_{ij}\left(\nabla x_j + (x_j - w_j)\frac{\nabla \mathrm{p}}{p}\right) + (w_i \rho \mathrm{v})\right] = \mathrm{r_i}$ Boundary conditions: $\mathbf{J}_{\mathbf{i}\mid\partial\Omega_{\mathrm{channel/anode}}} = \mathbf{J}_{\mathbf{i}\mid\partial\Omega_{\mathrm{anode\mid channel}}}$ $\mathbf{n}.\mathbf{J}_{\mathbf{i}\mid\partial\Omega_{\mathrm{wall}}} = 0$	-

	Gas channel	Anode	Electrolyte
Momentum transport	Governing equation: $\rho(\mathbf{v}.\nabla\mathbf{v}) - \nabla.\left[\mu(\nabla\mathbf{v} + (\nabla\mathbf{v})^T) - \left(\frac{2}{3}\mu\right)(\nabla.\mathbf{v})\mathbf{I}\right] - \nabla P = 0$ $\nabla.(\rho\mathbf{v}) = 0$ Boundary conditions: Fully developed, Laminar flow at the fuel inlet $p_{channel\|\partial\Omega_{\text{wall}}} = P_{atm}$ $p_{channel\|\partial\Omega_{\text{channel/electrolyte}}} = p_{electrode\|\partial\Omega_{\text{channel/electrolyte}}}$ $\mathbf{v}_{channel\|\partial\Omega_{\text{channel/electrolyte}}} = \mathbf{v}_{electrode\|\partial\Omega_{\text{channel/electrolyte}}}$	Governing equation: $\left(\frac{\mu}{\kappa} + R_a\right)\mathbf{v} = \nabla.\left[-P\mathbf{I} + \frac{\mu}{\epsilon}(\nabla\mathbf{v} + (\nabla\mathbf{v})^T) - \frac{2}{3}\mu(\nabla.\mathbf{v})\mathbf{I}\right]$ $\nabla.(\rho\mathbf{v}) = Ra$ Boundary conditions: $\mathbf{v}_{electrode\|\partial\Omega_{\text{channel/electrolyte}}} = \mathbf{v}_{channel\|\partial\Omega_{\text{channel/electrolyte}}}$ $p_{electrode\|\partial\Omega_{\text{channel/electrolyte}}} = p_{channel\|\partial\Omega_{\text{channel/electrolyte}}}$ $\mathbf{v}\|_{\partial\Omega_{\text{wall}}} = 0$	

	Gas channel	Anode	Electrolyte
Electronic charge transport	-	Governing equation: $\nabla.(-\sigma_{el}^{eff}\nabla\emptyset_{\mathrm{el}}) = i_V$ Boundary conditions: $\phi_{el(a)}\vert_{\partial\Omega_{\mathrm{anode/channel}}} = 0$ $\mathbf{n}.\mathbf{i_e}\vert_{\partial\Omega_{\mathrm{wall}}} = 0$ $\mathbf{n}.\mathbf{i_e}\vert_{\partial\Omega_{\mathrm{anode/electrolyte}}} = 0$	
Ionic charge transport	-	Governing equation: $\nabla.(-\sigma_{ion_{an}}^{eff}\nabla\emptyset_{ion_{an}}) = -i_V$ Boundary conditions: $\mathbf{n}.\mathbf{i_i}\vert_{\partial\Omega_{\mathrm{wall}}} = 0$ $\mathbf{n}.\mathbf{i_i}\vert_{\partial\Omega_{\mathrm{electrode/channel}}} = 0$ $\mathbf{i}_{\mathbf{i}\vert\partial\Omega_{\mathrm{electrolyte/anode}}} = \mathbf{i}_{\mathbf{i}\vert\partial\Omega_{\mathrm{anode\vert electrolyte}}}$	Governing equation: $\nabla.(-\sigma_{ion}\nabla\emptyset_{ion}) = 0$ Boundary conditions: $\emptyset_{ion(c)}\vert_{\partial\Omega_{cathode/electrolyte}} = \emptyset_{\mathrm{el(c)}} - \mathrm{E_c}^{eq}$ $\mathbf{i}_{\mathbf{i}\vert\partial\Omega_{\mathrm{electrolyte/anode}}} = \mathbf{i}_{\mathbf{i}\vert\partial\Omega_{\mathrm{anode\vert electrolyte}}}$

3.4 Input Parameters

In this section, all the input parameters that had been used in the governing equations of transport model and in the anode electrochemistry including kinetic model parameters are summarized. In addition to these parameters, geometric and microstructural parameters needed to calculate the TPB length are tabulated. The gas phase thermodynamic properties are calculated as a function of temperature and using the JANAF thermochemical tables.

3.4.1 Transport model parameters

The governing equations of the transport model contain physically meaningful parameters. Density, viscosity and permeability are the parameters needed for the momentum transport equation. Gas density, at a given pressure and temperature can be calculated by the ideal gas equation:

$$\rho = \frac{pM_g}{RT} \tag{3.61}$$

p, M_g, R and T are the pressure, molecular weight , gas constant and temperature respectively. Viscosity of gases at low pressure can be calculated using the Chapman-Enskog relation:

$$\mu = 26.69 \times 10^{-8} \frac{\sqrt{1000 M_i T}}{\sigma_i^2 \Omega_i^{2,2}(T^*)} \tag{3.62}$$

σ_i is the collision diameter (in nm) and $\Omega_i^{2,2}$ is a collision integral and is a function of reduced temperature (Brodkey and Hershey 1988). Reader is referred to Brodkey and Hershey (1988) for the values of these parameters. An average viscosity for the mixture can be calculated by the following expression:

$$\mu_{\text{mix}} = 0.5 \left[\sum_{i=1} x_i \, \mu_i + \frac{1}{\sum_{i=1} \frac{x_i}{\mu_i}} \right] \tag{3.63}$$

κ is the permeability of the gas and is calculated by the Carman-Kozeny relation :

$$\kappa = \frac{{d_p}^2}{72\tau}\frac{\epsilon_g^3}{(1-\epsilon_g)^2} \tag{3.64}$$

d_p, τ and ϵ_g are the average particle diameter, tortuosity and the porosity respectively.

Binary diffusion coefficient and density are the parameters needed for the species transport. The binary diffusion coefficient, D_{ij} can be calculated from the Fuller-Schettler-Giddings Correlation (Reid, Prausnitz, and Poling 1987):

$$D_{ij} = \frac{3.16\times10^{-8}\,T^{1.75}}{p\left(v_i^{\frac{1}{3}}+v_j^{\frac{1}{3}}\right)^2}\left[\frac{1}{M_i}+\frac{1}{M_i}\right]^{0.5} \tag{3.65}$$

M_i and M_j are the molar weights and v_i and v_j are the molar diffusion volumes of species i and j. Effective binary diffusion coefficient is calculated by:

$$D_{ij}^{eff} = \frac{\epsilon}{\tau}D_{ij} \tag{3.66}$$

Effective ionic and electronic conductivity are the parameters needed for the ionic and electronic charge transport. Ionic conductivity of electrolyte σ_{ion} is equal to the conductivity of pure ionic conducting phase (σ_{ion}^0) and is calculated as:

$$\sigma_{ion}^0 = \frac{\sigma_{0\_ion}}{T}\exp\left(-\frac{E_{ion}}{RT}\right) \tag{3.67}$$

E_{ion} and σ_{0_ion} are the activation energy of O^{2-} conduction and Pre factor of O^{2-}conduction. Conductivity of pure electronic conducting phase σ_{el}^0 is calculate by:

$\sigma_{el}^0 = 3.27\times10^4 - 10.653\mathrm{T}$

(3.68) Calculation of the effective conductivities of the porous anode based on percolation and coordination-number theory and using the pure solid phase conductivities is shown in Appendix A. Table 3-2 summarizes the transport model parameters.

Table 3-2: Model parameters of transport phenomena

Parameter	Description/formula	Numerical value	Reference
τ	Tortuosity	3.5	Zhu et al. (2005)
κ	Gas permeability	$1\times10^{-16}\,m^2$	Zhu et al. (2005)
ϵ	Porosity of the porous electrode	0.35	Zhu and Kee (2008)
v_i	Molar diffusion volume of species	$v_{H2O}=12.7\times10^{-6}$ $v_{H2}=7.07\times10^{-6}$ $v_{H2S}=20.96\times10^{-6}$	Taylor and Krishna (1993)
σ_{ion}	Ionic conductivity of electrolyte	$2.67\,\frac{S}{m}$	Zhu and Kee (2008)
σ_{0_ion}	Pre factor of O^{2-} conduction	$8.855\times10^{+7}\,\frac{S.K}{m}$	Zhu and Kee (2008)
E_{ion}	Activation energy of O^{2-} conduction	$9000\,\frac{J}{mol}$	Zhu and Kee (2008)
σ_{el}^{eff}	Effective electronic conductivity of anode	$2680\,\frac{S}{m}$	Zhu and Kee (2008)
$\sigma_{ion\_an}^{eff}$	Effective ionic conductivity of anode	$0.127\,\frac{S}{m}$	Zhu and Kee (2008)

3.4.2 Kinetic model parameters

The parameters and constants that are needed to calculate the volumetric current density including the parameters required for K_{H2} and i^*_{H2} are listed in table 3-3 with their corresponding values. K_{H2} (based on Zhu *et al.* formulations) and i^*_{H2} are calculated by the following expressions:

$$K_{H2} = \frac{\gamma_0}{A_{des}\Gamma^2\sqrt{2\pi RTW_{H2}}}.\exp(\frac{E_{des}}{RT}) \quad (3.69)$$

$$i^*_{H2} = i^*_{ref,H2}\exp[-\frac{E_{a,H2}}{R}\left(\frac{1}{T}-\frac{1}{T_{ref}}\right)] \quad (3.70)$$

Table 3-3: Kinetic Model parameters

Parameter	Description/formula	Numerical value	Reference
E_{des}	Activation energy for the H_2 desorption reaction	88.12 $\frac{\text{kJ}}{\text{mol}}$	Zhu *et al.* (2005)
A_{des}	Pre-exponential factor for the H_2 desorption reaction	5.59 $\times 10^{+19}$ $\frac{\text{s.cm2}}{\text{mol}}$	Zhu *et al.* (2005)
Γ	Surface site density of Ni	2.6×10^{-9} $\frac{\text{mol}}{\text{cm2}}$	Zhu *et al.* (2005)
γ_0	Sticking coefficient	0.01	Zhu *et al.* (2005)
K_{H2}	Equilibrium constant of H_2 adsorption	1.409×10^{-5} $\frac{1}{\text{Pa}}$	Zhu and Kee (2008)
$E_{a,H2}$	Activation energy	120 $\frac{\text{kJ}}{\text{mol}}$	Zhu and Kee (2008)
T_{ref}	Reference temperature	800 ºC	Zhu *et al.* (2005)

Parameter	Description/formula	Numerical value	Reference
$i^*_{ref,H2}$	Reference exchange current density factor	$4.8\times10^{9}\ \frac{\mathrm{A}}{\mathrm{m3}}$	Zhu and Kee (2008)
i^*_{H2}	Exchange current density factor	$1.205\times10^{9}\ \frac{\mathrm{A}}{\mathrm{m3}}$	Zhu and Kee (2008)
K_{H2_DFT}	DFT based calculated H_2 adsorption equilibrium constant	$3.48\times10^{-7}\frac{1}{\mathrm{Pa}}$	Monder and Karan (2010)
K_{H2S_DFT}	DFT based calculated H_2S adsorption equilibrium constant	$1.1083\times10^{+7}\ \frac{1}{\mathrm{Pa}}$	Monder and Karan (2010)
L_{TPB_ref}	Reference TPB length per unit volume	$8.8\times10^{+11}\ \frac{1}{\mathrm{m2}}$	Zhu and Kee (2008)
L_{TPB}	Calculated TPB length per unit volume	$8.8\times10^{+11}\ \frac{1}{\mathrm{m2}}$	Zhu and Kee (2008)
α_a	Anodic charge transfer coefficient	1.5	Zhu and Kee (2008)
α_c	Cathodic charge transfer coefficient	0.5	Zhu and Kee (2008)

3.4.3 Geometrical Parameters

The geometrical parameters include the dimensions of the half-cell anode model and the microstructural parameters needed to calculate the effective properties and TPB length and are listed in table 3-4.

Table 3-4: Geometric and microstructural parameters

Parameter	Description	Numerical value
d_p	Mean particle diameter $d_p = \frac{1}{\frac{\psi_{Ni}}{2R_{Ni}} + \frac{\psi_{YSZ}}{2R_{YSZ}}}$	1 μm
ϵ	Porosity of the porous electrode	0.35
ψ_{YSZ}	YSZ volume fraction	0.42
ψ_{Ni}	Ni volume fraction	0.23
R_{Ni}	Radius of the Ni particles	0.5 μm
R_{YSZ}	Radius of the YSZ particles	0.5 μm
L_{anode}	Anode thickness	500 μm
$L_{electrolyte}$	Electrolyte thickness	20 μm

The operating conditions are listed in table 3-5:

Table 3-5: Operating conditions considered

Parameter	Description	Numerical value
$x_{H2,in}$	Inlet H_2 molar fraction	$0.97 - x_{H2S,in}$
$x_{H2O,in}$	Inlet H_2O molar fraction	0.03

Parameter	Description	Numerical value
$x_{H2S,in}$	Inlet H_2S molar fraction	Varying from 0.0001 ppm to 1000 ppm
$V_{fuel,inlet}$	Mean inlet fuel velocity	700 ºC
T	Operating temperature	700 ºC

The detailed calculation of the inlet fuel velocity is given in Appendix C.

In the early stages of the work, a low permeability of 1×10^{-16} m^2 calculated from Carman-Kozeny relation was employed in the model. For this permeability, the model predicted a high pressure built-up across the anode (from the anode/gas channel interface to the anode/electrolyte interface). At this permeability the pressure built-up across the anode is in the range of 1.8×10^5 Pa to 7×10^5 Pa for the cell voltage changing from 0.91V to 0.41V. Change of pressure across the anode was tested for permeability ranging from 1×10^{-16} m^2 to 1×10^{-12} m^2. Pressure built-up across the anode at permeability of 1×10^{-12} m^2 is in the range of 90 Pa to 810 Pa for the cell voltage changing form 0.91V to 0.41V. In addition to the simulations at the calculated permeability value of 1×10^{-16} m^2, the simulations were also tested for permeability of 1×10^{-12} m^2. The Base Case performance model is the 2D multiphysics performance model with reported parameters in table 3-2 to table 3-5, with the permeability value of 1×10^{-12} m^2. Base Case performance model will the basis for our simulation in the following sections.

3.5 Solution method

All half-cell porous anode models were solved using COMSOL Multiphysics. COMSOL Multiphysics is a modeling package that uses finite element method and solves partial differential equations or ordinary differential equations describing any physical process. It has a graphic user interface for all the modeling steps of geometry generation, meshing, setting the differential equations and boundary conditions, solving and post-processing the results. The PARDISO direct solver package was used to solve all the governing equations of the model described by PDEs. For the meshing, a quadrilateral mesh that is controlled by setting the number of grid points at the boundaries of the electrode was used. The mesh generated for the 2D half-cell model has 28160 quadrilateral elements. A finer mesh is applied for the electrode/electrolyte interface because of the electrochemical reaction occurring at the interface and therefore the higher gradients. Number of nodes on different edges varies depending on the dimensions of the edges. For example the number of nodes on the length of the gas channel was chosen as 200. Grid independence was tested by comparing current density result of performance model (with overage dependent kinetic) against a mesh 1.5 times denser at cell voltage of 0.91V. The relative error in the current density was of the order of 1×10^{-6} between the mesh used in this work with 28160 elements and the finer mesh with 43800 elements. The hydrogen concentrations were also compared for the two different meshes at the outlet of the gas channel. The relative difference is of the order of 1×10^{-6}. Figure 3-3 shows the cross section in the gas channel at which the H_2 mole fractions are compared. Figure 3-4 shows the H_2 mole fraction in the outlet of the gas channel cross-section for both mesh sizes.

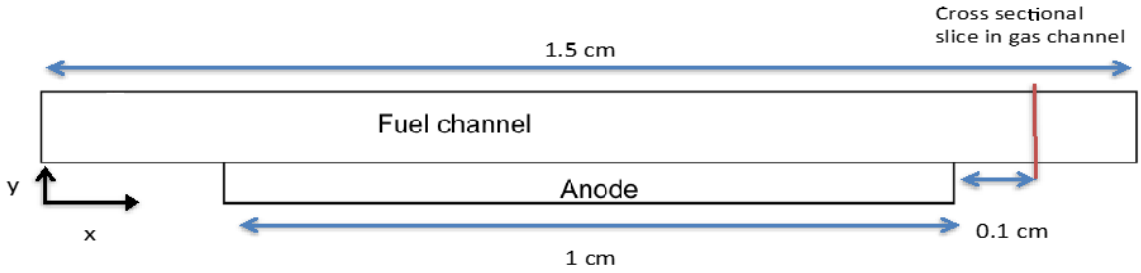

Figure 3-3: Schematic figure of half-cell and the cross section in gas channel at x=0.0135 m

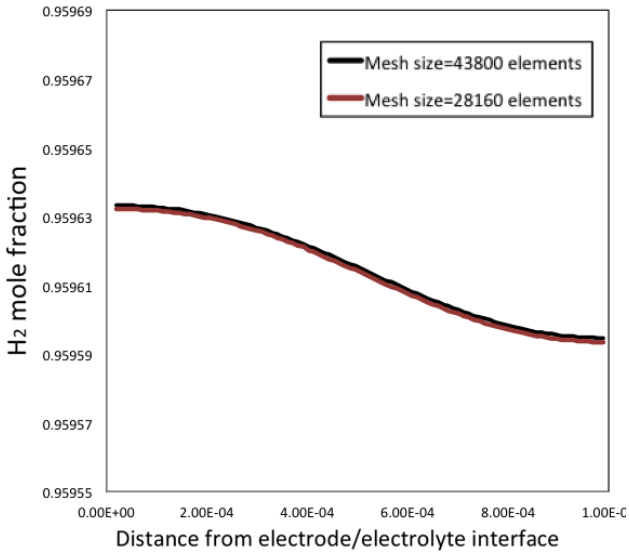

Figure 3-4: H_2 mole fraction in gas channel for different meshes at x=0.0135

Each simulation of the half-cell model presented in this chapter was verified for the mass and species conservation. Conservation of mass implies that sum of the mass flux entering the fuel channel and the mass flux added through the electrolyte should be equal to the mass flux leaving the gas channel. Conservation of species implies that the inlet molar flux should equal the outlet molar flux and the molar flux consumed/generated in the reaction.

3.6 Results and discussion

The **multiphysics electrochemical performance** is completed by implementing the kinetic models (that were developed in Chapter two) into the 2-dimentional multiphysics porous anode model. Different multiphysics electrochemical performance models are presented in figure 3-1. The following subsections will be discussed in the results and discussion section:

- General features of the results from multiphysics performance model are presented with the Base Case parameters in
- Cell performance predictions for feed mixture without H_2S impurities are presented for both coverage-dependent and coverage-independent performance models.
- Cell performance predictions for feed mixture containing H_2S impurities are presented. Relative loss in the cell performance and relative increase in the cell resistance due to the sulfur poisoning are calculated and compared to the experimental results.

3.6.1 General features of the results from multiphysics performance model

In this section, the general features of the results generated by multiphysics performance model such as, the pressure, velocity, concentration, and potential gradients as well as the rate of reaction in the model domains are examined for the base case parameters and a coverage-dependent kinetic model.

Pressure profile:

The pressure profile in domains of the anode and gas channel is shown in figure 3-5 at zero H_2S content and cell voltage of 0.91 V.

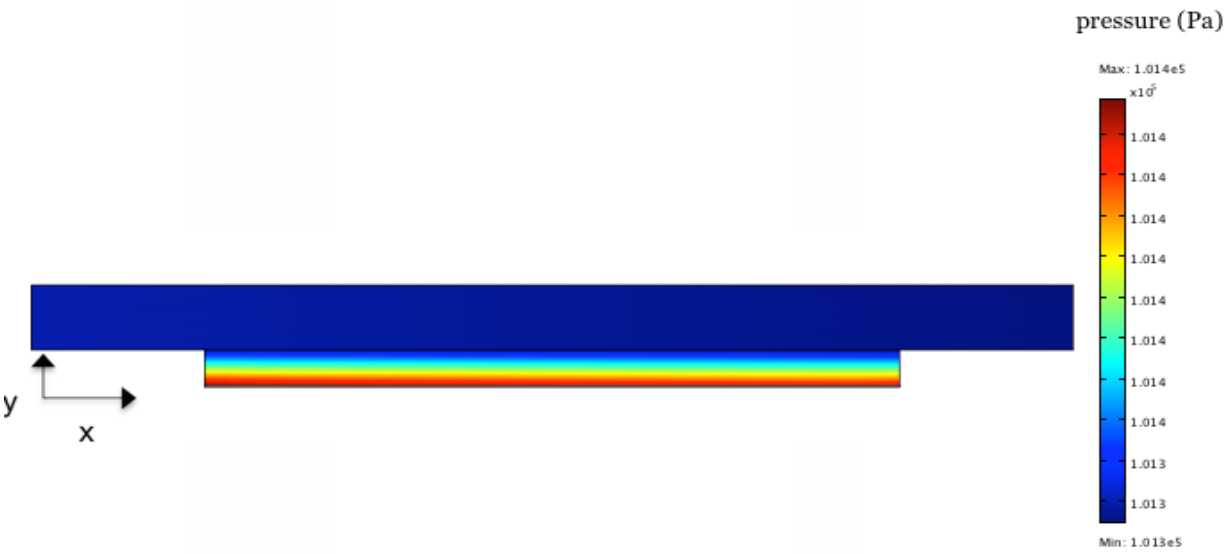

Figure 3-5: Pressure profile in the anode and gas channel domains

The pressure in the gas channel remains almost constant. The pressure drop along the gas channel (inlet to outlet) is negligibly small and approximately 10 Pa. The pressure in the anode porous domain increases from $1.0133\times10^{+5}$ Pa to $1.0142\times10^{+5}$ Pa, from the channel/electrode interface to the electrode/electrolyte interface, i.e. an increase of 90 Pa. This behavior may be counterintuitive unless one realizes that there is a net mass production in the active region of the porous anode. As per the overall, HOR stoichiometry for every 2g of gaseous hydrogen consumed, 18g of water is produced. That is, there is a net increase in the gas-phase mass flow rate, which comes from the oxygen ion present in the electrolyte phase, i.e. the solid phase. Addition of the mass to the porous anode domain changes the momentum balance. Momentum transport equation in the anode domain is the Brinkman equation that takes into account the changes in momentum balance due to mass production via the term $R_a\mathrm{v}$. Increase in the pressure profile that is calculated by this equation shows the effect of increase in momentum due to the mass production. Reaction rate increases in the anode from the channel/electrode interface to the electrode/electrolyte interface.

The effect of H_2S and sulfur poisoning is examined on the pressure profile in a cross sectional slice in the middel of the anode (from the anode/fuel channel interface to anode/electrolyte interface), as it is shown in figure 3-6. Figure 3-7 shows the pressure line profiles in this cross section at zero, 0.1 and 10 ppm H_2S and at cell voltage of 0.91 V .

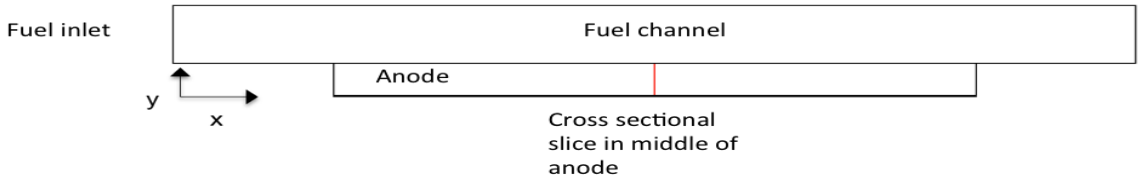

Figure 3-6: Schematic figure of the half-cell and the cross-sectional slice in the middle of anode

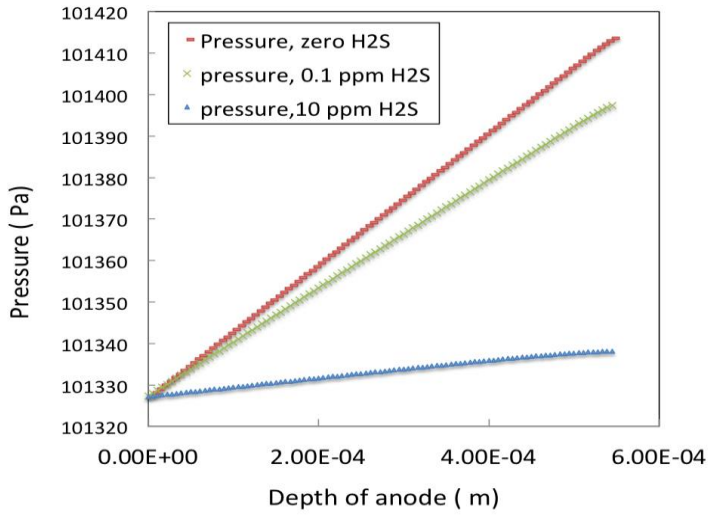

Figure 3-7: Pressure line profiles across the depth of the anode at x=0.075 (m) and y=570(μm) to y= 20 (μm) for feed mixture containing three H_2S concentrations

Due to higher rate of reaction and H_2O production at lower H_2S concentration, the increase of pressure is higher at lower H_2S concentration.

Velocity field profile:

The velocity field for feed mixture containing zero H_2S at cell voltage of 0.91 V is shown in figure 3-8. The velocity distribution in the gas channel shows the viscous effect of the wall on the fuel.

Figure 3-8: Velocity field in anode and gas channel domains for the base case condition.

Species partial pressure and concentration profiles:

The concentration and partial pressure profiles of the species H_2 and H_2O at the cell voltage of 0.91 V and zero H_2S concentration are shown in figure 3-9, 3-10, 3-11 and 3-12, respectively. H_2 mole fraction and partial pressure decrease along the gas channel and across the anode (from

anode/gas channel interface to anode/electrolyte interface) due to H_2 consumption. H_2O mole fraction and partial pressure increase along the gas channel and across the anode due to H_2O production.

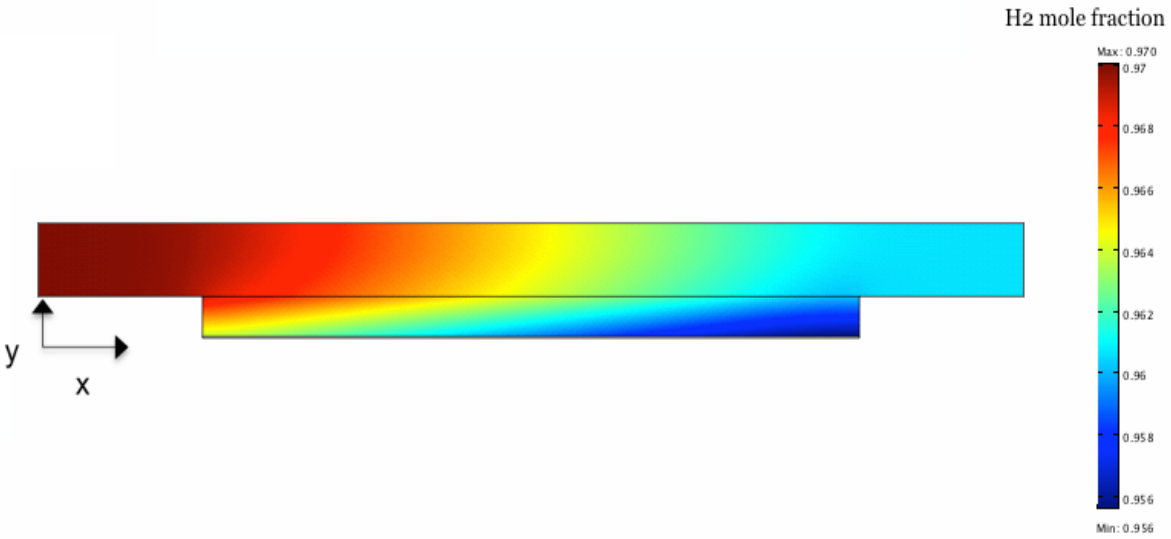

Figure 3-9: H_2 mole faction profile in anode and gas channel domains for the base case condition

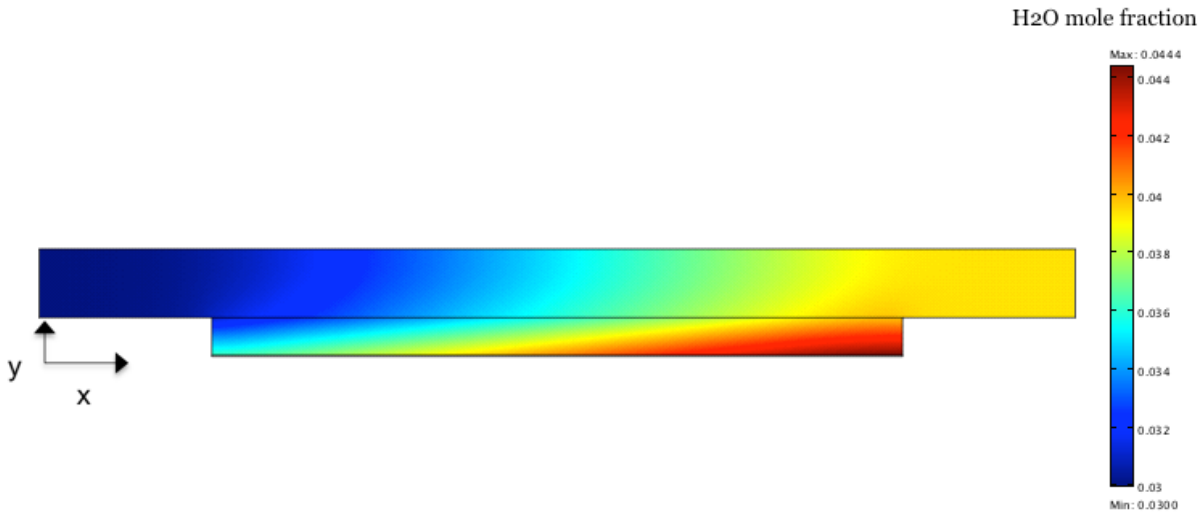

Figure 3-10: H_2O mole faction profile in anode and gas channel domains for the base case condition

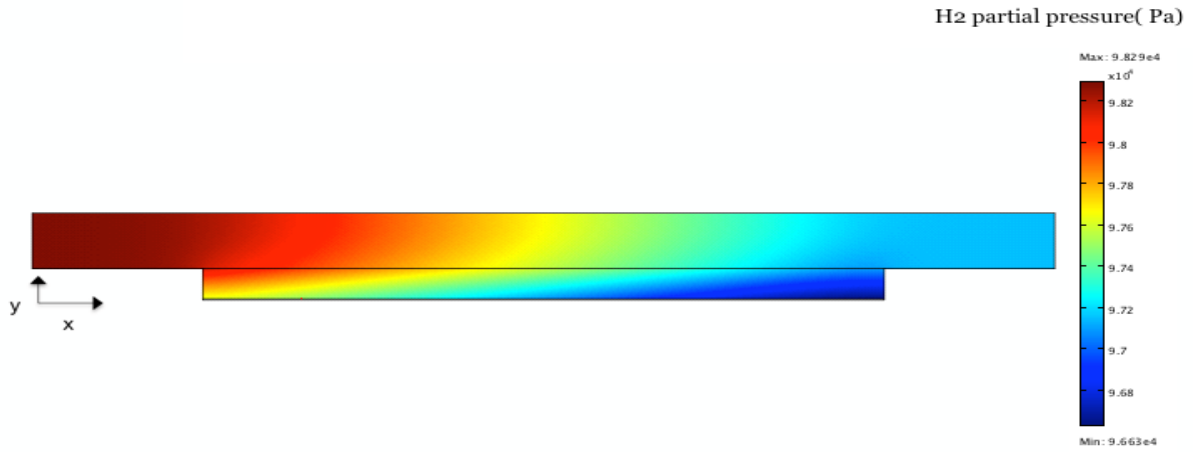

Figure 3-11: H_2 partial pressure profile in anode and gas channel domains for the base case condition

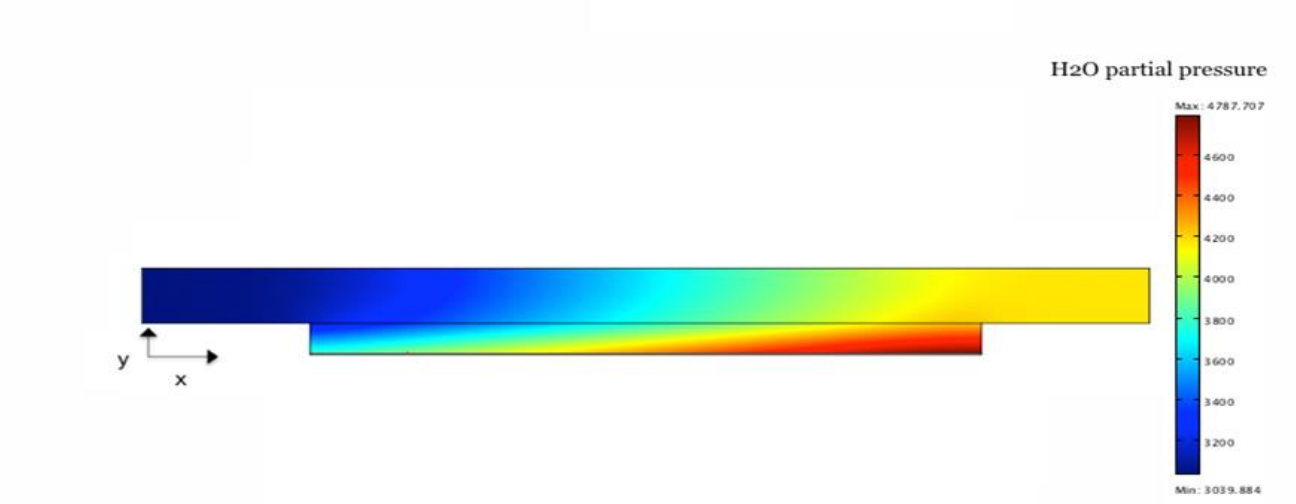

Figure 3-12: H_2O partial pressure profile in anode and gas channel domains for the base case condition.

In order to observe the effect of sulfur poisoning, H_2 and H_2O concentration line profiles are presented at different H_2S concentrations. H_2S concentration and partial pressure line profiles are also examined for 10ppm inlet H_2S concentration. Figures 3-13 and 3-14 show the line profiles of H_2 and H_2O mole fraction for feed mixture containing zero and 10 ppm H_2S in the middle of anode, (as depicted in figure 3-6). Due to the effect of sulfur poisoning and lower rate of H_2 consumption, decrease of the H_2 mole fraction at 10 ppm H_2S inlet concentration is less than the decrease of H_2 mole fraction at zero H_2S inlet concentration. Lower increase in the H_2O mole fraction is observed for feed mixtures with 10 ppm H_2S than that with zero H_2S inlet concentration. This behavior is due to the lower rate of reaction and H_2O production as the result of sulfur poisoning.

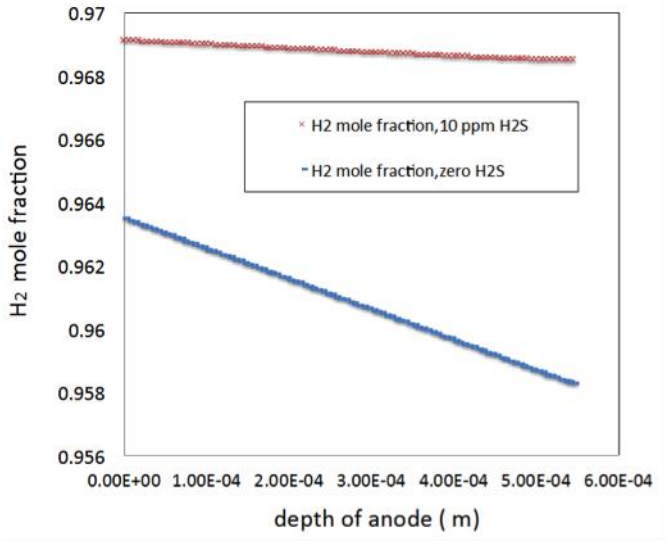

Figure 3-13: H_2 mole fraction distribution across the depth of the anode at x=0.075 m and y=570 μm to y= 20 μm for feed mixture containing zero and 10 ppm H_2S at cell voltage of 0.91 V.

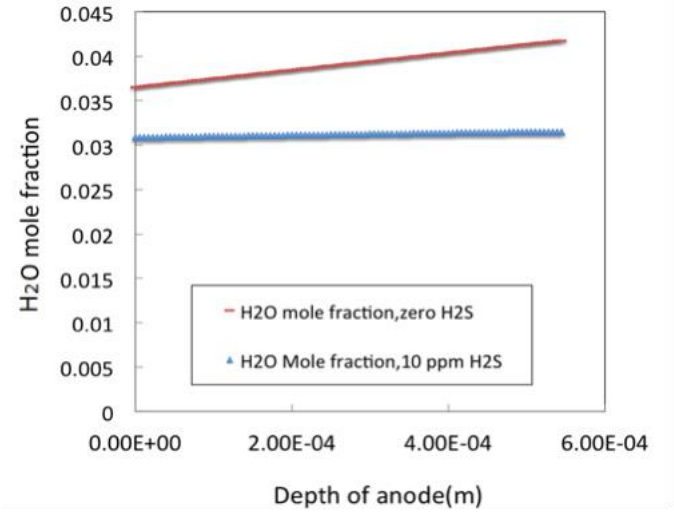

Figure 3-14: H_2O mole fraction distribution across the depth of the anode at x=0.075 m and y=570 μm to y= 20 μm for feed mixture containing zero and 10 ppm H_2S at cell voltage of 0.91 V.

Figure 3-15 and 3-16 show the H_2S mole fraction and partial pressure line profiles for feed mixture containing 10 ppm H_2S in the middle of anode, (as depicted in figure 3-6). The H_2S mole fraction and partial pressure decrease in the anode domain in the middle of anode. A gradient in H_2S concentration is observed in the anode domain, in spite the fact that H_2S is not getting consumed or generated. This behavior can be explained by considering the net mass flux in the anode domain from electrolyte towards the gas channel due to the net mass production in the anode. This causes a convective flux of H_2S from the electrolyte towards the gas channel. As H_2S is not being consumed or generated, the total H_2S flux should remain zero. Having the convective flux of H_2S towards the gas channel causes the H_2S diffusive flux to be towards the electrolyte, resulting in a decreasing H_2S gradient in the anode domain.

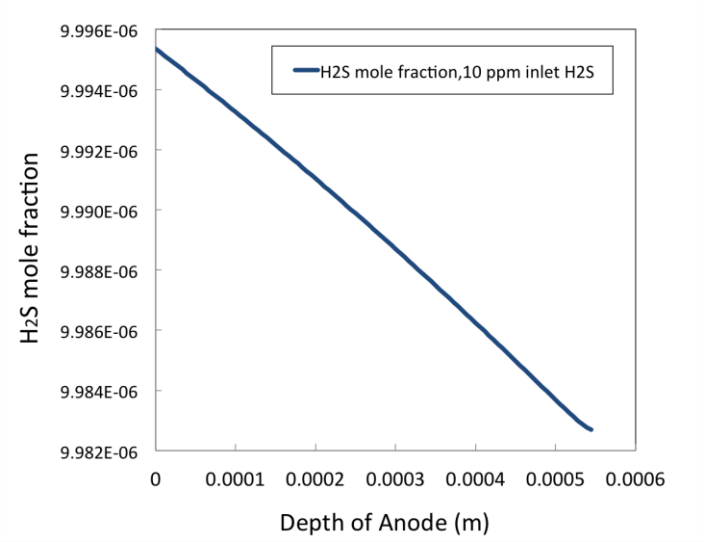

Figure 3-15: H_2S mole fraction distribution across the depth of the anode at x=0.075 m and y=570μm to y= 20 μm for feed mixture containing 10 ppm H_2S at cell voltage of 0.91 V.

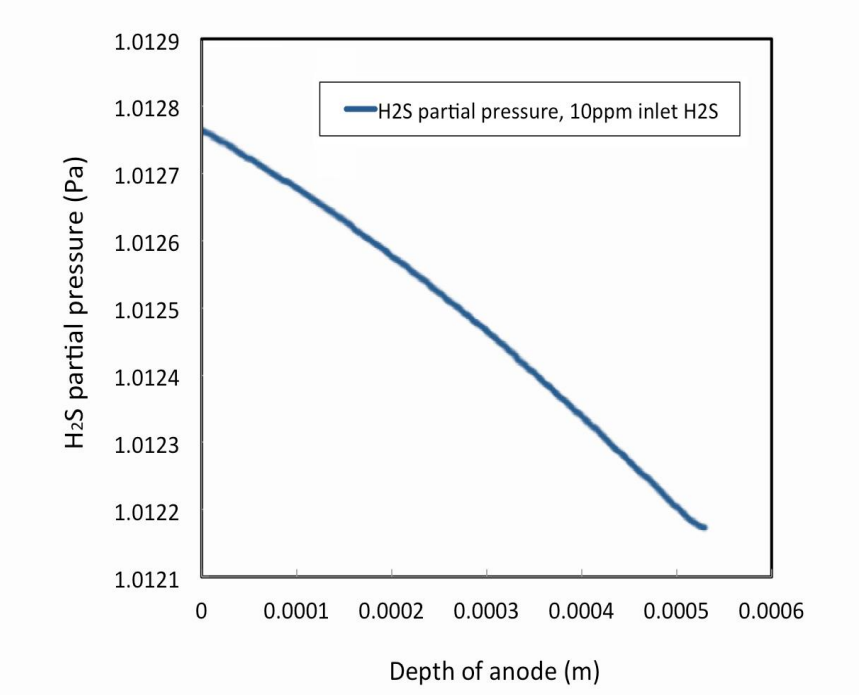

Figure 3-16: H_2S partial pressure distribution across the depth of the anode at x=0.075 m and y=570μm to y= 20 μm for feed mixture containing 10 ppm H_2S at cell voltage of 0.91 V.

Potential distribution profile:

The distribution of electrical potential arises from the transport of charges. This results in a distributed activation overpotential, which then can result in a distributed reaction rates. It may be recalled that the overpotential in this work is defined as the difference between equilibrium phase potential difference and the local phase potential difference. The phase potential difference here refers to the difference between the ion-conducting (YSZ) and the electron-conducting (Ni) material phases. Zero overpotential implies that no electrochemical driving force exists and

would result in a zero current generation. The activation overpotential for base case parameters at cell voltage of 0.91 V is shown in figure 3-17.

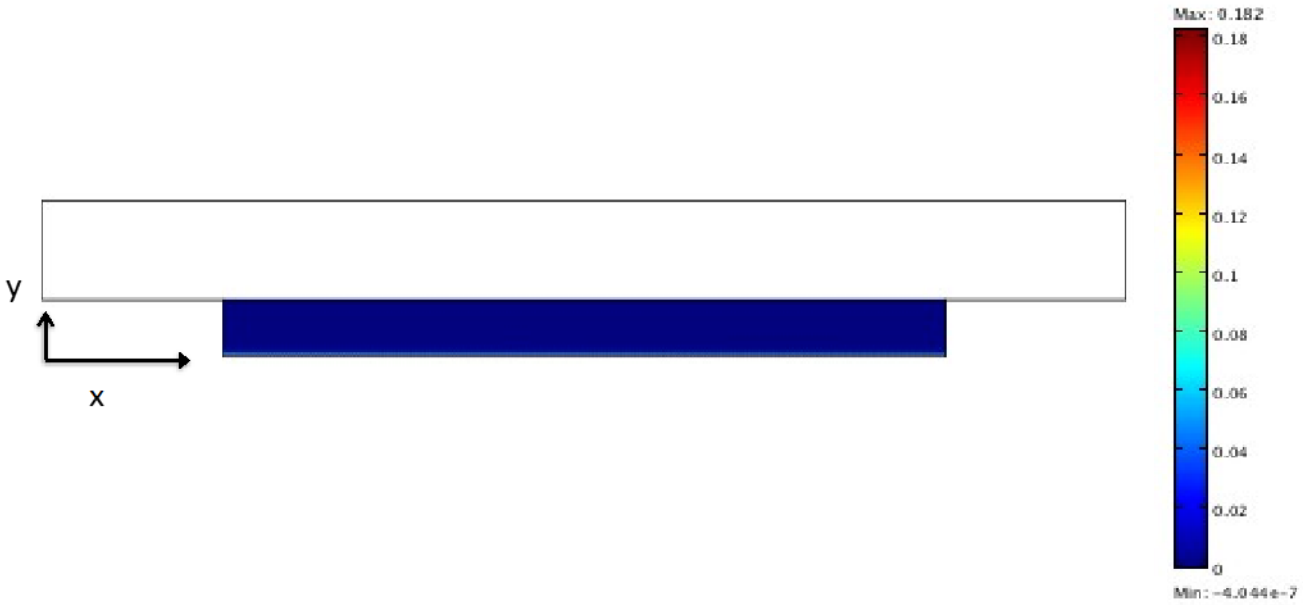

Figure 3-17: The activation overpotential for base case parameters at cell voltage of 0.91 V

For a better observation of the anode overpotential distribution in the model domain, the line profile of the anode overpotential across the depth of the anode for three H_2S concentrations is shown in figure 3-18.

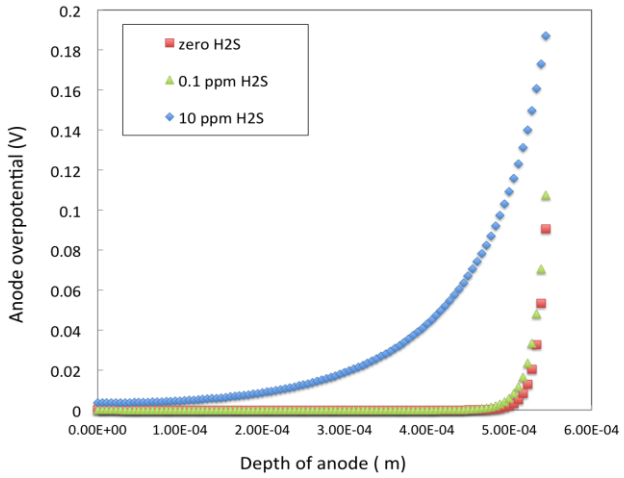

Figure 3-18: Anode activation overpotential line profiles in depth of anode, at x=0.075 m and y=570μm to y= 20μm, for base case parameters at cell voltage of 0.91 V

It can be noted that for the same cell potential of 0.91 V, in the case of higher H_2S in the reaction feed mixture, higher activation overpotential is observed. This would mislead a reader in interpreting that higher current is being generated in the case of feed with H_2S. However, the exchange current density is also diminished significantly in the presence of H_2S. The net result is that although the activation overpotential is higher for the case of feed with higher H_2S, a reduced exchange current density effects a lower current generation.

Reaction rate profile:

The rates of mass production per volume ($kg/m^3.s$) are compared for a rectangular area in the middle of anode as presented in figure 3-19. The rate of mass production profiles for base case parameters at three inlet H_2S concentrations of zero, 0.1 and 10 ppm at cell voltage of 0.91 V are shown in figure 3-20.

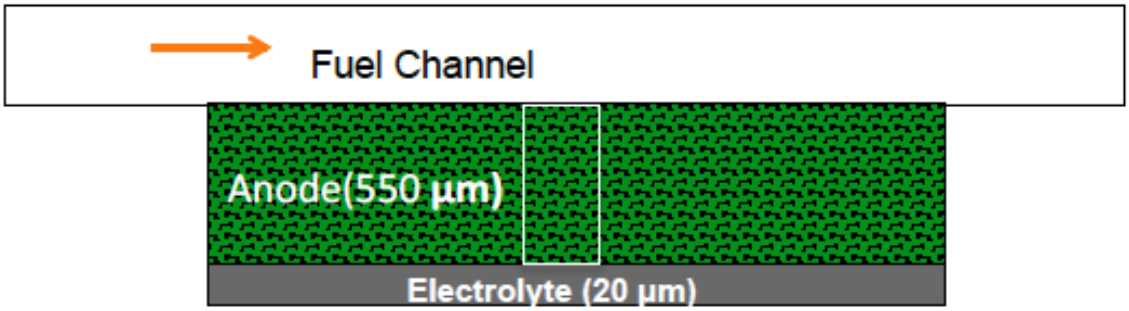

Figure 3-19: Schematic half-cell with rectangular area in the middle of anode

Rate of gas-phase mass generation.

The rate of mass production or the rate of reaction is higher for lower H_2S concentrations. Furthermore, most of the reaction occurs in a 10 microns thin region near the electrolyte/electrode interface.

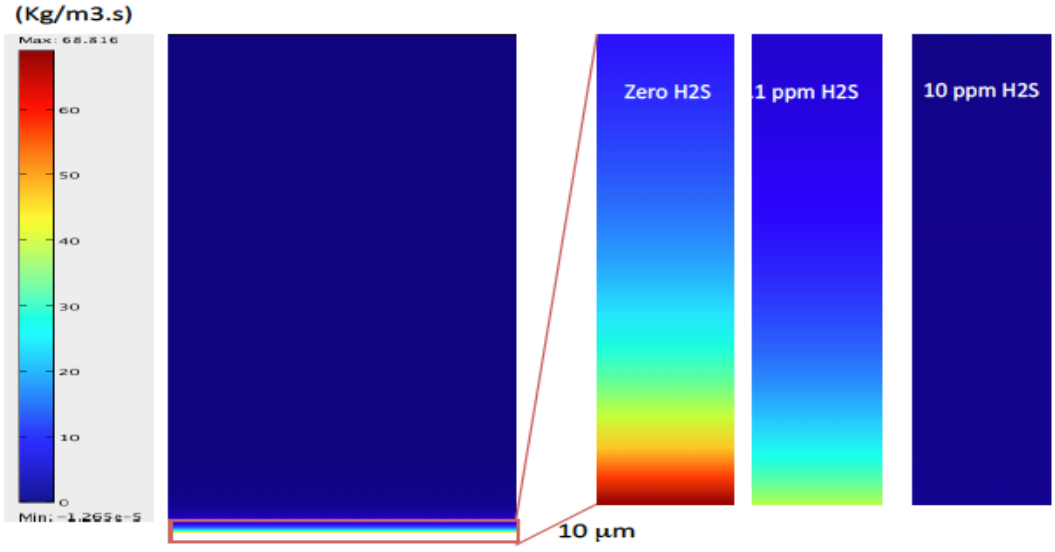

Figure 3-20: Mass production rate profiles for three inlet H_2S concentrations in the center of the porous anode region indicated in Figure 3-19. The zoomed view of the H_2S distribution in a 10-micron thin region near the electrode/electrolyte interface is shown.

3.6.2 Polarization behavior predicted by multiphysics performance model with pure H_2 feed mixture

The polarization behavior (i-V curves) predicted from three multiphysics performance models varying in the kinetic model formulation are shown in Figure 3-21 for the Base Case parameters and for feed mixture without H_2S impurities. The set of results are presented to examine how the differences in the kinetic formulations affect the polarization behavior under conditions where transport effects are also important.

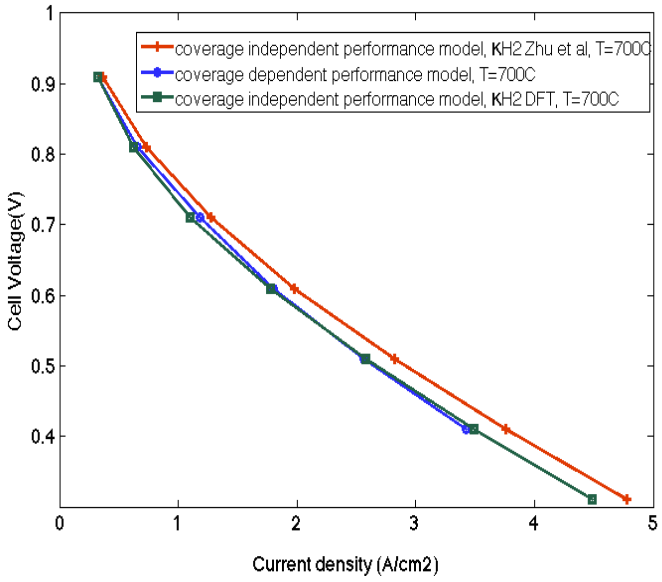

Figure 3-21: Polarization behavior (i-V curve) predicted by multiphysics performance model for reaction mixture without H_2S for Base Case parameters

The result from the coverage-independent model with K_{H2_DFT} is closer to the result from the coverage-dependent model. As expected, at any given cell potential, the kinetic model with highest exchange current density shows the highest current density.

3.6.3 Anode model predictions for feed mixtures containing H_2S

The polarization curves, relative loss in cell performance as a function of H_2S concentration and the relative increase in the anode activation overpotential are presented in the following sub-sections. The loss in cell performance can be compared for either galvanostatic (constant current) or potentiostatic (constant cell voltage) condition. In galvanostatic mode, the relative loss in a cell performance is considered as the loss in cell voltage at each H_2S concentration relative to zero H_2S concentration at a constant current density. Comparison of change in current density upon sulfur poisoning at potentiostatic mode introduces difficulty because the change in current also affects changes in ohmic and cathodic losses. On the other hand, by comparison at constant current density, the ohmic and cathode losses remain constant and any changes in cell potential upon changing H_2S content in the feed mixture arises from the change of anode performance due to sulfur poisoning only. In this work, simulations were performed at constant cell potentials to generate polarization curves. In order to calculate the loss in cell performance in galvanostatic mode, the polarization data at three H_2S concentration and zero H_2S concentration were fitted to an expression derived from Tafel approximation using linear least square regression method. The cell voltage and the loss in cell voltage at constant current density can be calculated using the fitted expression.

Tafel approximation derived expression is:

$$E_{cell} = E_{ocv} - i.ASR - \ln(i)\frac{RT}{(\beta+1).F} + \ln(i_0)\frac{RT}{(\beta+1).F} \tag{3.71}$$

In half-cell porous anode model the cathode overpotential is set to zero due to the assumption of ideal cathode boundary.

$$E_{cell} = E_{ocv} - \eta_{an} - \nabla V_{ohm} \tag{3.72}$$

Ohmic loss can be expressed as:

$$\nabla V_{ohm} = i.ASR \tag{3.73}$$

By estimating the activation overpotential via the Tafel equation and rearranging the equation, the anode activation overpotential can be expressed as:

$$i = i_0(\exp(\beta + 1)F\eta_{an}/RT\ ) \tag{3.74}$$

$$\eta_{an} = (\ln(i) - \ln(i_0))\frac{RT}{(\beta+1).F} = \ln(i)\frac{RT}{(\beta+1).F} - \ln(i_0)\frac{RT}{(\beta+1).F} \tag{3.75}$$

Therefore, the cell voltage can be written as:

$$E_{cell} = E_{ocv} - i.ASR - \ln(i)\frac{RT}{(\beta+1).F} + \ln(i_0)\frac{RT}{(\beta+1).F} \tag{3.76}$$

In order to calculate the cell voltage and the cell voltage drop at each current density, i-V curves are fitted to this expression. In addition to calculating the relative loss in the cell performance, the relative increase in the anode activation overpotential can also be calculated. The anode activation overpotential for each H_2S concentration and current density is calculated based on the fitting results using the corresponding expression:

$$\eta_{an} = (\ln(i) - \ln(i_0))\frac{RT}{(\beta+1).F} = \ln(i)\frac{RT}{(\beta+1).F} - \ln(i_0)\frac{RT}{(\beta+1).F} \tag{3.77}$$

Two points should be mentioned here: (i) The anode ovepotential that is being calculated here, is an average or effective anode overpotential accounting for the anode overpotential gradient in the anode domain; (ii) As the concentration losses are not considered in the fitted expression, ASR and η_{an}values obtained from fitting results, are affected by this simplifying assumption. Therefore their values do not represent the exact average area specific resistance and the average anode overpotential of the cell due to ignoring the concentration losses in the fitted expression. The loss in cell performance and increase in the cell resistance are compared with the experimental data as well.

Polarization behavior predicted by multiphysics electrochemical performance model with coverage-independent kinetic model

In this multiphysics performance model, both K_{H2} and K_{H2S} used in the kinetic formulation were calculated from the DFT calculations. The polarization curve results with Base Case parameters and reaction mixture with H_2S concentrations of zero, 0.1 ppm, 1 ppm and 10 ppm are shown in figure 3-22:

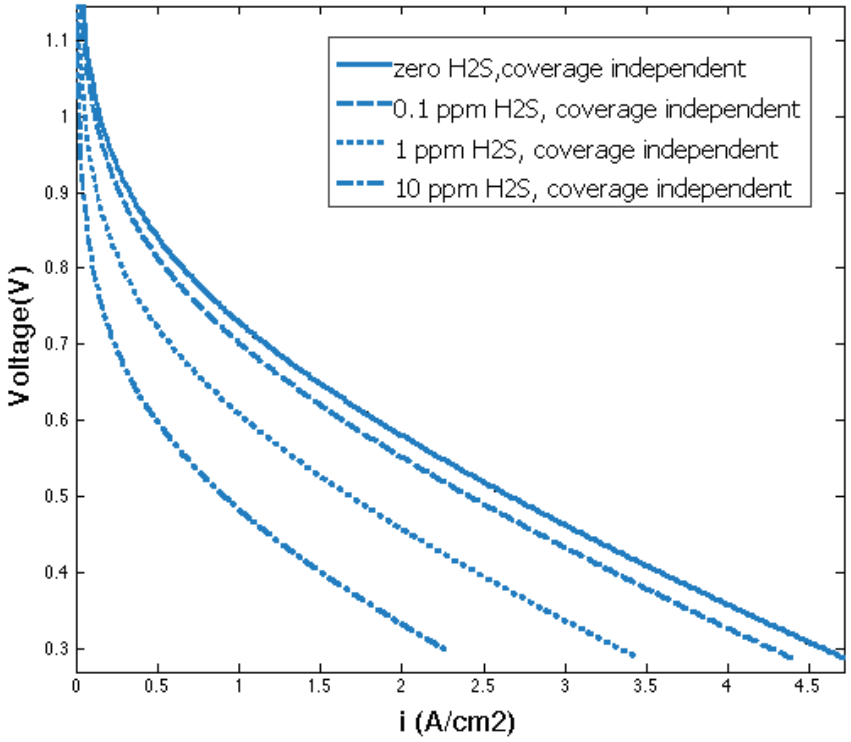

Figure 3-22: i-V curves of performance model using coverage independent kinetics, T=700ºC and other Base Case parameters.

As expected, for a given current density, the cell voltage decreases with an increase in the H_2S concentration. In order to calculate the loss in the cell voltage at a constant current density, i-V

curves are fitted to equation (3.76) by least square fitting method. The i-V curves of the 2-Dimensional multiphysics performance model with coverage-independent kinetic and their fitted curves are presented in Appendix D. The relative loss in the cell voltage at constant current density i_1 is calculated by the following expression:

$$\Delta E_{cell,R} = \frac{\Delta E_{cell}}{E_{cell|H2}} \tag{3.78}$$

$$\Delta E_{cell} = E_{cell|H2} - E_{cell|H2S} \tag{3.79}$$

$E_{cell|H2}$ and $E_{cell|H2S}$ represent calculated voltage from the fitting result at current density i_1 , for fuel mixture without H_2S and fuel mixture with H_2S content.

Figure 3-23 shows the relative loss in the cell voltage at three inlet H_2S concentrations of 0.1 ppm, 1 ppm and 10 ppm, at constant current density of 0.241 A/cm^2, 0.409 A/cm^2 and 2 A/cm^2 relative to cell voltage at zero inlet H_2S concentration. At constant current density, the losses in cathode and electrolyte remain unchanged and only the anode losses change due to change in H_2S content in the feed. Thus, the representation of this anode loss in terms of percentage loss in cell voltage is useful but can be skewed if the ohmic and cathodic losses dominate. Thus, the change in anode overpotential is a better and direct metric for comparison. The relative increase in the anode overpotential due to sulfur poisoning is a measure of the increase in the cell resistance at constant current density (i_1) and is calculated by the following expression:

$$\Delta\eta_{a,R} = \frac{\Delta\eta_a}{\eta_{a|H2}} \tag{3.80}$$

$$\Delta\eta_a = \eta_{a|H2S} - \eta_{a|H2} \tag{3.81}$$

In the above equations, $\eta_{a|H2S}$ and $\eta_{a|H2}$respresent the effective anode overpotential calculated at current density (i_1) from the i-V curve fitting results of 2D performance model for fuel mixture with H_2S impurities and fuel mixture without H_2S impurities, respectively.

Figure 3-24 shows the relative increase in the anode activation overpotential at three inlet H_2S concentrations of 0.1 ppm, 1 ppm and 10 ppm, at constant current densities of 0.241 A/cm^2, 0.409 A/cm^2 and 2 A/cm^2 relative to cell voltage at zero inlet H_2S concentration.

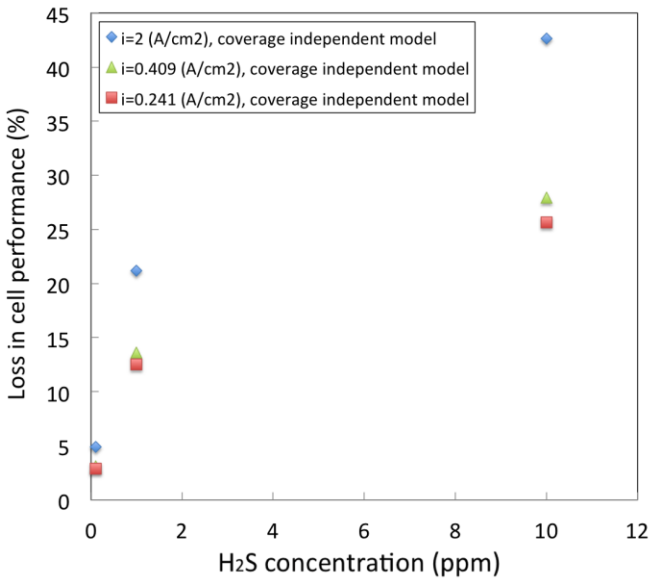

Figure 3-23: Relative loss in voltage at constant current predicted by coverage-independent performance model, T=700ºC with Base Case parameters

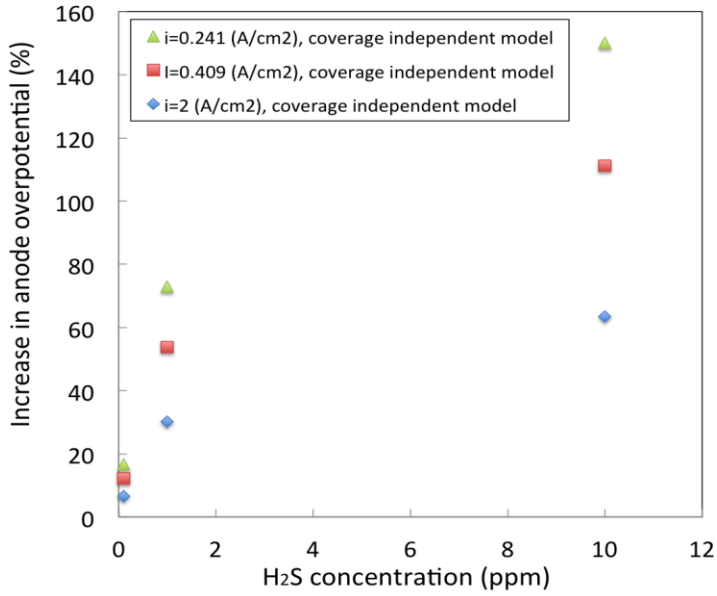

Figure 3-24: Relative increase in the anode activation overpotential predicted by coverage-independent performance model, T=700ºC with Base Case parameters

Polarization behavior predicted by multiphysics performance model with coverage-dependent kinetic

The polarization curve result of multiphysics performance model with coverage-dependent kinetic and Base Case parameters for reaction mixtures with H_2S concentrations of zero, 0.1 ppm, 1 ppm and 10 ppm are shown in figure 3-25:

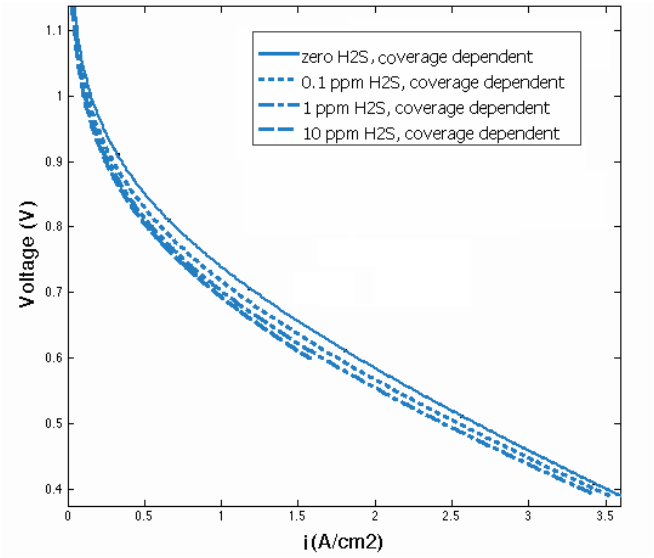

Figure 3-25: i-V curves of performance model with coverage dependent kinetics, T=700°C with Base Case parameters

As mentioned above, loss in the cell voltage is calculated by fitting i-V curves to the equation (3.76). The results of the fitting are presented in Appendix D. Figure 3-26 shows the relative loss in the cell voltage at three inlet H_2S concentrations of 0.1 ppm, 1 ppm and 10 ppm, at constant current denities of 0.241 A/cm^2, 0.409 A/cm^2 and 2 A/cm^2 relative to cell voltage at zero inlet H_2S concentration. Figure 3-27 shows the relative increase in the anode activation overpotential computed for three inlet H_2S concentrations of 0.1 ppm, 1 ppm and 10 ppm, at constant current denity of 0.241 A/cm^2, 0.409 A/cm^2 and 2 A/cm^2 relative to cell voltage at zero inlet H_2S concentration.

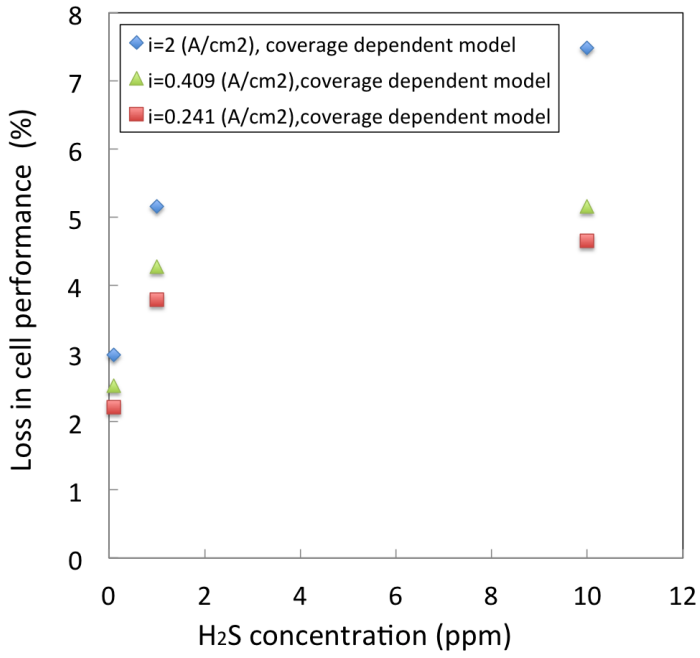

Figure 3-26: Relative loss in cell voltage at constant current predicted by coverage-dependent performance model, T=700ºC with Base Case parameters.

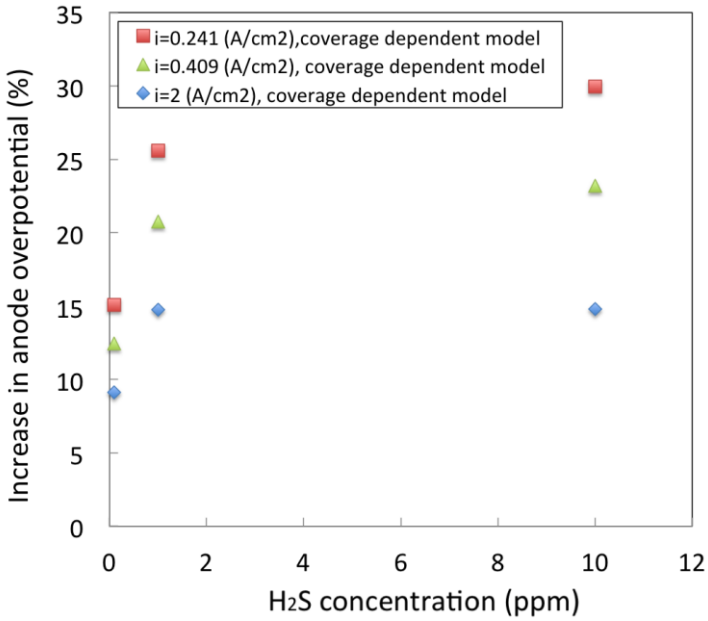

Figure 3-27: Relative increase in the anode activation overpotential predicted by coverage-dependent performance model, T=700°C with Base Case parameters.

For both coverage-dependent and coverage-independent performance models following trends could be observed: As expected, the poisoning increases with an increase in H_2S content of the fuel. Both relative loss in the cell performance and relative increase in the cell resistance predicted by performance models increase with increasing H_2S content of the fuel mixture. Also, both the relative loss in the cell performance and the relative increase in the cell resistance show a sharp increase at lower H_2S content, followed by a gentle increase at higher H_2S concentration. The 2D performance model with coverage-dependent kinetics predictions for loss in the cell performance is lower than the 2D performance model with coverage-independent kinetics, which is the same trends observed in Chapter two for kinetic models.

In both performance models at constant H_2S concentration, relative loss in cell performance is smaller at lower current densities, while the relative incresae in the cell resistance is smaller at higher current densities. This behavior might appear contradictory, as it is not clear whether it is better to work at higher current densities or lower current densities to decrease the sulfur poisoning effect. To better understand the behavior, two points should be mentioned here. First, a decrease in the cell voltage (ΔE_{cell}) is equal to the increase in the anode overpotential ($\Delta \eta_a$) due to the galvanostatic condition and zero cathode losses in our model.

$$E_{cell|H2} = E_{OCV} - i.ASR - \eta_{a|H2} \tag{3.82}$$

$$E_{cell|H2S} = E_{OCV} - i.ASR - \eta_{a|H2S} \tag{3.83}$$

$$\Delta E_{cell} = \eta_{a|H2S} - \eta_{a|H2} \tag{3.84}$$

$$\Delta E_{cell} = \Delta \eta_a \tag{3.85}$$

At constant current density, $\Delta \eta_a$ has a slight increase with the increase in the current density referring to the figures E1 and E1 in Appendix E. However, the relative loss in the cell voltage and relative increase in anode overpotential show different values as they are calculated relative to the initial cell voltage ($E_{cell|H2}$) and initial anode overpotential ($\eta_{a|H2}$) at zero H_2S content of fuel mixture, respectively:

$$\Delta E_{cell,R} = \frac{\Delta E_{cell}}{E_{cell|H2}} \tag{3.86}$$

$$\Delta \eta_{a,R} = \frac{\Delta \eta_a}{\eta_{a|H2}} \tag{3.87}$$

The reason of observing opposite trends in the $\Delta E_{cell,R}$ and $\Delta \eta_{a,R}$ upon the change of current density at constant H_2S content of fuel mixture is that the initial cell voltage ($E_{cell|H2}$) and initial anode overpotential ($\eta_{a|H2}$) have opposite behavior upon the change of current density. $E_{cell|H2}$

is higher at lower current density, while $\eta_{a|H2}$ is smaller at lower current density, making $\Delta E_{cell,R}$ and $\Delta\eta_{a,R}$ decrease and increase with decrease of current density respectively.

As mentioned earlier, the representation of the anode performance losses in terms of percentage loss in cell voltage can be skewed if the ohmic and cathodic losses dominate. Although in our model the cathode losses are zero, the ohmic losses are still considered in the calculation of the percentage loss in cell voltage. Therefore, the relative increase in the anode overpotential is a better metric for the cell performance evaluation.

Similar trends for the relative loss in cell performance and relative increase in cell resistance have been noted in experimental studies of Cheng *et al.* (Cheng, Zha, and Liu 2007) at 800ºC as it is presented in the next subsection. Again, the loss in the cell performance here is defined as the loss in the cell voltage at constant current density. Because of the galvanostatic condition and zero cathode losses of the model, the loss in the cell voltage is equal to the increase in the anode overpotential.

3.6.4 Comparing the relative loss in cell performance and relative increase in anode overpotential with experimental results

Cheng *et al.* has reported experimental data for relative loss in the cell voltage and relative increase in cell resistance at constant current density. In their work, an increase in the internal cell resistance ($\Delta R|_{H2S}$) due to sulfur poisoning is defined by the following expressions:

$$E_{cell|H2} = E_{OCV} - i.(R|_{H2}) \tag{3.88}$$

$$E_{cell|H2S} = E_{OCV} - i.(R|_{H2} + \Delta R|_{H2S}) \tag{3.89}$$

$$\Delta R_R = \frac{\Delta R|_{H2S}}{R|_{H2}} \tag{3.90}$$

$R|_{H2}$, $\Delta R|_{H2S}$ and ΔR_R represent the total cell resistance before sulfur poisoning, increase in total

cell resistance after sulfur poisoning and relative increase in the total cell resistance, respectiely. The ΔR_R can be compared to the relative increase in the anode overpotential ($\Delta\eta_{a,R}$) calculated from our model. $\Delta R_a$and ($\Delta\eta_{a,R}$) formulations are compared in Appendix F.

Figures 3-28 and 3-29 show the relative loss in cell performance at two current densities of 0.409 A/cm^2 and 0.241 A/cm^2 and relative increase in cell resistance at two current densities of 0.409 A/cm^2 and 0.241 A/cm^2 reported by Cheng *et al.* T=800ºC.

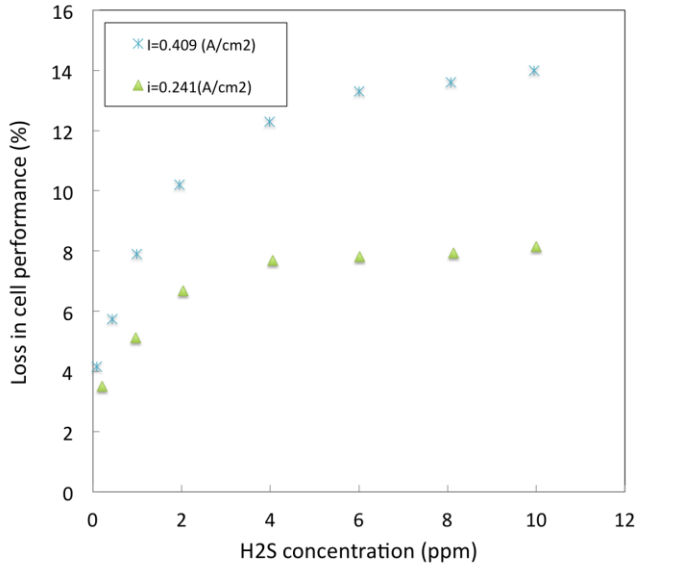

Figure 3-28: Relative loss in performance reported by experimental study (Cheng, Zha, and Liu , 2007), T=800ºC

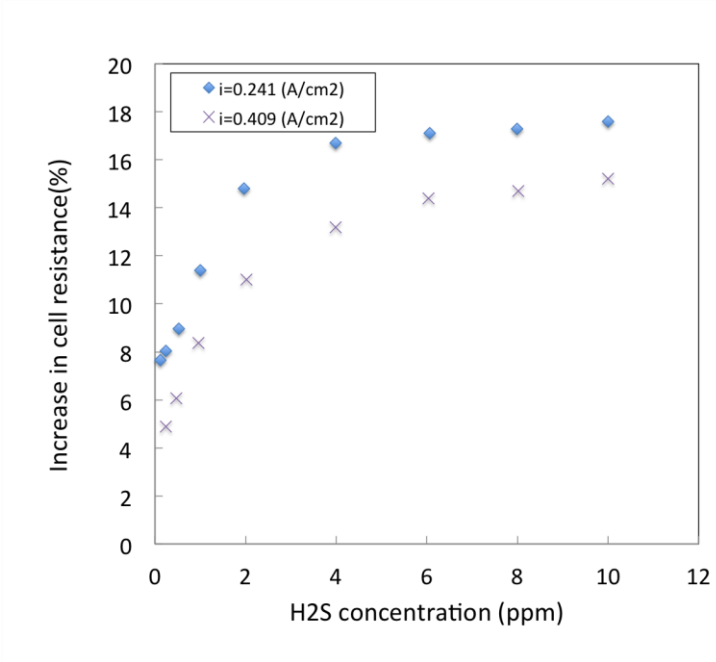

Figure 3-29: Relative increase in cell resistance reported by experimental study (Cheng, Zha, and Liu , 2007), T=800ºC

Similar trends in the experimental results and the performance model results can be observed:

-Increase in relative loss in cell performance and relative increase in the cell resistance by increase in the poisoning can be observed for both the experimental and performance model results.

- Smaller relative loss in cell performance at lower current densities and smaller relative incresae in the cell resistance at higher current densities can be observed for both the experimental and performance model results.

Coverage-dependent 2D performance model predictions are closer to the experimental results than the Coverage-independent 2D performance model predictions.

The purpose of the comparison is mainly to demonstrate that the model predictions have the similar trends as in experimental results.

3.7 Conclusion

A two-dimensional (2D) performance model that captures the effect of transport phenomena in addition to the kinetics of anode reaction in presence of H_2S was developed. The performance model is a 2D multiphysics model with porous anode domain that captures the gas-phase species transport, charged species transport and anode electrochemistry in addition to the kinetics of the H_2 electro-oxidation reaction in the presence of the S poisoning (coverage-dependent and coverage-independent kinetic models). The results of the 2D performance model indicates that the spatial distribution of the potential and species plays an important role in the performance predictions, due to the difference in the 2D performance model and kinetic model prediction. The cell performance diminution due to sulfur poisoning was evaluated by the 2D performance model predictions in terms of loss in the cell voltage and increase in the cell resistance at galvanostatic mode. The predictions shows an increasing trend in both the loss in the cell voltage and increase in the cell resistance upon the increase of the inlet H_2S content of the fuel. The predictions also indicate that for a constant inlet H_2S content, increase in the relative cell resistance is smaller at higher current densities. The 2D performance model with coverage-dependent kinetics predicts lower loss in the cell performance than the 2D performance model with coverage-independent kinetics, that is the same trends observed in chapter two for kinetic models.

The 2D model predictions when compared with experimental data in the literature showed similar trends of increase in the sulfur poisoning effect by increase in H_2S content and smaller increase in the relative cell resistance at higher current densities. Coverage-dependent 2D performance model

predictions are closer to the experimental results than the Coverage-independent 2D performance model predictions.

Chapter 4

Conclusion and Recommendations

4.1 Conclusion

A new kinetic model in the form of modified Butler-Volmer expression was derived to consider the effect of sulfur poisoning (caused by H_2S impurities) on the H_2 electro-oxidation in Ni-YSZ anodes of SOFCs. The new formulation is derived by adding the H_2S adsorption reaction on Ni to the set of elementary reactions for hydrogen oxidation reaction on Ni-YSZ three-phase region, previously proposed by Boer (1998). The H_2S adsorption reaction is modeled as an equilibrium reaction along with the equilibrium adsorption of H_2 on Ni. Two kinetic models for H_2S and H_2 adsorption were considered differing in the dependency of adsorption energies on sulfur and hydrogen surface coverages. Expectedly, both kinetic models predict a reduction in the current density with an increase in the H_2S concentration.

The kinetic model was implemented into a two-dimensional half-cell model with geometry comprising the anode gas channel, the porous anode and the electrolyte to study various transport effects on the sulfur poisoning effect. The 2D performance model captures the gas-phase species transport, charged species transport and anode electrochemistry with sulfur poisoning effects (coverage-dependent and coverage-independent kinetic models). Model shows that large gradients in overpotential exist over the anode thickness. In addition to that, gradients in the gas species concentration and surface coverage in the anode domain determine the local poisoning effect and the rate of electrochemical reaction. Local effect of sulfur poisoning on the rate of HOR reaction can be well explained by considering the mixed effect of local distribution of water vapour pressure, sulfur coverage and anode overpotential in the anode domain. Consistent with

the kinetic model, the 2D performance model shows that the loss in cell performance increases with an increase in H_2S content of the fuel. However, 2D performance model predicts lower relative loss in the current density than the kinetic model for the same H_2S content. Another ability of the 2D performance model is that it can predict the loss in cell performance at different anode overpotentials, while kinetic model predictions do not change at different anode overpotentials.

By comparing the 2D model predictions with the experimental results, similar trends of increase in the sulfur poisoning effect by increase in H_2S content and smaller increase in the relative cell resistance at higher current densities can be observed. Also, coverage-dependent 2D performance model predictions are closer to the experimental results than the coverage-independent 2D performance model predictions.

4.2 Recommendations

To improve the 2D model predictions, it is recommended that the Knudsen diffusion is added to the multicomponent gas species mass transport model. For better validation of the performance model predictions, the 2D performance model should employ experiment specific anode characteristics including the geometry, the anode microstructure and composition, and fuel composition. Experimental measurements wherein the anode losses can be isolated would be important for model validation. Such measurements can be performed using three-electrode setup with a reference electrode. The adsorption energies for the kinetic model were based on DFT studies on Ni (111) surface neglecting the effects of edge sites and other surface orientation in an actual Ni particle in the SOFC anode. Characterization of the Ni surface and determination of the adsorption energy accounting for these effects/features will improve the model.

References

Alstrup, Ib, Jens R. Rostrup-Nielsen, and Stig Røen. "High Temperature Hydrogen Sulfide Chemisorption on Nickel Catalysts." *Applied Catalysis* 1 (5): 303–314, 1981.

Bartholomew, C. H., P. K. Agrawal, and J. R. Katzer. "Sulfur Poisoning of Metals." *Advances in Catalysis* 31: 135–242, 1982.

Bartholomew, Calvin H. "Mechanisms of Catalyst Deactivation." *Applied Catalysis A: General* 212 (1): 17–60, 2001.

Bessler, Wolfgang G., Marcel Vogler, Heike Störmer, Dagmar Gerthsen, Annika Utz, André Weber, and Ellen Ivers-Tiffée. "Model Anodes and Anode Models for Understanding the Mechanism of Hydrogen Oxidation in Solid Oxide Fuel Cells." *Physical Chemistry Chemical Physics* 12 (42): 13888-13903, 2010.

Boer, Baukje de. SOFC Anode: Hydrogen Oxidation at Porous Nickel and Nickel/yttria- Stabilised Zirconia Cer*met Electrodes. PhD thesis, Universiteit Twente, Enschede, October 1998.*

Brodkey, R. S, and H. C Hershey. *Transport Phenomena: A Unifined Approach*. Brodkey Publishing, 1988.

Cheng, Zhe, Shaowu Zha, and Meilin Liu. "Influence of Cell Voltage and Current on Sulfur Poisoning Behavior of Solid Oxide Fuel Cells." *Journal of Power Sources* 172 (2): 688–693. 2007.

Den Besten, I. E., and P. W. Selwood. "The Chemisorption of Hydrogen Sulfide, Methyl Sulfide, and Cyclohexene on Supported Nickel Catalysts." *Journal of Catalysis* 1 (2): 93–102, 1962.

Farhad, Siamak, and Feridun Hamdullahpur. "Micro-Modeling of Porous Composite Anodes for Solid Oxide Fuel Cells." *AIChE Journal* 58 (6): 1893–1906, 2012.

Fedrigo, Doreen, and John Hontelez. "Sustainable Consumption and Production." *Journal of Industrial Ecology* 14 (1), 2009.

Feduska, W., and A. O. Isenberg. "High-Temperature Solid Oxide Fuel Cell—technical Status." *Journal of Power Sources* 10 (1): 89–102, 1983.

Forzatti, Pio, and Luca Lietti. "Catalyst Deactivation." *Catalysis Today* 52 (2): 165–181, 1999.

Galea, N.M., E.S. Kadantsev, and T. Ziegler. “Studying Reduction in Solid Oxide Fuel Cell Activity with Density Functional Theory- Effects of Hydrogen Sulfide Adsorption on Nickel Anode Surface.” *Journal of Physical Chemistry C* 111 (39): 14457–14468, 2007.

Grabow, Lars C., Britt Hvolbæk, and Jens K. Nørskov.“Understanding Trends in Catalytic Activity: The Effect of Adsorbate–Adsorbate Interactions for CO Oxidation Over Transition Metals.” *Topics in Catalysis* 53 (5-6): 298–310, 2010.

Haga, K., S. Adachi, Y. Shiratori, K. Itoh, and K. Sasaki. “Poisoning of SOFC Anodes by Various Fuel Impurities.” *Solid State Ionics* 179: 1427–1431, 2008.

Haile, Sossina M. “Fuel Cell Materials and Components.” *Acta Materialia*, The Golden Jubilee Issue. Selected topics in Materials Science and Engineering: Past, Present and Future, 51 (19): 5981–6000, 2003.

Hussain, M.M., X. Li, and I. Dincer. “Mathematical Modeling of Transport Phenomena in Porous SOFC Anodes.” *International Journal of Thermal Sciences* 46 (1): 48–56, 2007.

Hansen, John Bøgild.“Correlating Sulfur Poisoning of SOFC Nickel Anodes by a Temkin Isotherm.*”* *Electrochemical and Solid-State Letters* 11 (10): B178-B180, 2008.

Janardhanan, Vinod M., and Olaf Deutschmann. “Modeling of Solid-Oxide Fuel Cells.” *Zeitschrift Für Physikalische Chemie* 221 (4): 443–478, 2007.

Kee, R. J, Michael Elliott Coltrin, and Peter Glarborg. *Chemically Reacting Flow: Theory and Practice*. Hoboken, N.J.: Wiley-Interscience, 2003.

Kenney, Ben, Mikelis Valdmanis, Craig Baker, J.G. Pharoah, and Kunal Karan. “Computation of TPB Length, Surface Area and Pore Size from Numerical Reconstruction of Composite Solid Oxide Fuel Cell Electrodes.” *Journal of Power Sources* 189 (2): 1051–1059, 2009.

Landes, DAVID S.*The Unbound Prometheus,Technical Change and Industrial Development in Western Europe from 1750 to the Present*. Cambridge University Press, 2003.

Larminie, James, and Andrew Dicks. *Fuel Cell Systems Explained*. Chichester, West Sussex: J. Wiley, 2003.

Li, Ting Shuai, and Wei Guo Wang. “Sulfur-Poisoned Ni-Based Solid Oxide Fuel Cell Anode Characterization by Varying Water Content.” *Journal of Power Sources* 196 (4): 2066–2069, 2011.

Matsuzaki, Yoshio, and Isamu Yasuda.“The Poisoning Effect of Sulfur-Containing Impurity Gas on a SOFC Anode: Part I. Dependence on Temperature, Time, and Impurity Concentration.” *Solid State Ionics* 132 (3): 261–269, 2000.

McCarty, Jon G., and Henry Wise. “Thermodynamics of Sulfur Chemisorption on Metals. I. Alumina-Supported Nickel.” *The Journal of Chemical Physics* 72 (12): 1162-1167, 1980.

Monder, Dayadeep S., and Kunal Karan. “Ab Initio Adsorption Thermodynamics of H_2S and H_2 on Ni(111): The Importance of Thermal Corrections and Multiple Reaction Equilibria.” The Journal of Physical Chemistry C 114 (51): 22597–22602, 2010.

D. S. Monder and K. Karan. “Coverage Dependent Thermodynamics for Sulfur Poisoning of Ni Based Anodes.” ECS Transactions 57 (1): 2449–2458, 2013.

Monder, Dayadeep S., and Kunal Karan. “A Near Triple-Phase Boundary Region Model for H2S Poisoning od SOFC Anodes.” ECS Transactions, 35 (1) 977-985 (2011)

Rasmussen, Jens F.B., and Anke Hagen. “The Effect of H2S on the Performance of Ni–YSZ Anodes in Solid Oxide Fuel Cells.” *Journal of Power Sources* 191 (2): 534–541, 2009.

Reid, R. C., J. M. Prausnitz, and B. E. Poling. *The Properties of Gases and Liquids*. 4 th Edition. New York: McGraw-Hill, 1987.

Ryan, E.M., W. Xu, X. Sun, and M.A. Khaleel. “A Damage Model for Degradation in the Electrodes of Solid Oxide Fuel Cells: Modeling the Effects of Sulfur and Antimony in the Anode.” *Journal of Power Sources* 210: 233–242, 2012.

Saleh, J. M., C. Kemball, and M. W. Roberts. “Interaction of Hydrogen Sulphide with Nickel, Tungsten and Silver Films.” *Transactions of the Faraday Society* 57: 1771–1780, 1961.

Sasaki, K., K. Susuki, A. Iyoshi, M. Uchimura, N. Imamura, H. Kusaba, Y. Teraoka, et al. “H_2S Poisoning of Solid Oxide Fuel Cells.” *Journal of The Electrochemical Society* 153 (11): A2023-A2029, 2006.

Shishkin, M., and T. Ziegler. “Oxidation of H_2, CH_4, and CO Molecules at the Interface between Nickel and Yttria-Stabilized Zirconia: A Theoretical Study Based on DFT.” *The Journal of Physical Chemistry C* 113 (52): 21667–21678, 2009.

Singhal, Subhash C, and Kevin Kendall. *High-Temperature Solid Oxide Fuel Cells Fundamentals, Design, and Applications*. New York: Elsevier Advanced Technology, 2003.

Stambouli, A. Boudghene, and E Traversa. “Solid Oxide Fuel Cells (SOFCs): A Review of an Environmentally Clean and Efficient Source of Energy.” *Renewable and Sustainable Energy Reviews* 6 (5): 433–455, 2002.

Taylor, Ross, and R Krishna. *Multicomponent Mass Transfer*. New York: Wiley, 1993.

Vogler, Marcel, Anja Bieberle-Hütter, Ludwig Gauckler, Jürgen Warnatz, and Wolfgang G. Bessler. “Modelling Study of Surface Reactions, Diffusion, and Spillover at a Ni/YSZ Patterned Anode.” *Journal of The Electrochemical Society* 156 (5): B663-B672, 2009.

Wang, Jeng-Han, and Meilin Liu. “Computational Study of Sulfur–nickel Interactions: A New S–Ni Phase Diagram.” *Electrochemistry Communications* 9 (9): 2212–2217, 2007.

Yakabe, H., M. Hishinuma, M. Uratani, Y. Matsuzaki, and I. Yasuda. “Evaluation and Modeling of Performance of Anode-Supported Solid Oxide Fuel Cell.” *Journal of Power Sources* 86 (1): 423–431, 2000.

Zha, Shaowu, Zhe Cheng, and Meilin Liu. “Sulfur Poisoning and Regeneration of Ni-Based Anodes in Solid Oxide Fuel Cells.” *Journal of The Electrochemical Society* 154 (2): B201-B206, 2007.

Zhao, F, and A Virkar. “Dependence of Polarization in Anode-Supported Solid Oxide Fuel Cells on Various Cell Parameters.” *Journal of Power Sources* 141 (1): 79–95, 2005.

Zhu, Huayang, and Robert J. Kee. “Modeling Distributed Charge-Transfer Processes in SOFC Membrane Electrode Assemblies.” *Journal of The Electrochemical Society* 155 (7): B715-B729, 2008.

Zhu, Huayang, Robert J. Kee, Vinod M. Janardhanan, Olaf Deutschmann, and David G. Goodwin. “Modeling Elementary Heterogeneous Chemistry and Electrochemistry in Solid-Oxide Fuel Cells.” *Journal of The Electrochemical Society* 152 (12): A2427- A2440, 2005.

Appendix A

Triple phase boundary (TPB) and effective conductivity calculations

Percolation theory and particle coordination number theory are used to estimate the effective TPB length and effective ionic and electronic conductivities. It is assumed that the ionic and electronic conducting phases are composed of spherical particle overlapping with a contact angle of θ (Zhu and Kee , 2008). TPB length per unit volume is calculated by:

$$\lambda_{TPB}^{V} = l_{ed\_el}\, n_{tot} \zeta_{ed} \zeta_{el} P_{ed}\, P_{el}\, \frac{Z_{el} Z_{ed}}{Z_{tot}} \tag{A.1}$$

l_{ed_el} is the TPB length per contact between electrode and electrolyte. n_{tot} is the number of the particles of the composite anode per unit volume. ζ_{ed} and ζ_{el} are the number fractions of electrode and electrolyte particles . P_{ed} and P_{el} are the probability of the electronic phase particle and ionic phase particle to fall into a percolated cluster of its own phase, respectively. Z_{ed} and Z_{el} are the coordination number of the electronic phase and ionic conducting phase composite electrode. Z_{tot} is the overall average coordination number.

$$n_{tot} = \frac{1-\emptyset_g}{\left(\frac{4}{3}\right)\pi[\zeta_{ed} r_{ed}^3 + \zeta_{el} r_{el}^3]} \tag{A.2}$$

$$\zeta_{ed} = \frac{\psi_{ed/} r_{ed}^3}{\psi_{ed/} r_{ed}^3 + \psi_{el/} r_{el}^3} \tag{A.3}$$

$$\zeta_{el} = \frac{\psi_{el/} r_{el}^3}{\psi_{ed/} r_{ed}^3 + \psi_{el/} r_{el}^3} \tag{A.4}$$

$$\psi_{el} = \frac{\emptyset_{el}}{\emptyset_{el} + \emptyset_{ed}} \tag{A.5}$$

$$\psi_{ed} = \frac{\emptyset_{ed}}{\emptyset_{el} + \emptyset_{ed}} \tag{A.6}$$

$$Z_{ed} = 3 + \frac{(Z_{tot}-3)\, r_{ed}^2}{\zeta_{ed} r_{ed}^2 + \zeta_{el} r_{el}^2} \quad \text{(A.7)}$$

$$Z_{el} = 3 + \frac{(Z_{tot}-3) r_{el}^2}{\zeta_{ed} r_{ed}^2 + \zeta_{el} r_{el}^2} \quad \text{(A.8)}$$

r_{ed} and r_{el} are the radius of the electronic and ionic phases. The probability of the α particles, P_α is calculated by:

$$P_\alpha = [1 - \left(\frac{4.236 - Z_{\alpha\alpha})}{2.471}\right)^{2.5}]^{0.4} \quad \text{(A.9)}$$

Coordination number of the α particles with β particles, $Z_{\alpha\beta}$ is the average number of the β particles in contact with the α particles and is calculated by:

$$Z_{\alpha\beta} = \zeta_\beta \frac{Z_\alpha\, Z_\beta}{Z_{\alpha\beta}} \quad \text{(A.10)}$$

The effective conductivity of the composite anode can also be calculated using the percolation theory:

$$\sigma_\alpha^{eff} = \sigma_\alpha^0 [(1 - \emptyset_g)\psi_\alpha P_\alpha]^\gamma \quad \text{(A.11)}$$

σ_α^0 is the conductivity of the pure electronic or ionic phase.

Appendix B

Details of the Coverage-dependent thermodynamic

The standard Gibbs free energy of species i, is calculated from equations:

$$G_i^0 = H_i^0 - TS_i^0 \quad \text{(B.1)}$$

$$H_i^0 = E_{el,i} + E_{ZPV,i} + E_{th,i} + PV_{m,i} \quad \text{(B.2)}$$

In these equations, H_i^0 and S_i^0 are the molar enthalpy and entropy of species i, $E_{el,i}$ is the electronic energy at 0ºK , $E_{ZPv,i}$ is the zero point vibrational energy, $E_{th,i}$ is the thermodynamic thermal corrections including the rotational, vibrational and translational terms due to elevated temperature. The electronic energy is calculated from DFT calculation. Zero point vibrational energy, thermodynamic thermal correction and molar entropy are calculated form the statistical thermodynamics. For surface adsorbed species, $PV_{m,i}$ is ignored due to the negligible molar volume of surface species. If surface species are strongly adsorbed and fully dissociated, the surface translational and rotational modes can be ignored (Monder and Karan, 2010). The partition function for species i (q_i) that include all energy levels available to i on the surface can be calculated by:

$$q_i = q_i(elec)q_i(vib) = q_i(elec)\Pi(q_{i,k}(vib)) \quad \text{(B.3)}$$

$q_i(elec)$ and $q_i(vib)$ are the electronic and vibrational partition functions. $\Pi(q_{i,k}(vib))$ is the product over the number of vibrational modes for adsorbed species i. The electronic and vibrational partition functions are defined as:

$$q_i(elec) = \exp(-\frac{E_i}{k_B T}) \quad \text{(B.4)}$$

$$q_{i,k}(\text{vib}) = \frac{\exp\left(\frac{-h\nu_{i,k}}{2k_BT}\right)}{(1-\exp(\frac{-h\nu_{i,k}}{k_BT}))} \quad \text{(B.5)}$$

Ei is the electronic energy of adsorption for species i and is defined as a function of coverage of adsorbed molecules of all the species on the surface. $\nu_{i,k}$ is the k^{th} vibrational frequency for species i. h and k_B are the Planck and Boltzmann constants. According to the derivation of chemical potential from partition function in statistical thermodynamics and by assuming that the vibrational frequencies are coverage independent, the chemical potential of adsorbed species is defined as (Monder and Karan, 2013)

$$\mu_i = \partial(\sum(E_i\theta_i))/\partial\theta_i + k_BT\ln(\theta_i/(\theta_v q_i(\text{vib})) \quad \text{(B.6)}$$

$\theta_v$is the fraction of sites on the surface that are vacant.

$$\theta_v = 1 - \sum(\theta_i) \quad \text{(B.7)}$$

The electronic energy change on adsorption is given by this equation with i being the adsorbed species, n_i being the number of adsorbate atoms. N* is the number of surface sites.

$$E_{ads,i} = \{E_{ni,ads+slab(N^*)} - n_iE_{i,gas} - E_{slab(N^*)}\}/n_i \quad \text{(B.8)}$$

$E_{ni,ads+slab(N^*)}$ represents the total electronic energy of the slab with N* surface sites and Ni adsorbates, $E_{i,gas}$ represent the gas phase electronic energy of the adsorbed species and $E_{slab(N^*)}$ represents the total electronic energy of the clean slab with N* surface sites . In order to calculate the electronic energy of adsorption, $\sum(E_i\theta_i)$, Monder and Karan (2013) calcultaed Eads,i at different surface coverages with DFT methods and fitted a function that was previously

developed by (Grabow et al, 2010) to the calculated values of Eads at different surface coverages.

$$\sum(\mathrm{E_i}\theta_\mathrm{i}) = E_H\theta_H + E_S\theta_S = E_H(0)\theta_H + E_S(0)\theta_S + \alpha_H\{\theta_H - \theta_H(0)\}^2 + \alpha_S\{\theta_S - \theta_S(0)\}^2 + \beta_{HS}\theta_H{}^*\theta_S{}^* \quad \text{(B.9)}$$

$E_H(0)$ and $E_S(0)$ are the zero coverage adsorption energies; $\theta_H(0)$ and $\theta_S(0)$ are the threshold coverages; α_H and α_S are the self-interaction parameters and $\beta_{H2}$is the binary interaction parameter. The values of these parameters are obtained by fitting the function to the DFT based calculated values of $E_{ads,i}$. $\theta_H{}^*$ and $\theta_S{}^*$are the effective coverage of hydrogen and sulfur. For H and S coverages lower than $\theta_H(0)$ and $\theta_S(0)$, it is assumed that no adsorbate–adsorbate interactions are present. For any H coverage higher than$\theta_H(0)$, the H-H and H-S interactions are considered and for any S coverage higher than$\theta_S(0)$, the S-S and H-S interactions are considered. Therefore, the self-interaction terms of $\alpha_H\{\theta_H - \theta_H(0)\}^2$ and $\alpha_S\{\theta_S - \theta_S(0)\}^2$ are considered only if $\theta_H > \theta_H(0)$ and $\theta_S > \theta_S(0)$ respectively. The variables $\theta_H{}^*$ and $\theta_S{}^*$are the notations for effective coverage of hydrogen and sulfur and are used to calculate the energy contributions of hydrogen and sulfur interactions. $\theta_H{}^*$and $\theta_S{}^*$are zero in the low coverage region ($\theta_H < \theta_H(0)$ and $\theta_S < \theta_S(0)$). The term $\theta_H{}^*\theta_S{}^*$ is equal to $\theta_H\theta_S$ for $\theta_H > \theta_H(0)$ and $\theta_S > \theta_S(0)$. (Grabow, Hvolbæk, and Nørskov 2010). For other conditions, the detailed calculations of $\theta_H{}^*\theta_S{}^*$are presented in Grabow (2010). Using the relation for electronic energy, the first term in the surface species chemical potential can be developed for hydrogen and sulfur species:

$$\partial(\sum(\mathrm{E_i}\theta_\mathrm{i}))/\,\partial\theta_\mathrm{H} = E_H(0) + 2\alpha_H\{\theta_H - \theta_H(0)\} + \beta_{HS}\theta_S{}^* \quad \text{(B.10)}$$

$$\partial(\sum(\mathrm{E_i}\theta_\mathrm{i}))/\,\partial\theta_\mathrm{S} = E_S(0) + 2\alpha_S\{\theta_S - \theta_S(0)\} + \beta_{HS}\theta_H{}^* \quad \text{(B.11)}$$

The term $2\alpha_H\{\theta_H - \theta_H(0)\}$ is included if $\theta_H > \theta_H(0)$ and $\beta_{H2}{\theta_S}^*$is included if $\theta_S^* > 0$. The term $2\alpha_S\{\theta_S - \theta_S(0)\}$ is included if $\theta_S > \theta_S(0)$ and $\beta_{H2}{\theta_H}^*$is included if $\theta_H^* > 0$

The chemical potential of surface species are calculated by substituting the electronic energy and vibrational energy terms into the equation (B.6). Chemical potential of the H and S surface species are calculated by the relations (B.12) and (B.13):

$$\mu_H = E_H(0) + 2\alpha_H\{\theta_H - \theta_H(0)\} + \beta_{HS}{\theta_S}^* + \mathrm{k_B T}\ln\left(\frac{\theta_H}{(1-\theta_S-\theta_H).\Pi\left\{\frac{\exp\left(-h\frac{\nu_{H,k}}{2k_BT}\right)}{1-\exp\left(-h\frac{\nu_{H,k}}{2k_BT}\right)}\right\}}\right) \qquad \text{(B.12)}$$

$$\mu_S = E_S(0) + 2\alpha_S\{\theta_S - \theta_S(0)\} + \beta_{HS}{\theta_H}^* + \mathrm{k_B T}\ln\left(\frac{\theta_S}{(1-\theta_S-\theta_H).\Pi\left\{\frac{\exp\left(-h\frac{\nu_{k,S}}{2k_BT}\right)}{1-\exp\left(-h\frac{\nu_{kS,}}{2k_BT}\right)}\right\}}\right) \qquad \text{(B.13)}$$

Appendix C

Inlet velocity calculations

The mean velocity of fuel is calculated based on the desired or target current density and the fuel utilization factor (U_f) to be considered as 50%. The desired current density value of 2500 A/cm^3 is considered as the target current density value (i_t). The molar flow rate of the inlet fuel can be calculated as:

$$\dot{n}_{Fuel} = \frac{i_t.w_{ed}.l_{ed}.H_{ed}}{2FU_f.n_{H2}} \quad \text{(C.1)}$$

n_{H2} is the inlet H_2 concentration. w_{ed}, l_{ed} and H_{ed} are the width, length and the height of the electrode.

Inlet fuel velocity can be calculated by:

$$u_{fuel} = \frac{\dot{n}_{Fuel}.RT}{A.P} \quad \text{(C.2)}$$

$$A = w_{ed}.H_{ch} \quad \text{(C.3)}$$

P and A are the pressure and the channel inlet area. H_{ch} is the height of the fuel channel.

$$u_{fuel} = \frac{\frac{i_t.w_{ed}.l_{ed}.H_{ed}}{2FU_f.n_{H2}}.RT}{w_{ed}.H_{ch}.P} = \frac{i_t}{2FU_f.n_{H2}}.\frac{RT}{P}.\frac{l_{ed}H_{ed}}{H_{ch}} \quad \text{(C.4)}$$

Appendix D

i-V curves fitting results of 2D performance model

The results of fitting the i-V curves of the coverage-independent performance model to equation (3.76) by linear least square method with their R-square values are shown in figure D-1, D-2, D-3 and D-4 for 0, 0.1, 1 and 10 ppm H_2S respectively.

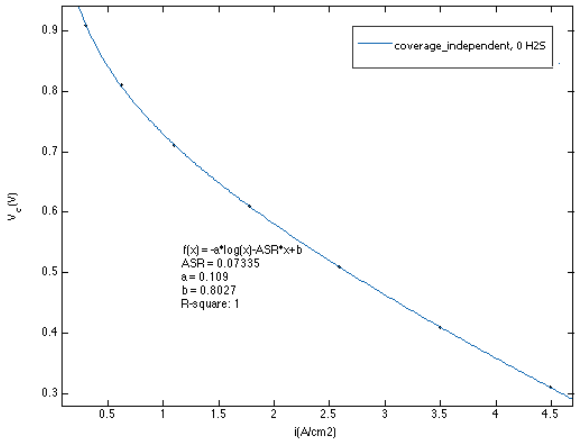

D-1: i-V curve fitting results of coverage-independent performance model for zero inlet H_2S concentration

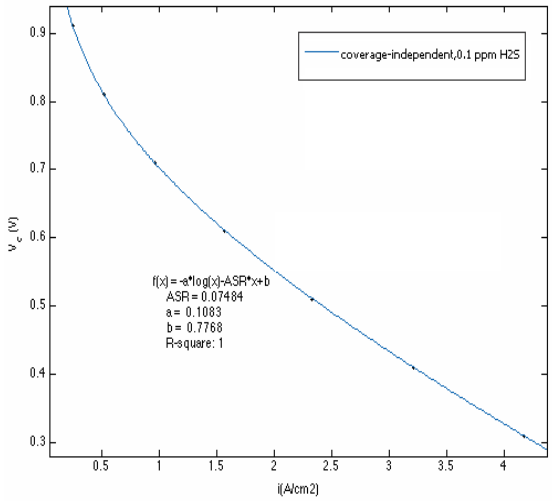

D-2: i-V curve fitting results of coverage-independent performance model for 0.1ppm inlet H_2S concentration

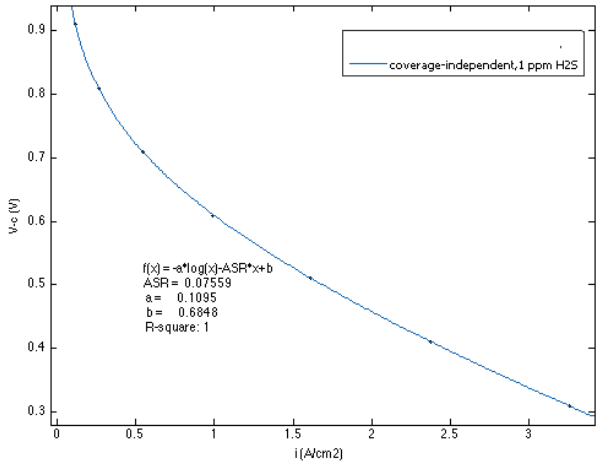

D-3: i-V curve fitting results of coverage-independent performance model for 1ppm inlet H_2S concentration

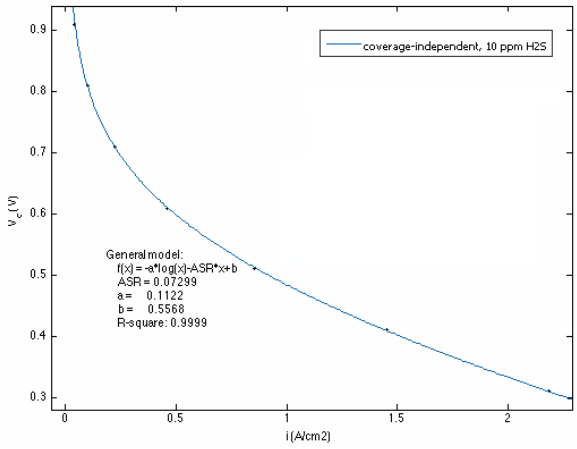

D-4: i-V curve fitting results of coverage-independent performance model for 10ppm inlet H_2S concentration

The results of fitting the i-V curves of the coverage-dependent performance model to equation (3.76) by linear least square method with their R-square values are shown in figure D-5, D-6, D-7 and D-8 for 0, 0.1,1 and 10 ppm H_2S respectively.

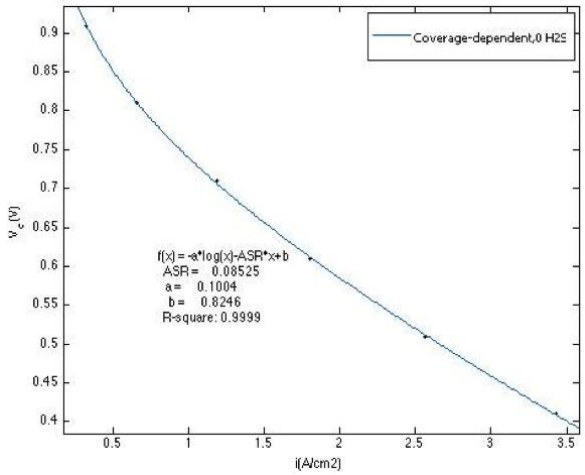

D-5: i-V curve fitting results of coverage-dependent performance model for zero inlet H_2S concentration

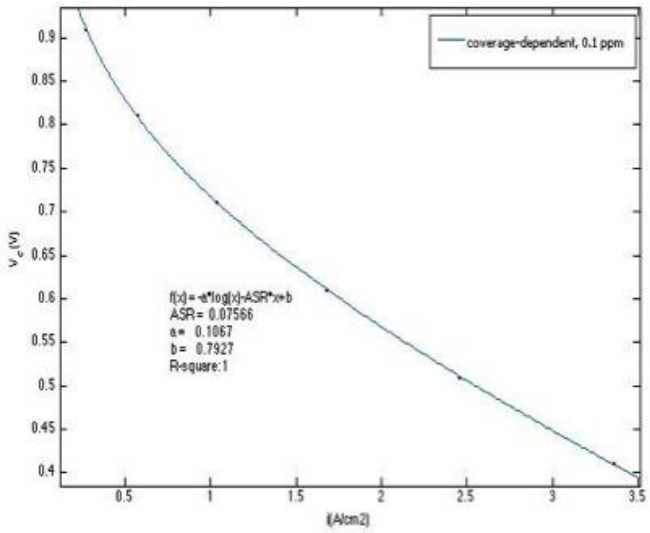

D-6: i-V curve fitting results of coverage-dependent performance model for 0.1 ppm inlet H_2S concentration

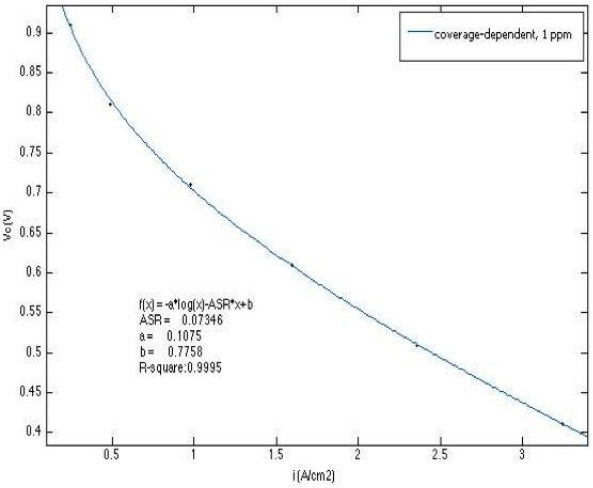

D-7: i-V curve fitting results of coverage-dependent performance model for 1 ppm inlet H_2S concentration

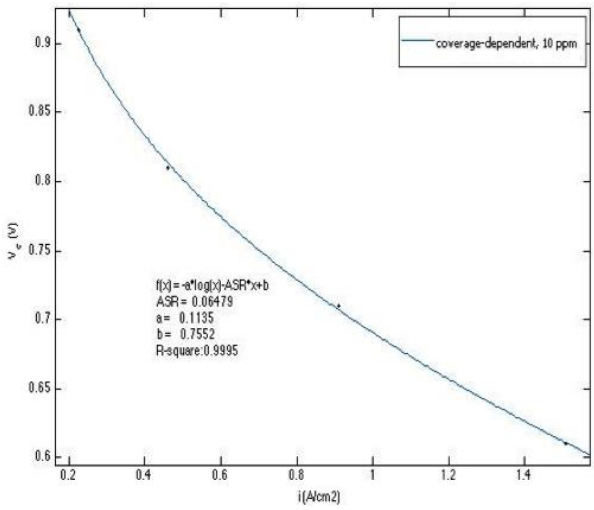

D-8: i-V curve fitting results of coverage-dependent performance model for 10 ppm inlet H_2S concentration

Appendix E

Change of anode activation overpotential as a function of current density with the effect of sulfur poisoning

In galvanostatic mode, relative loss in the cell voltage at a constant H_2S concentration increases by increase in the current density. Due to the assumptions of ideal cathode boundary, the loss in the cell voltage ($\Delta E_{cell,i_1}$) at constant current of i_1 is equal to the difference in the anode activation overpotential ($\Delta\eta_a$) due to sulfur poisoning.

$$\Delta E_{cell,i_1} = E_{cell|H2} - E_{cell|H2S} \quad \text{(E.1)}$$

$$E_{cell|H2} = E_{OCV} - i_1.ASR - \eta_{a|H2,i_1} \quad \text{(E.2)}$$

$$E_{cell|H2S} = E_{OCV} - i_1.ASR - \eta_{a|H2S,i_1} \quad \text{(E.3)}$$

$$E_{cell|H2} - E_{cell|H2S} = \eta_{a|H2S,i_1} - \eta_{a|H2,i_1} \quad \text{(E.4)}$$

$$\Delta E_{cell,i_1} = \Delta\eta_a \quad \text{(E.5)}$$

Therefore, the relative loss in cell voltage at current density i_1 is equal to the increase in the anode activation overpotential divided by the initial cell voltage (at zero H_2S concentration).

$$\Delta E_{cell,i_1,R} = \frac{\Delta E_{cell,i_1}}{E_{cell|H2}} = \frac{\eta_{a|H2S,i_1} - \eta_{a|H2,i_1}}{E_{cell,i1|H2}} \quad \text{(E.6)}$$

Similarly, the relative cell voltage drop at current density i_2 is calculated by:

$$\Delta E_{cell,i_2,R} = \frac{\Delta E_{cell,i_2}}{E_{cell|H2}} = \frac{\eta_{a|H2S,i_2} - \eta_{a|H2,i_2}}{E_{cell,i2|H2}} \quad \text{(E.7)}$$

To compare the relative loss in cell voltage at two different current densities of i_1 and i_2 exposed to the same H_2S concentration, the anode activation overpotential as a function of current density should be studied.

$$\eta_{an} = \ln(i)\frac{RT}{(\beta+1).F} - \ln(i_0)\frac{RT}{(\beta+1).F} \quad \text{(E.8)}$$

Figures E-1 and E-2 show anode activation overpotential as a function of current density at different H_2S concentrations for coverage-independent and coverage-dependent models respectively.

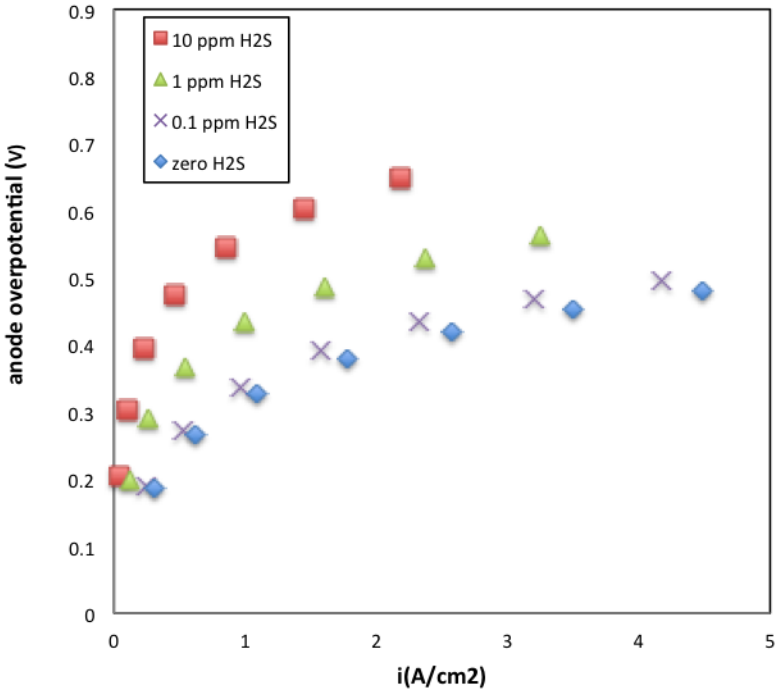

Figure E-1: Anode overpotential as a function of current density for coverage-independent performance model, T=700ºC with Base Case parameters.

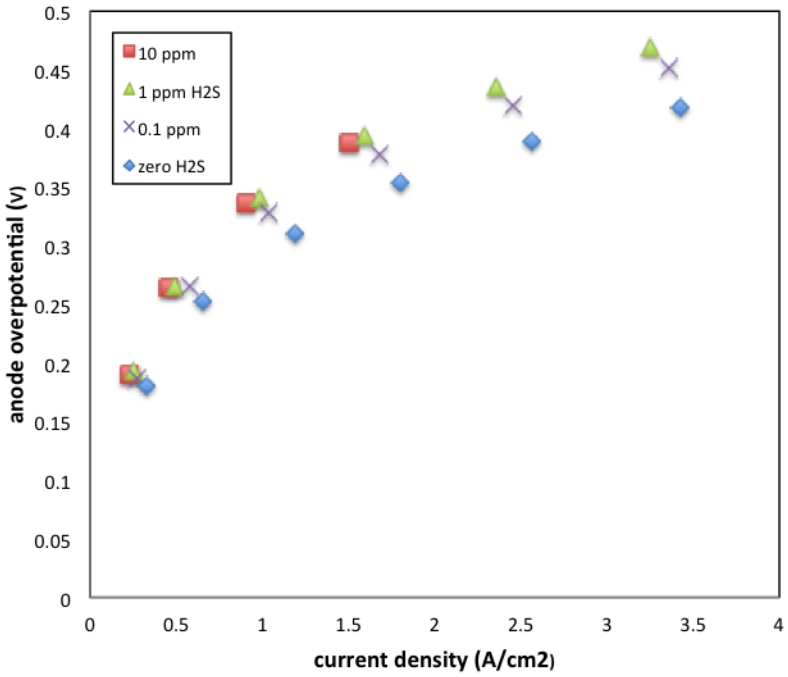

Figure E-2: Anode overpotential as a function of current density for coverage-dependent performance model, T=700ºC with Base Case parameters

As it is shown the anode overpotential increases at a constant current by increase in the H_2S concentrations. Also by the increase in the current density the overpotential curves at each H_2S concentration deviate from the curve at zero H_2S concentration. And the slope of curves increases by increase in H_2S concentration. This behavior cannot be justified from the $\eta_{an} = \ln(i)\frac{RT}{(\beta+1).F} - \ln(i_0)\frac{RT}{(\beta+1).F}$ equation. Since tis equation implies that by the increase in the H_2S concentration and decrease of i0, only the intercept of the equation $(-\ln(i_0)\frac{RT}{(\beta+1).F})$ is being

affected. Meaning that by increase in H_2S content, intercept of the new curves increase without any change in the slope of the curves. Therefore, based on the fitted expression ($\eta_{an} = \ln(i)\frac{RT}{(\beta+1).F} - \ln(i_0)\frac{RT}{(\beta+1).F}$), the difference between the anode overpotential caused upon sulfur poisoning remains constant by changing the current density. However, it should be noted that the transportation effect is not considered in this formulation. Not having considered the loss due to the transportation limitation, the slope of the anode overpotential curves is affected by the increase of the current density accounting for the concentration losses at higher current density. Therefore, diverging anode overpotential curves at higher current density are observed as in this figure, resulting in higher $\Delta\eta_a$ and ΔE_{cell} at higher current densities.

Appendix F

Loss in cell performance formulations

In this appendix the formulations of the relative increase in the anode overpotential ($\Delta\eta_R$) defined in our model and the relative increase in the cell resistance (ΔR_R) defined by Cheng et al. at galvanostatic mode are presented and compared.

Relative increase in the anode overpotential ($\Delta\eta_R$) is defined as:

$$\Delta\eta_{a,R} = \frac{\Delta\eta_a}{\eta_{a|H2}} \tag{F.1}$$

$$\Delta\eta_a = \eta_{a|H2S} - \eta_{a|H2} \tag{F.2}$$

$$\eta_{a|H2} = E_{OCV} - E_{cell|H2} - i.ASR \tag{F.3}$$

$$\eta_{a|H2S} = E_{OCV} - E_{cell|H2S} - i.ASR \tag{F.4}$$

$$\Delta\eta_a = E_{cell|H2} - E_{cell|H2S} = \Delta E_{cell} \tag{F.5}$$

$$\Delta\eta_R = \frac{\Delta E_{cell}}{\eta_{a|H2}} \tag{F.6}$$

$$\Delta\eta_R = \frac{\Delta E_{cell}}{E_{OCV} - E_{cell|H2} - i.ASR} \tag{F.7}$$

The relative increase in the cell resistance defined by Cheng et al. is defined as:

$$\Delta R_R = \frac{\Delta R|_{H2S}}{R|_{H2}} \tag{F.8}$$

$$E_{cell|H2} = E_{OCV} - i.(R|_{H2}) \tag{F.9}$$

$$E_{cell|H2S} = E_{OCV} - i.(R|_{H2} + \Delta R|_{H2S}) \tag{F.10}$$

$$\Delta R|_{H2S} = \frac{E_{cell|H2} - E_{cell|H2S}}{i} = \frac{\Delta E_{cell}}{i} \tag{F.11}$$

$$\Delta R_R = \frac{\Delta E_{cell}}{iR|_{H2}} = \frac{\Delta E_{cell}}{E_{OCV} - E_{cell|H2}} \tag{F.12}$$

By comparing the $\Delta\eta_{a,R}$ and ΔR_Rformulations, it can be inferred that both expressions measure the relative increase in the resistance. However, in the definition of the cell resistance by Cheng et al. both the ohmic and activation losses are considered, making the initial cell resistance equal to $E_{OCV} - E_{cell|H2}$ and higher than initial resistance of our model ($E_{OCV} - E_{cell|H2} - i.ASR$), in which the ohmic resistance is excluded.